Semi-analytical methods for simulating the groundwater-surface water interface

by

Ali A Ameli

A thesis

presented to the University of Waterloo

in fulfillment of the

thesis requirement for the degree of

Doctor of Philosophy

in

Civil Engineering

Waterloo, Ontario, Canada, 2014

AUTHOR'S DECLARATION

I hereby declare that I am the sole author of this thesis. This is a true copy of the thesis, including any required final revisions, as accepted by my examiners.

I understand that my thesis may be made electronically available to the public.

Abstract

Groundwater-surface water interaction is a key component of the hydrologic cycle. This interaction plays a key role in many environmental issues such as the impacts of land use and climate change on water availability and water quality. Modeling of local and regional groundwater-surface water interactions improves understanding of these environmental issues and assists in addressing them. Because of the physical and mathematical complexities of this interaction, numerical approaches are generally used to model water exchange between subsurface and surface domains. The efficiency, accuracy, and stability of mesh-based numerical models, however, depend upon the resolution of the underlying grid or mesh.

Grid-free analytical methods can provide fast, accurate, continuous and differentiable solutions to groundwater-surface water interaction problems. These solutions exactly satisfy mass balance in the entire internal domain and may improve our understanding of groundwater-surface water interaction principles. However, to model this interaction, analytical approaches typically required simplifying, sometimes unrealistic, assumptions. They are typically used to implement linearized mathematical models in homogenous confined or semi-confined aquifers with geometrically regular domains.

By benefiting from the strengths of both analytical and numerical approaches, grid-free semi-analytical methods may be able to address more challenging groundwater problems which have been out of reach of traditional analytical approaches, and/or are poorly simulated using mesh-based numerical methods. Here, novel 2-D and 3-D semi-analytical solutions for the simulation of mathematically and physically complex groundwater-surface water interaction problems are developed, assessed and applied. Those models are based upon the series solution method and analytic element method (AEM) and are intended to address groundwater-surface water interactions induced by pumping wells and/or the presence of surface water bodies in naturally complex stratified unconfined aquifers. Semi-analytical solutions are obtained using the least squares method, which is used to determine the unknown coefficients in the series expansion and the unknown strengths of analytic elements. The series and AEM solutions automatically satisfy the groundwater governing equation. Hence, the resulting solutions are exact over the entire domain except along boundaries and layer interfaces where boundary and continuity conditions are met with high precision. A robust iterative algorithm is used to implement a free boundary condition along the phreatic surface with a priori unknown location.

This thesis addresses three general problem types never addressed within a semi-analytic framework. First, a steady-state free boundary semi-analytical series solutions model is developed to simulate 2-D saturated-unsaturated flow in geometrically complex stratified unconfined aquifers. The saturated-unsaturated flow is controlled by water exchange along the land surface (e.g., evapotranspiration and infiltration) and the presence of surface water bodies. The water table and capillary fringe are allowed to intersect stratigraphic interfaces. The capillary fringe zone, unsaturated zone, groundwater zone and their interactions are incorporated with a high degree of accuracy. This model is used to assess the influences of important factors on unsaturated flow behavior and the water table elevation. Second, a 3-D free boundary semi-analytical series solution model is developed to simulate groundwater-surface water interaction controlled by infiltration, seepage faces and surface water bodies along the land surface. This model can simulate the water exchange between groundwater and surface water in geometrically complex stratified phreatic (unconfined) aquifers. The a priori unknown phreatic surface will be obtained iteratively while the locations of seepage faces don't have to be known a priori (i.e., this is a constrained free boundary problem). This accurate grid-free multi-layer model is here used to investigate the impact of the sediment layer geometry and properties on lake-aquifer interaction. Using this method, the efficiency of widely-used Dupuit-Forchheimer approximation used in regional groundwater-surface water interaction models is also assessed. Lastly, this 3-D groundwater-surface water interaction model is augmented with AEM solutions to simulate horizontal pumping wells (radial collector well) for assessing surface water impacted by pumping and determining the source of extracted well water. The resulting model will be used to assess controlling parameters on the design of a radial collector well in a river bank filtration system. This 3-D Series-AEM model, in addition, mitigates the limitations of AEM in modeling of general 3-D groundwater-surface water interaction problems.

Acknowledgements

I would like to thank Dr. James Craig, my PhD advisor, for his scientific support and motivations throughout my PhD studies. Also, I have always been thankful to James for his care and advice on things other than research, specially for helping me to be a socially professional person.

It is my pleasure to thank my PhD committee members Dr. Jon Sykes and Dr. Leo Rothenburg from the Department of Civil and Environmental Engineering and Dr. Walter Illman from the Department of Earth Science of University of Waterloo. I would also like to thank the comments of Dr. Jeffrey McDonnell on my research during my visit of the Global Institute of Water Security (GIWS) at the University of Saskatchewan as a guest researcher.

The majority of the thesis contents were peer-reviewed in the form of technical journal papers before thesis submission. I would like to thank the anonymous reviewers for the journals Advances in Water Resources and Water Resources Research who reviewed the papers associated with Chapter 4 and Chapter 5. Their constructive comments significantly improved the contents of my thesis.

Table of Contents

List of Figures

List of symbols

A_{jn}^m, B_{jn}^m , A_j^m, B_j^m, C_j^m, D_j^m	Unknown coefficient of series solution of the m^{th} layer (3-D and 2-D solutions)
$d_{sw}(x,y)$ [L]	The surface water body depth
F_i [L^2T^{-1}]	The influence function of each analytic element
$F(x,y)$ [LT^{-1}]	3-D infiltration-evapotranspiration function obtained using Equation (5-5)
$f(x)$ [LT^{-1}]	2-D infiltration-evapotranspiration function
H_r [L]	Water level stage of the river or lake
H_w [L]	Head in the radial collector well
$h\,(x,y,z)$ [L]	Total hydraulic head
K^s [LT^{-1}]	Saturated hydraulic conductivity
K^u [LT^{-1}]	Unsaturated conductivity
K_m^s [LT^{-1}] *	Saturated hydraulic conductivity of the m^{th} layer
L [L]	Domain length
L_x, L_y [L]	Domain length in *x* and *y* directions
l^i [L]	Half of the length of each segment of a line element used in AEM
l_{wl} [L]	Length of radial collector arm
M_u	Number of unsaturated layers
M_s	Number of saturated layers
M	Total number of layers
N , J	Number of series terms in each direction
NC	Total number of control points along each interface used for least squares
NC_x, NC_y	Number of control points along each interface in *x* and *y* directions used for

	least squares
N_s	The number of segments along a line element used in AEM to represent a pumping well
N_I	Number of image wells
NC_w	Number of control points along the well screens surface
P	The ratio of aquifer to sediment hydraulic conductivity
Q [L^3T^{-1}]	Radial collector well pumping rate
q_x, q_y, q_z [LT^{-1}]	Specific discharges in *x*, *y* and *z* directions
R [LT^{-1}]	Infiltration rate
RE [LT^{-1}]	recharge rate
r	Iteration number
S_y	Specific yield
$U(x), V(y), W(z)$	Eigenfunctions of the Laplace equation used in series solutions method
x_0^i, y_0^i, z_0^i	The center of each segment of a line sink in the global coordinate system
z_{wt} [L]	Water table elevation
z_1 [L]	Land surface elevation
z_t [L]	Top of the modeled domain elevation
z_m [L]	Elevation of the interfaces between different soil layers
z_{M+1} [L]	Bottom bedrock elevation
z_{cf} [L]	Top of capillary fringe elevation
z_{wl} [L]	Elevation of radial collector well
α [L^{-1}]	The exponential function parameter, Equation (5-5)
α_m [L^{-1}]	Sorptive number of the m^{th} layer

δ [L]	Transition zone depth, Equation (5-5)
$\omega_j, \omega_n, \gamma_{jn}$	Eigenvalues of the Laplace equation used in series solutions method
ϕ_w^i [L^2T^{-1}]	The discharge potential correspond to i^{th} segment of a line element (AEM)
$\phi^s\ (x, y, z)$ [L^2T^{-1}]	Saturated discharge potential
ϕ^u [L^2T^{-1}]	Unsaturated Kirchhoff potential
ψ_m^u[L^2T^{-1}]	Unsaturated stream function of the m^{th} layer
ψ_m^s [L^2T^{-1}]	Saturated stream function of the m^{th} layer
ϕ_m^u[L^2T^{-1}]	Unsaturated Kirchhoff potential of the m^{th} layer
ϕ_m^s [L^2T^{-1}] *	Saturated discharge potential of the m^{th} layer
φ_m^e [L]	Air entry pressure of the m^{th} layer
φ [L]	Pressure head
${\sigma_0}^i$	Constant strength of each segment of a line element used in AEM
τ	The relaxation factor of the iterative scheme
Θ	volumetric water content

* Superscript or subscript (s) and (u) are only mentioned for coupled saturated-unsaturated simulation to make a distinction between saturated and unsaturated variables/parameters. If noting mentioned variables/parameter is for pure saturated simulation.

Chapter 1
Introduction

1.1 Subsurface-surface interaction

Groundwater and surface water are not typically isolated from one another. Continual water, nutrient and contaminant exchange involving a wide range of physical, biological, chemical and biogeochemical processes have been fundamental concerns in water supply, water quality and ecosystem management. Lake and stream acidification, lake eutrophication, human activities (e.g., agricultural development, loss of wetlands and flood plains due to urban development, excessive pumping, etc.) and natural hazards such as landslide and flooding have been issues which have encouraged hydrologists, geologists and ecologists to consider the interaction between subsurface and surface water. Pumping, for example, may cause decline in groundwater levels in the vicinity of surface water bodies and capture groundwater which would have potentially discharged into surface water bodies as base flow. Excessive pumping may similarly induce flow out of surface water bodies into the aquifer. Both phenomena lead to the depletion of stream flow. Lowering of the water table level may likewise disconnect ground water and surface water, and alter riparian vegetation. Efficient land use and water management in different physiographic settings requires a comprehensive understanding of the interaction between pumping wells, groundwater and surface water bodies. This understanding can also be helpful to assess the reliability of wells water quality through determining the pumping wells sources.

Groundwater-surface water interactions have been assessed experimentally in different physiographic settings. Using field methods, there has been a significant body of field work done to assess stream-aquifer interaction [e.g., *Dunne and Black*, 1970; *Harvey et al.*, 1997; *Hunt et al.*, 2001; *Sophocleous et al.*, 1988] and Lake-aquifer interaction [e.g., *Harvey et al.*, 1997; *Smerdon et al.*, 2005]. Due to the practical complexities, the utility of experimental analysis alone might be limited [e.g., *Halford and Mayer*, 2000; *Rushton*, 2007], and mathematical models are needed.

1.1.1. Modeling of Subsurface-surface interaction

Modeling of local and regional subsurface-surface water interaction assists in the conceptual understanding of this interaction and its controlling parameters. In addition, efficient design of processes and technologies used for groundwater and surface water withdrawal and treatment often requires a robust subsurface-surface water interaction model. Examples include the design of (1)

radial collector (RC) wells which provide a large pumping well yield under low drawdown, (2) bank filtration process where surface water contaminants are purified (for use as drinking water) by passing through the banks of rivers or lakes or (3) pump and treat remediation near streams where groundwater contaminants are captured by vertically or non-vertically oriented pumping wells. All of these systems may require detailed analysis of the 3-D interaction between surface water bodies, pumping wells and groundwater.

Accurate simulation of 3-D groundwater-surface water interaction can be cumbersome due to mathematical complexities including a non-linear governing equation, a constrained non-linear free boundary along the water table, and/or the presence of heterogeneity, anisotropy and naturally complex geometry. If unsaturated conditions are explicitly modeled in the vadose zone, material properties (and therefore the governing equation) may likewise become non-linear. In most cases, 3-D numerical (rather than analytical) models are generally used to simulate the complex interaction between the subsurface and surface [e.g., *Cardenas and Jiang*, 2010; *Larabi and De Smedt*, 1997; *Oz et al.*, 2011; *Smerdon et al.*, 2007; *Therrien et al.*, 2008; *Werner et al.*, 2006]. Mesh-based numerical models, however, are prone to numerical artifacts; the resolution of the underlying grid or mesh significantly impact the efficiency and accuracy of numerical approaches. The discretization requirements in numerical models typically increases computational expense, particularly for free boundary problems [*An et al.*, 2010; *Knupp*, 1996]. Discretization constraints may also lead to poor representation of the geometry and properties of surface water bodies at a different scale than the regional aquifer it is part of [*Mehl and Hill*, 2010; *Rushton*, 2007; *Sophocleous*, 2002; *Townley and Trefry*, 2000], or the details of pumping impacts on streams [*Moore et al.*, 2012; *Patel et al.*, 2010]. Along a well screen, for example, a high resolution 3-D discretization is required while the treatment of the unique boundary condition at the well (using a head dependent boundary cell as is done in MODFLOW) might be cumbersome for mesh-based approaches [*Patel et al.*, 1998]. Misalignment of arbitrary-directed wells with respect to the mesh discretization may also compromise the efficiency of the discrete models [*Moore et al.*, 2012].

Accurate grid-free (mesh-less) analytical approaches have occasionally been employed to address mathematically and geometrically simplified 1-D [e.g., *Boano et al.*, 2010; *Hantush*, 2005; *McCallum et al.*, 2012; *Serrano and Workman*, 1998; *Teloglou and Bansal*, 2012; *Workman et al.*, 1997] and 2-D [e.g., *Anderson*, 2003; *Haitjema and Mitchell-Bruker*, 2005] groundwater systems to provide a better understanding of the basic principles of the interaction between groundwater and surface water,

and at the same time serve as a benchmark for numerical model validation. However, in applying simplifying assumptions regarding problem geometry or physics, analytical approaches cannot typically provide a realistic representation of the complexity of groundwater-surface water exchange flows in heterogeneous unconfined aquifers.

Benefiting from the strengths of both analytical and numerical schemes, grid-free semi-analytical approaches have the potential to address more complex problems at lesser computational cost than discrete equivalents. The basic idea behind semi-analytical approaches is the augmentation of standard analytical techniques (e.g., series solutions, analytic element method, separation of variables, Laplace and Hankel transforms, etc.) with a simple numerical technique such as least squares minimization or numerical inversion/integration [*Craig and Read*, 2010]. Semi-analytical methods such as series solutions and analytic element method (AEM) have been augmented with a least squares minimization algorithm to successfully address geometrically complex problems [*Luther and Haitjema*, 1999; *Luther and Haitjema*, 2000; *Read and Volker*, 1993; *Wong and Craig*, 2010].

Semi-analytical series solution methods have been developed to simulate homogenous [*Read and Volker*, 1993] and multi-layer [*Craig*, 2008; *Wong and Craig*, 2010] topography-driven flow in naturally complex two dimensional aquifers with finite domains. *Marklund and Wörman* [2011]were able to use such methods to demonstrate that the topography driven flow hypothesis induces a systematic error and, according to the criterion developed by *Haitjema and Mitchell-Bruker* [2005], it is not valid for most groundwater systems. Treatment of the phreatic surface as a free boundary remains the preferred course of action. This is particularly true when simulating groundwater-surface water exchanges fluxes, where the water table location can not be prescribed, as done with the topography driven approach.

Semi-analytical AEM has been also used as a robust alternative to mesh-based numerical models for (1) the simulation of large-scale regional groundwater-surface water interaction [*Haitjema et al.*, 2010; *Hunt*, 2006; *Moore et al.*, 2012; *Simpkins*, 2006], (2) screening or quick hydrologic analysis and stepwise modeling [*Dripps et al.*, 2006; *Hunt*, 2006; *Strack*, 1989], (3) assessment of the theories behind the estimation of effective conductivity and dispersion coefficients in highly heterogeneous formations [*Barnes and Janković*, 1999; *Janković et al.*, 2003], and (4) 3-D flow toward partially penetrating vertical, horizontal and slanted pumping well(s) in homogenous unconfined aquifers and multi layer confined aquifers [*Bakker et al.*, 2005; *Luther and Haitjema*, 1999; *Steward*, 1999;

Steward and Jin, 2001; 2003]. However, the representation of the phreatic surface, naturally complex layer stratification and surface water bodies geometry is still challenging using analytic elements [*Hunt*, 2006], especially in 3-D.

1.2 Research objectives and Thesis Structure

The objective of this thesis is to extend available semi-analytical series solution methods and the analytic element method (AEM) for simulation of 2-D and 3-D steady-state groundwater-surface water interaction in a geometrically complex stratified domain. The interaction can be controlled by arbitrary-oriented pumping wells, precipitation, evapotranspiration, seepage faces and surface water bodies. The phreatic surface will be treated as a constrained non-linear free boundary condition. Note that the developed solutions in this thesis are not integrated groundwater-surface water models, but are subsurface models aimed at resolving exchange fluxes under a predefined infiltration rate. Direct exchanges with surface water bodies are also considered. The contributions developed in this thesis collectively have pushed the series solution and AEM methods from a specialized tool useful for some constrained problems to a quite general modeling method capable of simulating complex flow under quite general conditions. Some of these conditions may be challenging to properly address using mesh-based numerical methods.

This thesis is structured around published and submitted articles. A brief background of field and modeling studies of groundwater-surface water interaction, and the mathematical formulation for the governing laws of subsurface flow is presented in chapter 2. Chapter 3 explains the theoretical basics behind semi-analytical series solutions and AEM. Chapters 4 and 5 correspond to two published articles [*Ameli and Craig*, 2014; *Ameli et al.*, 2013] about the extension of series solutions to simulate 2-D and 3-D groundwater-surface water interaction with and without the vadose zone and capillary fringe. In chapter 4, the series solution approach is extended to address 2-D saturated-unsaturated flow in naturally complex stratified unconfined aquifers where the free boundary water table interface can intersect the layer interfaces. This model is extended to simulate 3-D groundwater-surface water interaction in a geometrically complex stratified unconfined aquifer (chapter 5), where flow is controlled by water exchange across the land surface including infiltration, seepage faces and exchange with surface water bodies. The 3-D series solution model is augmented with 3-D AEM techniques in chapter 6 to assess groundwater-surface water interaction between a group of horizontal

wells (radial collector wells) and surface water features in geometrically complex stratified unconfined aquifers. Wells are allowed to intersect stratigraphic interfaces in this model.

The developed models have the potential to assess factors controlling groundwater-surface water interaction. Fast, continuous, accurate and grid-free semi-analytical models developed here support the conceptual understanding of basic principles of groundwater-surface water interaction. Application examined here include an examination of the important controls on the behavior of unsaturated and capillary fringe flow (chapter 4), assessment of the validity of Dupuit-Forchheimer approximation used in regional 2-D models and investigation into lakebed geometry controls on groundwater-surface water exchange (chapter 5) and design of a radial collector well in a RBF system (chapter 6).

Chapter 2
Background

2.1 Groundwater-surface water interaction

The interaction between groundwater and surface water occurs in different physiographic and climatic settings around the world. This interaction may take three forms; a surface water feature loses water and solutes into groundwater, groundwater discharges water and solutes into a surface water body or a surface water body loses and gains water and solutes along different reaches. Water is also exchanged across the ground surface via the mechanisms of transpiration, evaporation and infiltration through the vadose zone.

Groundwater-surface water interactions have been assessed experimentally in different physiographic settings such as mountain, riverine, coastal, and karst terrains [*Carter*, 1990; *Correll et al.*, 1992; *Harte and Winter*, 1993; *Smerdon et al.*, 2005; *Stark et al.*, 1994; *Winter and Rosenberry*, 1995], leading to a well-established conceptual model for groundwater-surface water exchange. Figure 2-1 depicts this conceptual model for groundwater-surface water interaction including various surface and subsurface flow exchange mechanism in an unconfined aquifer. The portion of stream or lake flow that comes from deeper subsurface flow is called baseflow (groundwater). Interflow is the lateral movement of shallow subsurface water in unsaturated zone that may return to the ground surface through seepage faces (return flow or throughflow) or enters a stream or lake prior to infiltrating into deep groundwater and becoming baseflow; the portion which is infiltrated into groundwater zone is termed groundwater recharge, usually expressed as a flux across the water table surface. The groundwater zone is bounded above by the water table surface, which is also called the phreatic surface. Along the phreatic surface, the water in the soil pores is at atmospheric pressure (zero pressure head) while in the saturated zone there is positive pore water pressure. The unsaturated zone, also termed the vadose zone, is the part of an unconfined aquifer between the ground surface and water table. Water in the vadose zone has a pore pressure head less than atmospheric pressure, and is retained in the soil matrix by a combination of adhesion and capillary forces. At the ground surface, water can be exchanged with the atmosphere and ponded at the surface by infiltration, evaporation and transpiration processes. Infiltration is the process by which water (rain fall or snowmelt) on the ground surface enters the soil. The infiltration rate is the rate at which soil is able to absorb surface water, which decreases as the soil becomes more saturated. If the precipitation rate exceeds the

infiltration rate, overland flow along the ground surface occurs. Evaporation and transpiration (collectively termed evapotranspiration) are processes involving withdrawal of water from the shallow subsurface. Factors that impact evapotranspiration include types of vegetation and land use, the plant's growth stage or level of maturity, percentage of soil cover, solar radiation, humidity, temperature, and wind speed.

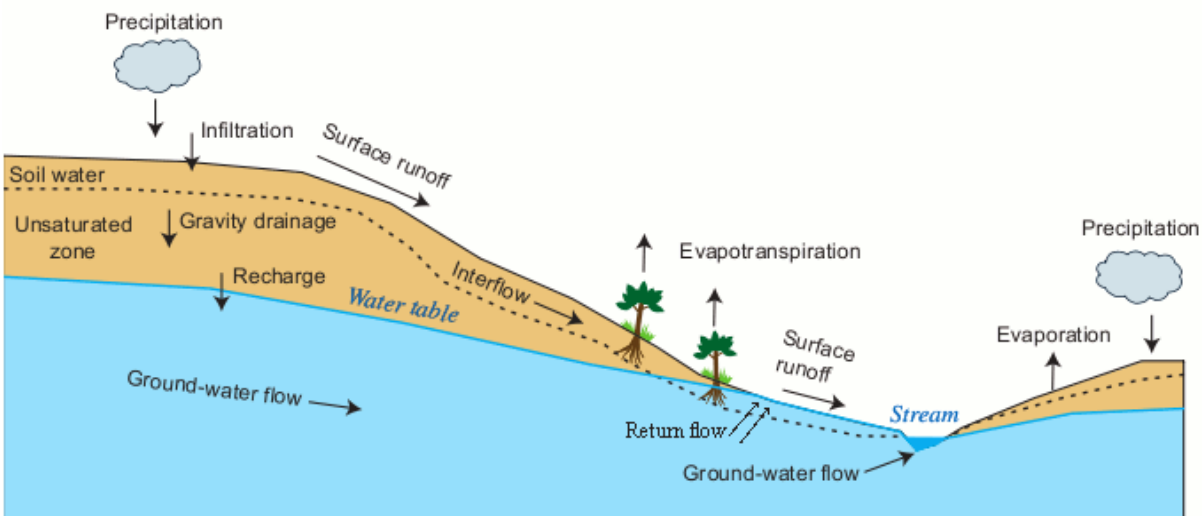

Figure 2-1. Layout of the general groundwater-surface water interaction problem. Image was modified from http://people.ucsc.edu/~bkdaniel/

2.2 Groundwater-surface water interaction induced by pumping wells

Large quantities of groundwater and (indirectly) surface water may be withdrawn by a single well or a group of pumping wells. Pumping wells can be placed vertically, horizontally or slanted depending upon the chosen design. The withdrawal water can be used for municipal consumption, agriculture or industrial purposes. In the following, some of the applications of pumping wells installation are briefly described, with a focus on systems with non-vertical wells. Note that, traditionally vertical wells have been used for irrigation and municipal or rural water supplies.

River Bank Filtration (RBF)

Withdrawal of water from pumping wells close to surface water bodies (e.g., rivers) essentially is a means of using surface water while providing a natural filtering process referred to the river bank filtration (RBF). In a manner similar to slow sand filtration, river water contaminants, including

pathogens (e.g., Cryptosporidium and Giardia), organic compounds and turbidity are attenuated through a combination of processes such as filtration, microbial degradation, sorption to sediments and dilution with background groundwater [*Hiscock and Grischek*, 2002; *Moore et al.*, 2012; *Ray et al.*, 2002]. RBF systems are typically used in alluvial aquifers which may consist of a variety of deposits ranging from fine sand to pebbles and cobbles. Coarse-grained and permeable deposits are ideal formations for RBF. Proper design of RBF systems requires the ability to accurately estimate drawdown and withdrawal rate across the groundwater-surface water interface.

Pump and treat remediation

Pump and treat is one the most common groundwater remediation technologies which involves pumping of contaminated groundwater to surface for treatment. A group of pumping wells is designed to capture the plume contaminant followed by a couple of biological and chemical processes to treat extracted groundwater [*Matott et al.*, 2006]. The efficiency of the technology depends upon the configuration and number of pumping wells. Pumping near surface resources may lead to excessive withdrawal of surface water or inefficient, deleterious and inadvertent withdrawal of surface contamination.

Aquifer tests

Pumping wells are also used to determine the local and regional material properties of the aquifers through aquifer tests including constant head test, constant rate test, slug test and recovery test [*Butler Jr*, 1997; *Charbeneau*, 2006]. Aquifer tests near surface features must address their presence appropriately to properly be used to estimate aquifer properties.

2.2.1 Pumping Well orientation

Vertical wells have been traditionally used for most applications, as it is much more challenging and/or expensive to do otherwise. However, the construction of non-vertical, particularly horizontal, wells has become more common place after significant advances in drilling technologies [*Joshi*, 2003]. The benefits of horizontal wells over vertical ones have been reported by many researchers [*Bakker et al.*, 2005; *Joshi*, 2003; *Moore et al.*, 2012; *Patel et al.*, 2010; *Yeh and Chang*, 2013] as follows:

- Horizontal wells can be installed in urban areas with obstructions such as buildings and roads along the land surface

- Horizontal wells yield a smaller drawdown near the well to withdraw the desired water demand
- In shallow aquifers, horizontal wells can generally extract more water since useful screen length does not vary with the changes in the saturated thickness.
- The entering groundwater velocity to a horizontal well screen is lower due to a larger available screen length. This decreases the rate of clogging and minimizes the head loss between the aquifer and the well.
- The operating cost of horizontal wells is lower since fewer wells are required to fulfill the desired yield.

It seems that horizontal wells can be an appropriate alternative to vertical ones. A group of horizontal wells may be designed to increase the efficiency of the pumping. As an example, radial collector (RC) well systems, initially developed by Ranney in 1930, consists of a number of horizontal wells (lateral arms) screened to the aquifer, and connected to a vertical cylindrical caisson [*Moore et al.*, 2012]. Traditionally collector wells were made from steel pipes with slots punched or cut into them, and were installed using a hydraulic jack by driving them into the aquifer through ports in the caisson. More recently, they are composed of wound stainless steel screens [*Bakker et al.*, 2005]. A radial collector well system is able to withdraw a large quantity of surface water through alluvial riverbed in regions where rivers are not perennial. Recently RC wells have been widely applied in river bank filtration (RBF) and pump and treat processes [*Bakker et al.*, 2005; *Hoffman*, 1998; *Moore et al.*, 2012; *Patel et al.*, 2010]. It should be noted that arbitrarily oriented well sections are notably difficult to simulate using numerical methods.

2.3 Subsurface flow mathematical formulation

In this section, the governing equations for subsurface water flow are presented. First, governing equations for 3-D transient and steady-state saturated flow in porous media are derived. The 3-D steady-state governing equation for saturated flow is used in chapters 5 and 6. The 2-D steady-state governing equation for saturated flow is also used in chapter 4. Second, the governing equations for 3-D transient and steady-state unsaturated flow are described. The 2-D steady-state linearized form of this equation is used in chapter 4. Note that hereafter (s) and (u) describe saturated and unsaturated properties/variables.

2.3.1 Saturated Flow

The saturated zone includes groundwater and capillary fringe zones where the moisture content is equal to the porosity. Applying continuity of mass with a water incompressibility assumption for a representative elementary volume leads to

$$-\left(\frac{\partial q_x}{\partial x}+\frac{\partial q_y}{\partial y}+\frac{\partial q_z}{\partial z}\right)=\frac{\partial \Theta}{\partial t} \tag{2-1}$$

$$\text{where } q_x=-K_x^s\frac{\partial h}{\partial x},\quad q_y=-K_y^s\frac{\partial h}{\partial y},\quad q_z=-K_z^s\frac{\partial h}{\partial z}$$

q_x, q_y and q_z [LT^{-1}] and K_x^s, K_y^s and K_z^s [LT^{-1}] are specific discharges and saturated hydraulic conductivities in *x*, *y* and *z* directions, respectively and $h\,(x,y,z)$ [L] is the total hydraulic head. Θ is the volumetric water content which can vary due to the compressibility of the fluid or media. As is common in analytical and semi-analytical methods literature, here, the Darcy law for isotropic and homogenous porous media may be posed in terms of a discharge potential, $\phi^s(x,y,z)=K^s\,h\,(x,y,z)$ [L^2T^{-1}], defined as

$$q_x=-\frac{\partial \phi^s}{\partial x}\;\&\;q_y=-\frac{\partial \phi^s}{\partial y}\;\&\;q_z=-\frac{\partial \phi^s}{\partial z} \tag{2-2}$$

By combining the Darcy law (Equation (2-2)) and continuity of mass (Equation (2-1)), governing equation for 3-D transient, saturated flow in terms of discharge potential is derived as

$$\frac{\partial^2 \phi^s}{\partial x^2}+\frac{\partial^2 \phi^s}{\partial y^2}+\frac{\partial^2 \phi^s}{\partial z^2}=\frac{\partial \Theta}{\partial t} \tag{2-3}$$

which is valid in any domain with piecewise constant hydraulic conductivity, though the definition of the discharge potential changes at interfaces between different media. For the steady-state case, the Laplace equation governs 3-D saturated flow in terms of discharge potential as

$$\frac{\partial^2 \phi^s}{\partial x^2}+\frac{\partial^2 \phi^s}{\partial y^2}+\frac{\partial^2 \phi^s}{\partial z^2}=0 \tag{2-4}$$

2.3.2 Unsaturated Flow

Buckingham [1907] using the fact that the unsaturated conductivity, K^u, is a function of pressure head φ [L], has extended the applicability of Darcy law to unsaturated flow as

$$q_x = -K^u(\varphi)\frac{\partial\varphi}{\partial x}, \quad q_y = -K^u(\varphi)\frac{\partial\varphi}{\partial y}, \quad q_z = -K^u(\varphi)\frac{\partial\varphi}{\partial z} - K^u(\varphi) \tag{2-5}$$

Richards [1931] coupled continuity of mass (equation (2-1)) and Darcy- Buckingham constitutive equations (Equation (2-5)) to obtain the 3-D governing equation for transient unsaturated flow in terms of pressure head as:

$$\frac{\partial}{\partial x}\left(K^u(\varphi)\frac{\partial\varphi}{\partial x}\right) + \frac{\partial}{\partial y}\left(K^u(\varphi)\frac{\partial\varphi}{\partial y}\right) + \frac{\partial}{\partial z}\left(K^u(\varphi)\frac{\partial\varphi}{\partial z}\right) + \frac{\partial}{\partial z}K^u(\varphi) = \frac{\partial\theta(\varphi)}{\partial t} \tag{2-6}$$

The solution of this equation is typically complicated by the non-linear relationships, $K^u(\varphi)$ and $\theta(\varphi)$. For the vadose zone, in this thesis, the problem is expressed in terms of a Kirchhoff potential $\phi^u[\mathrm{L}^2\mathrm{T}^{-1}]$ in a manner similar to *Philip* [1998] or *Bakker and Nieber* [2004]. This facilitates the linearization of non-linear governing equation of the vadose zone. The Kirchhoff potential is a function of pressure head φ[L] as

$$\phi^u(\varphi) = \int_{-\infty}^{\varphi} K^u(\eta)d\eta \tag{2-7}$$

and the negative of the gradient of this potential corresponds to the unsaturated flow rate. Note that various non-linear forms of $K^u(\varphi)$ are available. The conductivity-pressure head function proposed by *Gardner* [1958] is analytically tractable, and will be used in this thesis. Using the exponential Gardner model with air entry pressure, φ^e.

$$K^u(\varphi) = K^s \exp\left(\alpha(\varphi - \varphi^e)\right) \tag{2-8}$$

the Kirchhoff potential becomes:

$$\phi^u(\varphi) = \frac{K^e}{\alpha}\exp(\alpha\varphi) \tag{2-9}$$

where α [L^{-1}] is sorptive number and φ^e [L] is the air entry pressure, and $K^e = K^s \exp(-\alpha \varphi^e)$ [LT^{-1}]. Note that sorptive number depicts the gravity to capillary potential of an unsaturated soil. Using the Kirchhoff potential (equation (2-9)) and Gardner soil characteristic model (equation (2-8)), the 2-D steady-state form of non-linear Richards' equation is simplified to an equivalent linear 2-D governing equation for unsaturated flow in the vadose zone [*Bakker and Nieber*, 2004; *Basha*, 1999; 2000]:

$$\frac{\partial^2 \phi^u}{\partial x^2} + \frac{\partial^2 \phi^u}{\partial z^2} + \alpha \frac{\partial \phi^u}{\partial z} = 0 \qquad (2\text{-}10)$$

Equation (2-10) is linear and separable which can be separated into two ordinary differential equations using the method of separation of variables.

2.4 Modeling of Groundwater-surface water interaction

Modeling groundwater-surface water interaction can support the conceptual understanding of factors controlling the interaction and, when supported by field data, provides a valuable tool for site-specific analysis and design. In most cases, numerical (rather than analytical) models are generally used due to the complexity of such interaction. In the following, the major mathematical and geometrical complexities which modelers typically must attend to simulate this interaction are outlined.

Non-Linearity

Material and governing equation non-linearity may complicate the simulation of ground water-surface water interaction. Material non-linearity such as exhibited in the soil characteristic models (e.g., equation (2-8)) used for describing unsaturated material properties may significantly increase the computational cost particularly in transient groundwater-surface water interaction problems which include the vadose zone. Non-linear material properties may lead to non-linearity in the governing equation such as the Richards' equation (equation (2-6)). This equation has been widely used for the simulation of local and regional ground water-surface water interaction.

Free boundary problem

The phreatic or water table as shown in Figure 2-1, is a boundary interface between groundwater zone and unsaturated zone (capillary fringe) where water in the soil pores is at atmospheric pressure (zero pressure head). In some models, the phreatic surface has been treated as a replica of topography or

land surface after *Toth* [1963]. However, *Haitjema and Mitchell-Bruker* [2005] have presented a simple dimensionless decision criterion to assess the likelihood for whether topography-driven flow analysis is able to emulate the location of phreatic surface on the basis of aquifer size and material properties, and recharge rate. According to their criterion, the phreatic surface is generally a subdued replica of land surface in flat aquifers with a high recharge to aquifer conductivity ratio. *Marklund and Wörman* [2011] have indicated that the topography-driven flow hypothesis induces a systematic error and it is not valid for most groundwater systems. Treatment of the phreatic surface as a priori unknown free boundary is desirable. However this treatment leads to a non-linear boundary condition along the water table (e.g., a kinematic boundary condition) or when cast using the Dupuit-Forchheimer, a non-linear governing equation (e.g., the *Boussinesq* [1872] equation). Two boundary conditions have been proposed along the water table surface for the simulation of 3-D transient free boundary saturated flow in an unconfined aquifer [*Knupp*, 1996]. First, the zero pressure head condition given as

$$\varphi(x, y, z_{wt}, t) = 0 \tag{2-11}$$

and secondly, the non-linear kinematic boundary condition in terms of total hydraulic head, h, given as follows [*Wang et al.*, 2011]:

$$k_x(\frac{\partial h}{\partial x})^2 + k_y(\frac{\partial h}{\partial y})^2 + k_z(\frac{\partial h}{\partial z})^2 = S_y(\frac{\partial h}{\partial t}) + (k_z + RE)(\frac{\partial h}{\partial z}) - RE \tag{2-12}$$

where S_y and RE [LT^{-1}] are specific yield and recharge rate, respectively and z_{wt} is a priori unknown water table location. Across seepage faces and at surface water bodies, in addition, Dirichlet condition may be implemented as:

$$h(x, y, z_t, t) = z_1(x, y) + d_{sw}(x, y) \tag{2-13}$$

where z_1 is the land surface location and $d_{sw}(x, y)$ [L] is the surface water body depth. To accurately obtain the recharge rate across the water table, a hybrid saturated-unsaturated model is required [*An et al.*, 2010]. Standard numerical models including MIKE-SHE, HyroGeoSphere and Hydrus 2-D use the hybrid saturated-unsaturated model with a fixed mesh. Due to a difference mathematical behavior below and above a priori unknown water table surface, a different mesh discretization for these two zones are required. Therefore implementation of moving water table interface may be challenging

inside a fixed mesh, particularly in dry conditions. Due to the complexity of such a coupled model, typically the unsaturated zone is neglected and a moving mesh is used to properly represent the behavior of the a priori unknown water table surface in a fully saturated model [as is done in e.g., Flonet and Seco-Flow 3D models]. Using moving mesh scheme, mesh adaptation due to free surface is challenging and, particularly for high material contrast, may cause a numerical instability. The mesh discretization should be ideally modified and transformed at each iteration. This is more problematic in the presence of seepage face or groundwater ridge. In addition, researchers have experimentally and numerically shown that ignoring flow in unsaturated zone can have an effect on the magnitude of subsurface flow toward a stream and upon the water table location [*Berkowitz et al.*, 2004; *Romanoa et al.*, 1999].

To implement equations (2-11), (2-12) and (2-13), typically an iterative scheme with an initial guess of the phreatic surface is used while constant head (Dirichlet) and flux (Newman) boundary conditions are implemented along seepage face/surface water locations and recharge zones, respectively. A zero pressure head condition is imposed at each iteration to modify 1) the a priori unknown phreatic surface location along recharge zones and 2) the location of seepage faces. This type of boundary condition may be termed a constrained free boundary since the location of intersection with the ground surface is not known a priori and the surface is, strictly speaking, only a free surface in recharge zones. In other words, in 2-D simulation the location of hinge node (or in 3-D hinge line) which is a separating element between the seepage face/surface water and recharge zone is not known a priori. Mesh-based numerical models deal with moving mesh issues related to this constrained free boundary problem [*An et al.*, 2010; *Knupp*, 1996]. At each iteration which the free surface is moved, an updated mesh is required. Moving the mesh can disrupt the alignment between the coordinate lines and principle axes of the conductivity tensor. In addition, it is necessary to interpolate spatially-varying aquifer properties, such as conductivity, to the correct value within a moving-mesh cell [*Knupp*, 1996]. Moving mesh issues are much more challenging in hybrid saturated-unsaturated models [e.g., *An et al.*, 2010]. A simpler treatment of free boundary problem has been suggested by *Boussinesq* [1872] where hydrostatic condition is assumed in a 2-D Dupuit - Forchheimer model. This leads to a non-linear governing equation and at the same time the accuracy of the model in the vicinity of 3-D flow features including pumping well, river and lake may not be acceptable [e.g., *Ameli and Craig*, 2014; *Kacimov*, 2000].

Implementation of the free boundary condition along the water table is cumbersome for analytical and semi-analytical models as well. However, grid-free analytical or semi-analytical approaches may circumvent the issues related to moving mesh in discrete numerical methods. In steady semi-analytical models a simplified form of equation (2-12) (second order and transient terms are ignored) can be used as

$$(k_z + RE)(\frac{\partial\, h}{\partial z}) = RE \tag{2-14}$$

This equation with the assumption of $RE<<<k_z$ which is valid for examples presented in this thesis can be represented as

$$(k_z)(\frac{\partial\, h}{\partial z}) = RE \tag{2-15}$$

Luther [1998] and *Luther and Haitjema* [2000] employed equation (2-15) with a zero recharge assumption accompanied with the previously mentioned iterative scheme. Alternatively, *Tristscher et al.* [2001] minimized the variational formulation generated from the root mean square errors of the flux condition constrained to a zero pressure head. However, mentioned techniques must assume the location of seepage faces prior to the simulation or not have seepage faces present. In other words, a portion of water table is kept in a fixed state. These methods therefore cannot be used to determine the location of seepage faces or other intersections with the surface. Similar to the implementation of the free boundary in numerical models, a robust iterative algorithm with the ability to address phreatic surface as a constrained non-linear free boundary condition is a preferred course of action. In this thesis efficient iterative schemes are used to implement equations (2-11& 2-13 &2-15) along the a priori unknown phreatic surface.

Heterogeneity and anisotropy

Material properties of natural aquifers are usually heterogeneous. This heterogeneity is caused by the redepostion of different types of soil and sediment in an aquifer. The heterogeneity can be vertical, horizontal or both and is typically addressed rather easily with numerical methods, but presents a challenge with analytical techniques, which typically require regular system geometry and/or homogeneity. However, recently vertical heterogeneity or stratification has been addressed quite successfully using multi-layer analytical models [e.g., *Bakker et al.*, 2005; *Wong and Craig*, 2010].

Anisotropy may be treated by coordinate transformation to isotropic equivalents in numerical and analytical models [e.g., *Craig*, 2008; *Winter and Pfannkuch*, 1984], but this transformation may become complicated in systems with heterogeneity and/or complex geometry.

Complex geometry

Aquifers are geometrically complex in finite horizontal and vertical extents. Irregular geometry of bedrock, interfaces between different soil layers and land surface topography, are inseparable elements of each groundwater system. Treatment of such complexities is typically out of reach of classical analytical approaches, though some notable exceptions exist [*Read and Volker*, 1993; *Read and Broadbridge*, 1996; *Wong and Craig*, 2010]

2.4.1 Numerical models for groundwater-surface water interaction

As stated above, discrete numerical models have been typically used to simulate groundwater-surface water interaction in complex aquifers [e.g., *Cardenas and Jiang*, 2010; *Larabi and De Smedt*, 1997; *Okkonen and Kløve*, 2011; *Oz et al.*, 2011; *Patel et al.*, 1998; *Therrien et al.*, 2008]. However, it is known that the efficiency of numerical approaches depend upon the resolution and structure of the underlying grid or mesh. This compromises the numerical schemes appropriateness in addressing free boundary problems [*An et al.*, 2010; *Knupp*, 1996], and may lead to poor representation of the geometry and properties of surface water bodies [*Mehl and Hill*, 2010; *Rushton*, 2007; *Sophocleous*, 2002; *Townley and Trefry*, 2000] and pumping wells [*Moore et al.*, 2012; *Patel et al.*, 2010] in multi-scale problems.

The geometry and property of surface water bodies (e.g., lakes, rivers) and their underlying sediment layers may not be accurately represented using mesh based schemes, because a practical mesh spacing in regional groundwater-surface water models is usually considerably larger than these small scale features [*Rushton*, 2007]. In cases such as these, a simple 1-D approximation (e.g., use of a river coefficient) is usually used to incorporate the effect of the sediment of these features [e.g., *Nield et al.*, 1994; *Rushton*, 2007]. Similarly, pumping well(s) with arbitrary orientations are difficult to address with discrete models [*Patel et al.*, 1998; *Patel et al.*, 2010]. The local interaction between pumping wells and neighboring surface water bodies is three dimensional. Due to the small diameter of radial collector (RC) wells (15 cm to 50 cm), a high resolution 3-D discretization is difficult to apply along well screens. Furthermore, when the laterals of RC wells do not align with the generated grids of numerical models specific care is required to incorporate this misalignment [*Moore et al.*,

2012]. Therefore, numerical models may be inefficient to test all (RC) well configurations and determine their optimum design for RBF and pump and treat processes [*Patel et al.*, 2010].

Variation of head and discharge along well screens, skin effects and head losses inside the collectors complicate the boundary condition implementation along each collector screen. There are three common approaches to treat this unique boundary condition along each collector screen: uniform inflow [*Tsou et al.*, 2010; *Zhan and Zlotnik*, 2002; *Zhan et al.*, 2001], uniform head [*Moore et al.*, 2012; *Patel et al.*, 2010; *Samani et al.*, 2006] or constrained non-uniform head [*Bakker et al.*, 2005]. The first representation of the well screen boundary condition is unrealistic particularly for the application to long horizontal wells. The second approach, on the other hand, can be valid when the flow condition inside the well is laminar with negligible head losses [*Moore et al.*, 2012]. Head losses can be considered in the third approach (preferred) [*Bakker et al.*, 2005]. Mesh-based numerical models such as MODFLOW roughly approximate this boundary condition using a head dependent boundary condition, often using conductance factor [*Patel et al.*, 1998].

2.4.2 Semi - analytical models

Grid-free semi-analytical methods, which benefit from the strength of both analytical and numerical schemes, can be used to address complex problems. For linear or linearized problems, these methods have the capacity to produce continuous and differentiable solutions which satisfy the governing equation(s) exactly. Under many circumstances, they can provide helpful insights into ground water-surface water exchanges in 2-D and 3-D [*Haitjema*, 1995]. These methods (e.g., series solutions, separation of variables, Laplace, Fourier and Hankel transforms, etc.) may be augmented with a simple numerical technique such as weighted Least Squares minimization (WLS) or numerical inversion to address geometrically or mathematically complex problems [e.g., *Craig*, 2008; *Luther and Haitjema*, 1999; *Mishra and Neuman*, 2010; *Mishra et al.*, 2013; *Read and Volker*, 1993; *Tartakovsky and Neuman*, 2007; *Tristscher et al.*, 2001; *Wong and Craig*, 2010].

To date, researchers have successfully used semi-analytical Laplace-Fourier double transform scheme to address 2-D stream-aquifer interaction in a semi-confined aquifer with a regular geometry and trivial boundary conditions [*Hunt*, 2003; 2009; *Ward and Lough*, 2011]. The semi-analytical series solution method has also been extended to address topography driven saturated flow in naturally complex homogenous [*Read and Volker*, 1993; *Wörman et al.*, 2006] and multi-layer aquifers [*Craig*, 2008; *Wong and Craig*, 2010]. This method has been also used to address free boundary 2-D

saturated-unsaturated steady-state model in homogenous systems [*Tristscher et al.*, 2001]. In spite of having an ability to address naturally complex geometry and free boundary condition, the series solution approach has not been extended to address free boundary 2-D and 3-D saturated and saturated-unsaturated steady flow in geometrically complex stratified unconfined aquifers.

The semi-analytical analytic element method (AEM) is also recognized as a robust alternative to mesh-based numerical models for the simulation of large-scale regional flow without loss of local resolution [*Hunt*, 2006; *Moore et al.*, 2012]. AEM is also able to easily refine or enlarge the computational domain without redesigning the computational grid; this is useful for screening or quick hydrologic analysis and stepwise modeling [*Dripps et al.*, 2006; *Hunt*, 2006; *Strack*, 1989]. A simple initial model can be gradually upgraded to a more complex model as more data become available instead of replacing the initial model in stepwise modeling [*Hunt*, 2006]. AEM has also been used as a numerical laboratory to assess the theories behind the estimation of effective conductivity and dispersion coefficients in highly heterogeneous formations [*Barnes and Janković*, 1999; *Janković et al.*, 2003]. Such simulations are impossible using mesh-based numerical methods. AEM, in addition, has been widely used to address regional groundwater-surface water interaction [*Haitjema et al.*, 2010; *Hunt et al.*, 2003a; *Simpkins*, 2006], mostly in 2-D systems. In most cases, the Dupuit-Forchheimer assumption is applied when applying AEM to groundwater-surface water interaction problems [*Haitjema*, 1995; *Haitjema et al.*, 2010], where surface water bodies (e.g., lakes and streams) are represented by 2-D line sinks. In this case, to approximate 3-D details near surface water bodies, a simple Cauchy boundary condition accompanied by a conductance factor approach has typically been used [*Haitjema et al.*, 2010; *Moore et al.*, 2012; *Patel et al.*, 2010], which may not be able to accurately mimic the behavior of groundwater in the vicinity of surface water features. In addition, the surface water geometry and properties may not be well represented using 2-D line sinks.

By using distributed singularities, AEM is able to incorporate pumping wells without horizontal or vertical grid discretization. Fully 3-D flow close to wells screen can be emulated by placing 3-D line sinks with variable strengths along a pumping well. Using AEM, multiple researchers have addressed 3-D flow toward partially penetrating vertical, horizontal and slanted pumping well(s) such as is needed for design of radial collector wells [e.g., *Bakker et al.*, 2005; *Luther and Haitjema*, 1999; *Steward*, 1999; *Steward and Jin*, 2001; 2003]. Compared to numerical schemes, grid-free AEM provides a large degree of flexibility in placement of collectors during the design phase when different numbers, orientations, and lengths of collectors must be considered. In spite of these

advantages, the treatment of phreatic surface using AEM may be challenging where hundreds of point and line sinks are placed above the modeled domain [*Luther and Haitjema*, 1999; *Luther and Haitjema*, 2000]. There are no unique guidelines about the location, type and number of the required singularities to properly address the phreatic surface. Modeling of vertical stratification may also be challenging using AEM. The quasi 3-D FDM-AEM model developed by *Bakker et al.* [2005] is able to model a group of horizontal pumping wells in a stratified confined aquifer with considering the effect of skin and head losses along the well screens. It has been shown that this quasi 3-D model can emulate the 3-D behavior of pumping wells with a high degree of accuracy [*Moore et al.*, 2012]; however, vertical discretization is required to represent vertical resistance using finite difference which may limit the application of the model to a confined aquifer with a simple geometry and parallel layer stratification. Likewise, the phreatic surface and its conditions to the ground surface are not properly handled in such pseudo-3D models.

As *Hunt* [2006] has suggested in his short review, AEM needs to be further developed to better address three dimensional, transient and multi-aquifer flow problems. In addition, surface water features and phreatic surface (including seepage faces) have to be efficiently considered. Improved methods can be useful for determining well water origins and assessing surface water impacted by pumping in naturally complex aquifers. The percentage of well water that comes from surface water bodies can also be estimated which may provide understanding in contaminant risk management and potential ecosystem disruption.

Chapter 3
Semi-analytical series solution and analytic element method

3.1 Introduction

In this chapter the mathematical background behind the development of semi-analytical approaches used in this thesis are explained. Their limitations and the possible ways to mitigate these limitations are presented.

3.2 Series solutions

Over a finite domain, any arbitrary smooth and continuous function can be represented by infinite terms of orthogonal series (basis functions). Relying upon this strength of orthogonal series, separation of variables and series solution methods have been applied by many researchers to analytically solve separable linear governing equation [e.g., *Freeze and Witherspoon*, 1967; *Powers et al.*, 1967; *Selim*, 1975]. Basis functions are typically generated from the method of separation of variables and therefore satisfy the linear governing equation exactly. Using the method of separation of variables, for example, to solve the 3-D Laplace equation (Equation (2-4)), a solution of the following form is assumed

$$\phi(x,y,z) = U(x)V(y)W(z) \tag{3-1}$$

After substitution into the Laplace equation, we obtain three ordinary differential equations for $U(x)$, $V(y)$ and $W(z)$:

$$U'' + \omega^2 U = 0 \quad \& \quad V'' + \beta^2 V = 0 \quad \& \quad W'' - \gamma^2 W = 0 \tag{3-2}$$

where $\gamma^2 = \omega^2 + \beta^2$

Here ω^2, β^2 and γ^2 are Eigenvalues and $U(x)$, $V(y)$ and $W(z)$ are Eigenfunctions of the Laplace equation. By solving the preceding ODEs and using superposition of solutions for a range of values for ω and β, a discharge potential function of the following form is obtained as a flexible solution to the 3-D Laplace equation:

$$\phi \quad (x, y, z) = \sum_{j=0}^{\infty} \sum_{n=0}^{\infty} cos\, \omega_j x\, cos\, \beta_n y\, [A_{jn} cosh(\gamma_{jn} z) + B_{jn} sinh(\gamma_{jn} z)] \tag{3-3}$$

In the preceding equation, j and n are coefficient indexes approximation in x and y direction respectively (in practice, the series is truncated to N and J series terms in each direction). Eigen values (${\omega_j}^2$, ${\beta_n}^2$, ${\gamma_{jn}}^2$) are typically selected to satisfy boundary conditions at the sides of the domain (in this thesis no-flow conditions are assumed along all sides of the modeled domain) as is later discussed in chapter 5. The unknown coefficients A_{jn}, B_{jn} in equation (3-3) are arbitrary and may be calculated to satisfy continuity and boundary conditions.

Based on the orthogonality of basis functions, unknown coefficients may be obtained using the Euler formulas (similar to the determination of the Fourier coefficients in a Fourier series approach)[*Freeze and Witherspoon*, 1967]. However, this treatment of boundary and continuity conditions is limited to application to problems with a regular (e.g., square or rectangular) domain [*Selim*, 1975; *Wong and Craig*, 2010]. Indeed along irregular boundaries, the basis functions are, strictly speaking, non-orthogonal such that the Euler formulas are not valid and alternative approaches must be deployed. The Gram-Schmidt orthonormalization scheme used by e.g., *Selim* [1975] slightly mitigated this issue, but it is overly complicated.

Read and Volker [1993] derived a simpler least squares (LS) approach for simulating flow in single-layer aquifer systems with irregular boundaries at the top and the bottom using series solutions. This LS approach was employed by *Craig* [2008] to consider the effects of an arbitrary number of multiple parallel or syncline layers. *Wong and Craig* [2010] further extended this approach to address topography driven saturated flow in a geometrically complex stratified unconfined aquifer. Using LS, unknown series solution coefficients A_{jn}, B_{jn} are calculated by minimizing the total sum of squared errors (TSSE) in all boundary and continuity conditions at a set of control points. These control points are located along the layer interfaces, topographic surface, bottom boundary, and/or the phreatic surface.

3.3 Analytic Element Method (AEM)

The analytic element method (AEM) initially developed by *Strack and Haitjema* [1981] is a semi-analytical method used for the solution of linear partial differential equations including the Laplace, the Poisson, and the modified Helmholtz equations. In a fashion similar to the series solution method discussed above, this approach does not rely upon discretization of volumes or areas in the modeled system; only internal and external boundaries are discretized using a simple numerical collocation or least squares algorithm.

The basic idea behind AEM is the representation of flow features by geometric elements, such as point and line sinks. For the purpose of solving steady-state groundwater flow, each element has an analytic solution which satisfies, for example, the Laplace equation [*Strack*, 1989]. In a manner similar to the series solution the influence of analytic elements on the surrounding flow field can be defined in terms of discharge potential, ϕ [L^2T^{-1}], as follows;

$$\phi(x,y,z) = \sum_i \sigma_i F_i(x,y,z) \tag{3-4}$$

The influence function, F_i[L^2T^{-1}], represents the unit contribution of each element (i) to total discharge potential of the flow field where σ_i is the strength coefficient for each element. Influence functions are generally designed to generate a specific form of discontinuity in potential or its gradient along lines, curves, or surfaces, but be continuous elsewhere. The influence function for various ground water features and governing equations have been developed by many researchers after *Strack and Haitjema* [1981] initially used AEM for the simulation of groundwater problems.

Here, the primary interest is in utilizing 3-D AEM techniques. In 3-D, most AEM solutions are generated from the elementary solution for a point sink in an infinite domain. Analogous to a point charge in electromagnetic theory, a 3-D ground water point sink contribution to total discharge potential is

$$\phi(x,y,z) = -\frac{\sigma}{4\pi\left[\left(x-x_p\right)^2 + \left(y-y_p\right)^2 + \left(z-z_p\right)^2\right]^{\frac{1}{2}}} \tag{3-5}$$

Where x_p, y_p and z_p are the location of the point sinks in the global coordinate system. By integrating the preceding equation along a line segment with a known sink distribution, the specific

discharge contribution of a line sink can be obtained. A line sink is able to mimic the behavior of an arbitrary-oriented pumping well. There are various formulations for representing a pumping well using a line sink in the literature, most of which differ in the strength distribution function along the line sink [*Haitjema*, 1995; *Luther and Haitjema*, 1999; *Luther and Haitjema*, 2000; *Luther*, 1998; *Steward and Jin*, 2001]. Here pumping wells will be modeled in a manner similar to *Steward and Jin* [2003]. Rather than considering a complex strength distribution function along the well, they subdivided each well (line element) into a set of consecutive segments and represented the discharge potential of each segment in its local coordinate system. The discharge potential correspond to i^{th} segment of a line element, i.e., ϕ_w^i, is then obtained by integrating the potential for a point sink along the segment with a length of $2l$ (here $\bar{x}$, $\bar{y}$ and $\bar{z}$ are local coordinates of each segment where $\bar{x}$ represents the segment axis) as follows:

$$\phi_w^i(\bar{x},\bar{y},\bar{z}) = -\frac{1}{4\pi}\int_{-l}^{l} \frac{{\sigma_0}^i}{[(\bar{x}-\bar{x}')^2+(\bar{y})^2+(\bar{z})^2]^{\frac{1}{2}}}\, d\bar{x}' \qquad i = 1 \dots N_s \tag{3-6}$$

where N_s and ${\sigma_0}^i$ are the number of segments along a line element and constant strength of each segment, respectively. Although *Steward and Jin* [2003] have applied linearly varying strength along each segment of the line element, in this thesis a constant strength for each segment is used as the contribution of the linearly varied strength term to the total discharge potential is negligible when the segment length is small enough (as the number of segments increases, the required linearly varied strength along each arm can be emulated using segments with constant head). *Steward and Jin* [2003] have generated a closed form expression for each segment of a line element in its local coordinate as

$$\phi_w^i(\bar{x},\bar{y},\bar{z}) = -\frac{{\sigma_0}^i}{4\pi}\ln\frac{[(\bar{x}+L)^2+(\bar{y})^2+(\bar{z})^2]^{\frac{1}{2}}+(\bar{x}+L)}{[(\bar{x}-L)^2+(\bar{y})^2+(\bar{z})^2]^{\frac{1}{2}}+(\bar{x}-L)} \qquad i = 1 \dots N_s \tag{3-7}$$

3.4 Gibbs phenomenon

Gibbs phenomenon is a common issue with series-based solution methods and occurs whenever an orthogonal series (e.g., a Fourier series) is used to approximate a function with a discontinuity (in function or its gradient). In other words, sharp changes in geometry of the layers and/or boundary conditions implemented across an interface can exacerbate Gibbs phenomenon [for further details see

Nahin, 2011]. Strictly speaking, such discontinuities lead to singular behaviour which cannot be represented using separable solutions. This issue has been reported in research studies which used series-based approaches to address groundwater flow in geometrically complex systems [e.g., *Wong and Craig*, 2010]. In this thesis, Gibbs phenomenon predominantly occurs due to sharp changes in geometry or boundary condition. Such problems may ideally be rectified by supplementing standard basis functions with special 'supplemental solutions', which handle local departures from generally smooth solutions. Here, such an approach is discussed for 1-D curve fitting of a discontinuous function using a discrete Fourier series. In higher dimensions, when supplemental solutions must additionally satisfy the governing equation, the problem becomes significantly more complex.

Consider a 1-D function ($G(x)$) with an abrupt change at $x = 0$ as:

$$G(x) = \begin{cases} \sin(x) & x < 0 \\ 10\cos(10x) & \delta_x > x > 0 \\ \sin(x - \delta_x) & x > \delta_x \end{cases} \tag{3-8}$$

where δ_x is equal to 0.25. Figure 3-1a shows the function $G(x)$ in addition to the fitted 1-D curve to $G(x)$ generated from a Fourier series in the form

$$F(x) = \sum_{n=0}^{N} A_n \cos\left(\frac{nx}{8}\right) + B_n \sin\left(\frac{nx}{8}\right) \tag{3-9}$$

where N =10 and a simple least Squares algorithm through 20 data points (control points) is used for the curve fitting as follows

$$SSE = \sum_{i=1}^{20} (F(x_i) - G(x_i))^2 \rightarrow Min \tag{3-10}$$

Figure 3-1b shows the absolute error at 80 non-control points normalized with respect to the maximum value of function $G(x)$. Apparently the sharp change can not be emulated accurately. Even worse this sharp change compromises the efficiency of Fourier series in fitting the remaining parts of function $G(x)$.

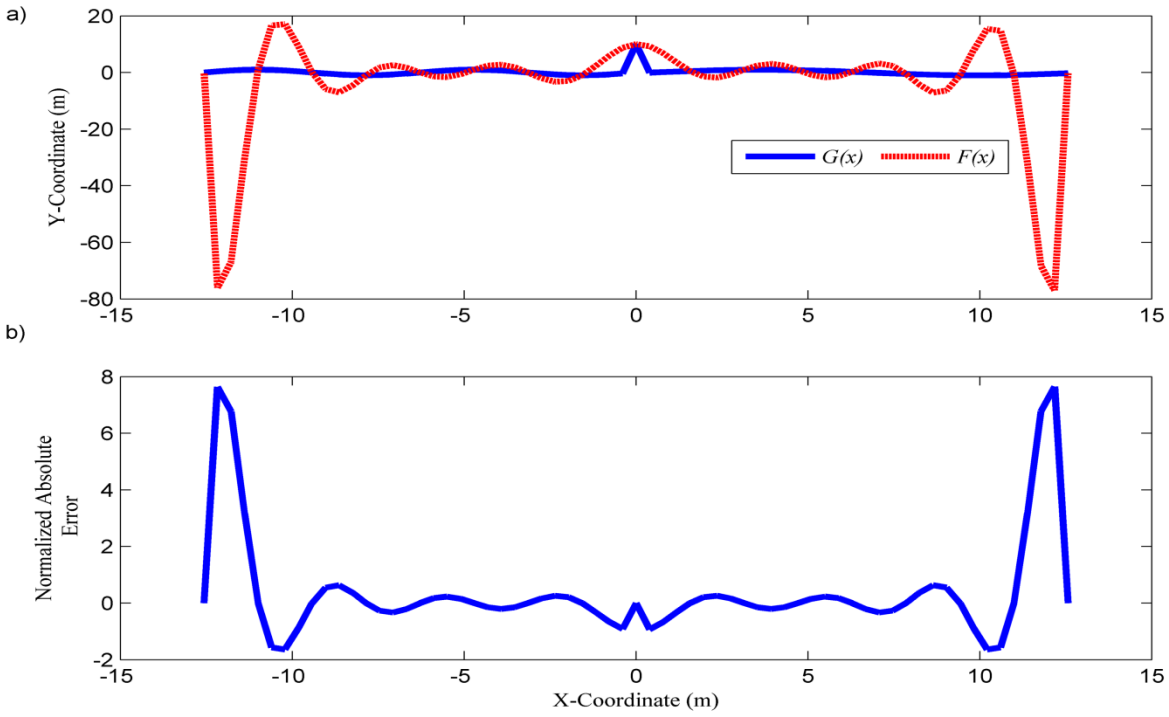

Figure 3-1. Performance of discrete Fourier series in curve fitting of function $G(x)$ using least square algorithm. a) Original and fitted function, b) normalized least squares absolute error.

Here an abrupt change is emulated by the combination of two Heaviside step functions as follows (Dirac delta function when *k* approaches infinity)

$$\delta(x,a) = \begin{cases} \dfrac{1}{1+e^{2k(x-a)}} & x < a \\ \dfrac{1}{1+e^{-2k(x-a)}} & x > a \end{cases} \tag{3-11}$$

where the abrupt change occurs at $x = a$. By augmenting the Fourier series (Equation (3-9)) with the proceeding function, an abrupt change at x = 0 can properly be addressed without negative effect on the remaining part of the fitted curve. The resulting augmented equation is as follows;

$$F'(x) = \delta(x,0) + \sum_{n=1}^{N} A_n \cos\left(\frac{nx}{8}\right) + B_n \sin\left(\frac{nx}{8}\right) \tag{3-12}$$

With the same number of Fourier series terms and control points as the first example, figure 3-2a indicates that the augmented $F'(x)$ can provide a better fit to the original function than $F(x)$. Figure 3-2b shows the normalized absolute error at 80 non-control points.

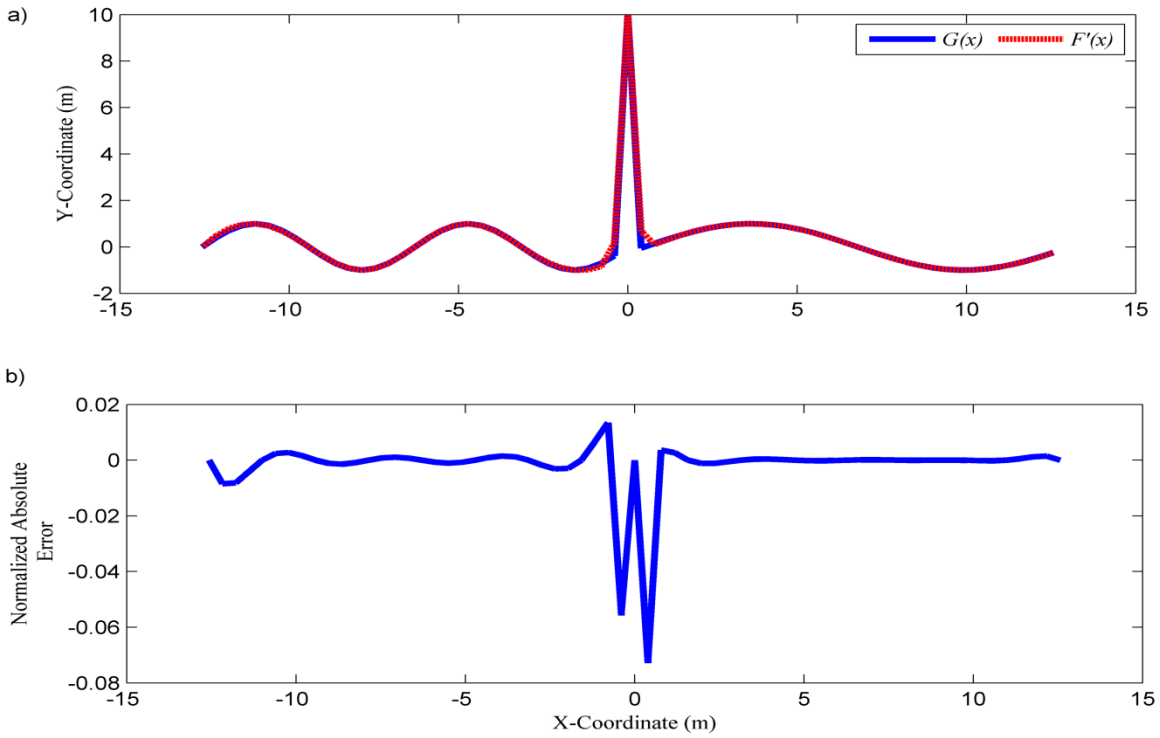

Figure 3-2. Performance of the augmented Fourier series with a supplemental function in curve fitting of function *G(x)* using least square algorithm. a) Original and fitted function, b) normalized least squares absolute error.

Analogous to the Fourier series, series solutions can be augmented to handle local departures from generally smooth solutions to the governing equation of groundwater flow. However, developing 2-D and 3-D supplemental functions which are discontinuous at some specific points and, at the same time, satisfying the governing equation is challenging. Alternative approaches may otherwise be employed to tackle Gibbs phenomenon. For example, some degree of function smoothing can reduce the error caused by Gibbs phenomenon as is discussed in chapter 5. Using weighted least squares where different weighting coefficients are considered for each control point is another possible way to address Gibbs phenomenon as is discussed in chapter 4. However, both are stopgap measures which may not address the core problem.

Chapter 4
Series solutions for saturated-unsaturated flow in multi-layer unconfined aquifers

This chapter is based on the following published article. For the coherence of this thesis, changes have been made in the introduction, background, method and conclusion sections of this publication. References are presented at the end of the thesis.

Ameli, A. A., J. R. Craig, and S. Wong (2013), Series solutions for saturated-unsaturated flow in multi-layer unconfined aquifers, *Adv. Water Resour.*, *60*, 24-33, DOI**:** 10.1016/j.advwatres.2013.07.004.

4.1 Introduction

In many cases, the influence of the unsaturated zone must be included in a groundwater-surface water interaction model. Analytical and semi-analytical approaches typically neglect or simplify the unsaturated zone and capillary fringe flow. The purpose of the chapter is to extend semi-analytical series solution approaches for application to 2-D steady-state free boundary saturated-unsaturated subsurface flow induced by spatially variable surface fluxes in geometrically complex homogenous and stratified unconfined aquifers. The capillary fringe zone, unsaturated zone, groundwater zone and their interactions are incorporated. Continuous solutions for pressure in the saturated and unsaturated zone are determined iteratively, as is the location of the water table surface. The water table and capillary fringe are allowed to intersect stratigraphic interfaces. The model can be used to provide a conceptual understanding of the influence of factors on unsaturated flow behavior and a priori unknown water table elevation.

4.2 Background

To date, researchers have used series solutions to independently address the free boundary saturated-unsaturated steady flow in homogenous systems [*Tristscher et al.*, 2001] and topography-driven saturated flow in heterogeneous aquifers with geometrically complex stratification [*Wong and Craig*, 2010]. However, these issues have never been addressed concurrently. In addition, a robust regional subsurface model requires consideration of the interaction between subsurface flow and the topographic surface. Existing semi-analytical models have paid scarce attention to this issue, and also

have neglected the capillary fringe zone [*Mishra and Neuman*, 2010; *Tristscher et al.*, 2001]. However, researchers have experimentally and numerically shown that horizontal flow in this zone can have an effect on the magnitude of subsurface flow toward a stream and upon the water table location [*Berkowitz et al.*, 2004; *Romanoa et al.*, 1999].

4.3 Problem statement

Figure 4-1 shows the general schematic of a stratified soil profile that can be modeled using methods derived herein. An aquifer with length L is subdivided into M layers with arbitrary geometry, each with saturated conductivity K_m^s. Layers are indexed downward from m=1 to m=M and are bounded by the curve $z_m(x)$ above and $z_{m+1}(x)$ below. The bottom bedrock, $z_{M+1}(x)$, and sides of the aquifer are impermeable. The topographic surface, $z_1(x)$, is subject to a specified surface flux distribution function (which may be calculated from rainfall, evaporation and transpiration) and/or a Dirichlet condition along surface water bodies (e.g., a river with specified width and surface elevation). These conditions are easily amended to account for the presence of multiple surface water features. The saturated-unsaturated interface or top of capillary fringe ($z_{\mathrm{cf}}(x)$) is a moving boundary which defines the location of the top of the saturated zone and the bottom of unsaturated zone. The water table is defined as a boundary with zero pressure head. All layer interfaces, the topographic surface, and the bedrock surface are specified prior to solution.

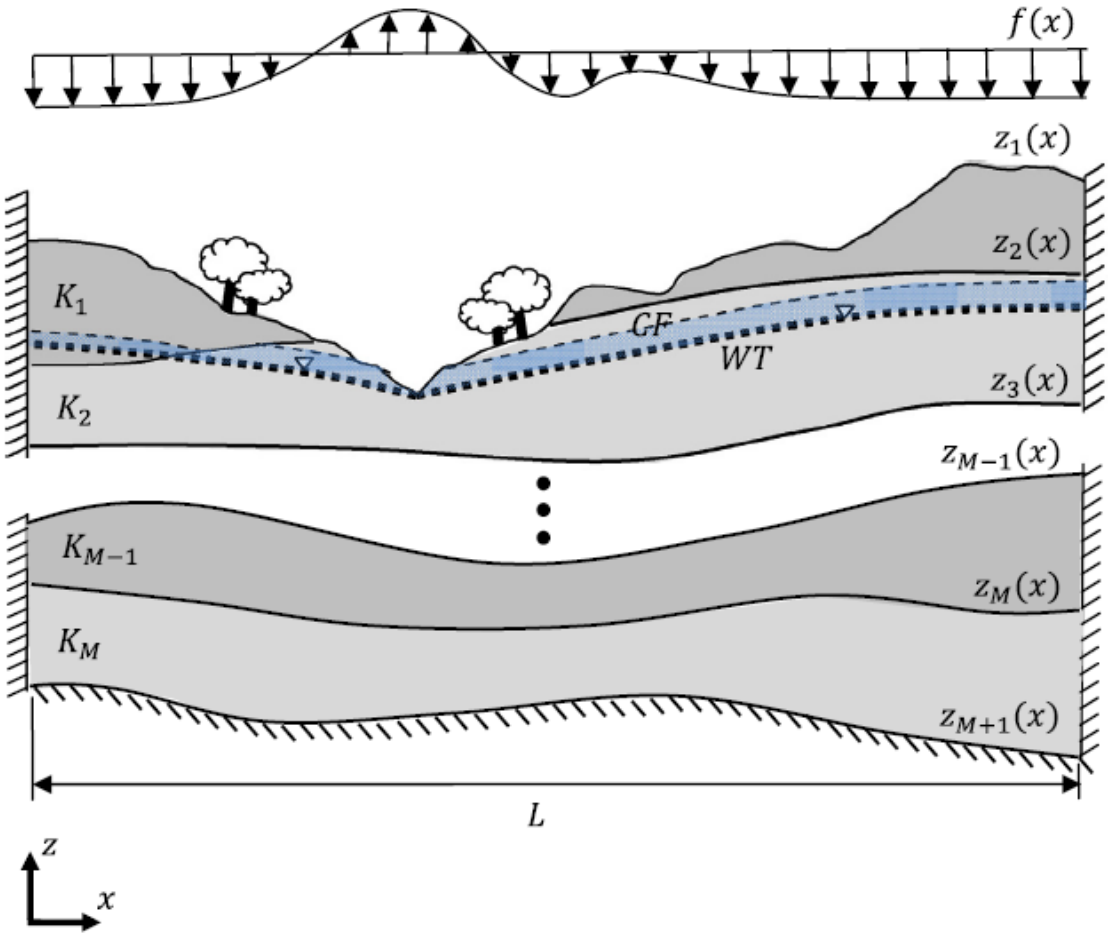

Figure 4-1. Layout of the general problem. M layers are separated by the layer interfaces $z_m(x)$, with $z_{(M+1)}(x)$ corresponding to the bottom bedrock and $z_1(x)$ corresponding to the topography surface. *CF* corresponding to the boundary between saturated and unsaturated zones that similar to water table location *WT* is unknown priori. Image from *Ameli et al.* [2013].

Here the M-Layer system is divided into two zones: the saturated zone (with M_s layers) and unsaturated zone (with M_u layers). The relationship between M, M_s and M_u is a priori unknown and will be discerned through the solution of the problem, since the top of capillary fringe might intersect multiple layers. Note that hereafter (s) and (u) describe saturated and unsaturated properties/variables.

As discussed in section 2.3, subsurface flow in each layer of saturated and unsaturated zones are governed by the following equations in terms of a discharge potential:

$$\frac{\partial^2 \phi_m^s}{\partial x^2} + \frac{\partial^2 \phi_m^s}{\partial z^2} = 0 \quad \text{for } m = M^*, \dots, M \tag{4-1}$$

$$\frac{\partial^2 \phi_m^u}{\partial x^2} + \frac{\partial^2 \phi_m^u}{\partial z^2} + \alpha_m \frac{\partial \phi_m^u}{\partial z} = 0 \text{ for } m = 1, \dots, M_u \tag{4-2}$$

where $M^*$is the uppermost layer where the top of capillary fringe interface (z_{cf}) exists.

For both unsaturated and saturated 2-D steady flow, the stream function formulation will be useful for applying some of the continuity and boundary conditions. The stream function formulation can be obtained using a generalized form of the Cauchy-Riemann equations for unsaturated flow [*Read and Broadbridge*, 1996],

$$\frac{\partial \psi_m^u}{\partial x} = -\frac{\partial \phi_m^u}{\partial z} - \alpha_m \phi_m^u \text{ and } \frac{\partial \psi_m^u}{\partial z} = \frac{\partial \phi_m^u}{\partial x} \text{ for } m = 1, \dots, M_u \tag{4-3}$$

and Cauchy-Riemann equations for saturated flow,

$$\frac{\partial \psi_m^s}{\partial x} = -\frac{\partial \phi_m^s}{\partial z} \quad \text{and} \quad \frac{\partial \psi_m^s}{\partial z} = \frac{\partial \phi_m^s}{\partial x} \text{ for } m = M^*, \dots, M \tag{4-4}$$

where ψ_m^u and ψ_m^s are unsaturated and saturated stream function of the m^{th} layer respectively. The unsaturated and saturated governing equations are equivalent to the following equations in terms of the stream function for each layer of unsaturated and saturated zones:

$$\frac{\partial^2 \psi_m^u}{\partial x^2} + \frac{\partial^2 \psi_m^u}{\partial z^2} + \alpha_m \frac{\partial \psi_m^u}{\partial z} = 0 \text{ for } m = 1, \dots, M_u \tag{4-5}$$

$$\frac{\partial^2 \psi_m^s}{\partial x^2} + \frac{\partial^2 \psi_m^s}{\partial z^2} = 0 \text{ for } m = M^*, \dots, M \tag{4-6}$$

The normal first order derivative of a 2-D function, *T*, across an interface can be decomposed into vertical and horizontal components as

$$\frac{\partial T}{\partial \eta} = \frac{\frac{\partial T}{\partial z} - \frac{d\hat{z}}{dx}\frac{\partial T}{\partial x}}{\sqrt{1 + (\frac{d\hat{z}}{dx})^2}} \tag{4-7}$$

When the cosine of the slope angle describing each evaluation curve approximated as unity (the denominator of the equation 4-7), in a manner similar to *Read and Broadbridge* [1996] for the vadose zone and *Wong and Craig* [2010] for the saturated zone, the normal first order potential derivatives across unsaturated and saturated interfaces can be represented as follows:

$$\frac{\partial \phi_m^u}{\partial \eta} = \frac{\partial \phi_m^u}{\partial z} - \frac{d\hat{z}}{dx}\frac{\partial \phi_m^u}{\partial x} + \alpha_m \phi_m^u \tag{4-8a}$$

$$\frac{\partial \phi_m^s}{\partial \eta} = \frac{\partial \phi_m^s}{\partial z} - \frac{d\hat{z}}{dx}\frac{\partial \phi_m^s}{\partial x} \tag{4-8b}$$

where η is the coordinate normal to each interface represented by the function $\hat{z}(x)$, which is either a layer interface $z_m(x)$ or the top of capillary fringe $z_{\mathrm{cf}}(x)$. Using the above equations (Equations (4-8a) and (4-8b)) and Cauchy-Riemann equations (Equations (4-3) and (4-4)) the boundary and continuity conditions along unsaturated and saturated interfaces can be represented in terms of either potential or stream function.

Across the sides of the domain in both unsaturated and saturated zones, no-flow conditions in x-direction are imposed. The stream function equivalent formulas for unsaturated and saturated zones used in current chapter are:

$$\psi_m^u(0, z\ ) = 0 \text{ for } m = 1, \dots, M_u \tag{4-7a}$$

$$\psi_m^u(L, z\ ) = 0 \text{ for } m = 1, \dots, M_u \tag{4-9b}$$

$$\psi_m^s(0, z\ ) = 0 \text{ for } m = M^*, \dots, M \tag{4-8a}$$

$$\psi_m^s(L, z\ ) = 0 \text{ for } m = M^*, \dots, M \tag{4-10b}$$

where L is the length of the domain (Figure 4-1). The topographic surface boundary condition with the arbitrary infiltration-evapotranspiration function $f(x)$[$\mathrm{LT^{-1}}$] is:

$$\frac{\partial \phi_1^u}{\partial \eta}\big(x, z_1(x)\big) = f(x) \tag{4-9a}$$

or, using the stream function formulation:

$$\frac{\partial \psi_1^u}{\partial x} + \frac{dz_1(x)}{dx}\frac{\partial \psi_1^u}{\partial z} = -f(x) \tag{4-11b}$$

where $f(x)$ is taken as positive for infiltration and negative for evapotranspiration. Along surface water features a uniform hydraulic head is applied. The continuity of flux along the vadose zone layers interfaces for $m = 2, \dots, M_u$ can be represented as its stream function equivalent:

$$\psi_m^u\big(x, z_m(x)\big) = \psi_{m-1}^u(x, z_m(x)) \tag{4-10}$$

Similarly, the continuity of head φ^u along vadose zone interfaces in terms of the Kirchhoff potential is

$$\frac{1}{\alpha_m}\ln\left(\frac{\alpha_m \phi_m^u}{K_m^s}\right) = \frac{1}{\alpha_{m-1}}\ln\left(\frac{\alpha_{m-1}\phi_{m-1}^u}{K_{m-1}^s}\right) \tag{4-11}$$

For the saturated zone, the continuity of flux (in terms of stream function) and pressure head (in terms of discharge potential) along each saturated layer interface (for $m = M^* + 1, \dots, M$) can be represented as:

$$\psi_m^s\big(x, z_m(x)\big) = \psi_{m-1}^s(x, z_m(x)) \tag{4-12}$$

$$\frac{\phi_m^s\big(x, z_m(x)\big)}{K_m^s} = \frac{\phi_{m-1}^s\big(x, z_m(x)\big)}{K_{m-1}^s} \tag{4-13}$$

No-flow conditions are imposed at the bottom of the domain (bedrock) in the saturated zone which can be also represented in terms of stream function as:

$$\psi_M^s\big(x, z_{M+1}(x)\big) = 0 \tag{4-14}$$

To complete the problem statement, continuity of flux and pressure head must be enforced along the boundary between unsaturated and saturated zones, here referred to as the top of capillary fringe (cf):

$$\psi_m^u\big(x, z_{\mathrm{cf}}^-(x)\big) = \psi_m^s(x, z_{\mathrm{cf}}^+(x)) \tag{4-15}$$

$$\frac{\phi_m^s}{K_m^s}\Big(x, z_{\mathrm{cf}}^+(x)\Big) - z_{\mathrm{cf}}^+(x) = \varphi_m^u(x, z_{\mathrm{cf}}^-(x)) = \varphi_m^e \tag{4-16}$$

here m is the layer where top of capillary fringe is located. In each unsaturated layer ($m = 1 \dots M_u$), the general stream function solution of the following form can be developed:

$$\psi_m^u \quad (x,z) = \sum_{j=0}^{J-1} A_j^m[\sin(\omega_j x)\exp\left(\gamma_j^m z\right)] + B_j^m\,[\sin(\omega_j x)\exp\left(\bar{\gamma}_j^m z\right)] \tag{4-17}$$

Note that the form of this solution is obtained using the method of separation of variables (in a similar process to the generation of equation (3-3) as was discussed in section 3.2) and satisfies the governing equation for unsaturated flow (Equation (4-5)). In the preceding equation, j represents the coefficient index, J is the order of approximation or total number of terms in the series solution, and A_j^m, B_j^m are the series coefficients associated with the m^{th} unsaturated layer and j^{th} coefficient index. Through judicious selection of ω_j, γ_j^m and $\bar{\gamma}_j^m$ the sides no-flow conditions (Equations (4-9a) and (4-9b)) are satisfied:

$$\omega_j = \frac{j\pi}{L}; \quad \gamma_j^m = \frac{-\alpha_m}{2} + \frac{1}{2}\sqrt{{\alpha_m}^2 + \left(\frac{2j\pi}{L}\right)^2},\ \bar{\gamma}_j^m = \frac{-\alpha_m}{2} - \frac{1}{2}\sqrt{{\alpha_m}^2 + \left(\frac{2j\pi}{L}\right)^2} \tag{4-18}$$

The Kirchhoff potential series solution can be obtained using equation (4-3):

$$\begin{aligned}\phi_m^u \quad (x,z) = {} & A_0^m \exp(-\alpha_m z) \\ & - \sum_{j=1}^{J-1} \langle \frac{\gamma_j^m}{\omega_j} A_j^m[\cos(\omega_j x)\exp(\gamma_j^m z)] + \frac{\bar{\gamma}_j^m}{\omega_j} B_j^m\,[\cos(\omega_j x)\exp(\bar{\gamma}_j^m z)]\rangle\end{aligned} \tag{4-19}$$

The series solution of the saturated governing equation (Equation (4-6)) in terms of stream function is similarly obtained using the method of separation of variables while C_j^m, D_j^m are the saturated series coefficients associated with the m^{th} layer ($m = M^*, \ldots, M$).

$$\psi_m^s \quad (x,z) = \sum_{j=0}^{J-1} C_j^m[\sin(\omega_j x)\exp(\omega_j z)] + D_j^m\,[\sin(\omega_j x)\exp(-\omega_j z)]) \tag{4-20}$$

Again, through judicious selection of $\omega_j = j\pi/L$ for j = 0 ... *J-1*, the side no-flow conditions (Equations (4-10a) and (4-10b)) are satisfied. The saturated discharge potential series solution can be obtained using Cauchy-Riemann conditions (Equation (4-4)):

$$\phi_m^s \ (x,z) = C_0^m - \sum_{n=1}^{J-1} (C_j^m[\cos(\omega_j x)\exp(\omega_j z)] + D_j^m[\cos(\omega_j x)\exp(-\omega_j z)]) \quad (4\text{-}21)$$

The unknowns coefficients A_j^m, B_j^m, C_j^m and D_j^m will be calculated to satisfy the continuity and boundary conditions (Equations (4-11) to (4-18)).

4.4 Solution

The series solution for above the top of capillary fringe (i.e. the unsaturated zone) and below the top of capillary fringe (i.e. ground water and capillary fringe zones) will be determined separately by minimizing the boundary and continuity condition errors at a set of NC uniformly spaced control points located along each layer interface, the capillary fringe top, the topographic surface, and the bedrock. The location of the top of capillary fringe and water table are unknown a priori, and will be obtained through a robust iterative scheme. Initially, the top of capillary fringe is fixed to be equal to the river hydraulic head, and a Dirichlet condition of $\varphi = \varphi_m^e$ (where m is the layer where top of capillary fringe is located) is applied. The unknown coefficients for the potential within the unsaturated zone are then calculated by minimizing the boundary and continuity condition errors at a set of NC control points along each interface within the unsaturated zone (the topographic surface, top of capillary fringe, and layer interfaces), for a total of $NC\times(M_u+1)$ control points. The total weighted (w_i is the weight of each equation) sum of squared errors (TWSSE) is here subdivided into the errors along mentioned evaluation curves, i.e.,

$$TWSSE^u = WSSE_{\mathrm{t}} + \sum_{m=2}^{M_u} WSSE_{\mathrm{m}} + WSSE_{\mathrm{cf}} \quad (4\text{-}22a)$$

where

$$WSSE_{\mathrm{t}} = \sum_{i=1}^{NC} w_i[\frac{\partial \phi_1^u}{\partial \eta}(x_i, z_1(x_i)) - f(x_i)]^2 \quad (4\text{-}24b)$$

$$WSSE_{\mathrm{m}} = \sum_{i=1}^{NC} w_i\left[\psi_m^u(x_i, z_m(x_i)) - \psi_{m-1}^u(x_i, z_m(x_i))\right]^2 +$$

$$\sum_{i=1}^{NC} w_i[\varphi_m^u(x_i, z_m(x_i)) - \varphi_{m-1}^u(x_i, z_m(x_i))]^2, \text{for } m = 2, \dots, M_u \quad (4\text{-}24c)$$

$$WSSE_{\text{cf}} = \sum_{i=1}^{NC} w_i[\varphi_{\text{cf}}^u(x_i, z_{\text{cf}}^-(x_i)) - \varphi_{\text{cf}}^e]^2 \quad (4\text{-}24d)$$

the subscripts refer to the errors along the topographic surface (t), layer interfaces (m) and top of capillary fringe (cf). By minimizing equation (4-24a), approximations of the unknown unsaturated coefficients (A_j^m, B_j^m) at the first iteration will be obtained and the series solutions for stream function (4-19) and Kirchhoff potential (4-21) are fully defined. This intermediate unsaturated zone solution provides the flux or stream function distribution along the capillary fringe, which acts as the top boundary condition for the solution of the saturated zone problem (Equation 4-18). In a similar manner, the saturated unknown coefficients are calculated by minimizing the total weighted sum of squared error (TWSSE) at a set of control points along top of capillary fringe location, bottom bedrock and interfaces between saturated layers.

$$TWSSE^s = WSSE_{\text{cf}} + \sum_{m=M^*+1}^{M} WSSE_{\text{m}} + WSSE_{\text{b}} \quad (4\text{-}23a)$$

where

$$WSSE_{\text{cf}} = \sum_{i=1}^{NC} w_i \left[\psi_m^s\left(x_i, z_{\text{cf}}^+(x_i)\right) - \psi_m^u\left(x_i, z_{\text{cf}}^-(x_i)\right)\right]^2 \quad (4\text{-}25b)$$

and m is the layer where top of capillary fringe is located

$$WSSE_{\text{m}} = \sum_{i=1}^{NC} w_i\left[\psi_m^s(x_i, z_m(x_i)) - \psi_{m-1}^s(x_i, z_m(x_i))\right]^2 + \sum_{i=1}^{NC} w_i\left[\frac{\phi_m^s}{K_m^s}(x_i, z_m(x_i)) - \frac{\phi_{m-1}^s}{K_{m-1}^s}(x_i, z_m(x_i))\right]^2 \quad (4\text{-}25c)$$

$$WSSE_{\text{b}} = \sum_{i=1}^{NC} w_i\left[\frac{\partial \phi_{M+1}^s}{\partial \eta}(x_i, z_{M+1}(x_i))\right]^2 \quad (4\text{-}25d)$$

By minimizing equation (4-25a), an approximation of the unknown saturated coefficients (C_j^m,D_j^m) is obtained and the series solution in terms of stream function (4-22) and discharge potential (4-23) are fully defined. The saturated series solution provides a water pressure distribution along the approximate top of capillary fringe surface at each control point ($\varphi_{cf}(x_i)$). In each iteration, this may be used to modify the location of the top of capillary fringe according to:

$$z_{cf}^{k+1}(x_i) = z_{cf}^{k}(x_i) + \tau(\varphi_{cf}^{k}(x_i) - \varphi_m^e) \quad (4\text{-}24)$$

where k is the iteration number, φ_m^e is the air entry pressure head of the m^{th} layer (m is the layer where the top of capillary fringe is located), and τ is a relaxation factor which is between 0 and 1. The top of capillary fringe location is therefore revised and this iteration scheme will be continued until the saturated pressure head at each control points along top of capillary fringe $\varphi_{cf}^{k}(x_i)$ converges to air entry pressure. After the location of the top of capillary fringe converges to a fixed position, the water table elevation is obtained as the contour with zero pressure head. Note that solution of the over determined system of equations is handled using the LSCOV function of MATLAB.

4.5 Analysis

The following section describes a set of tests used to demonstrate the quality and the convergence behavior of the series solutions. The efficiency of the approach is assessed for geometrically complex homogenous and stratified unconfined aquifers under different surface boundary conditions. Normalized continuity and boundary condition errors (Equations 4-27) are assessed along each interface (m) at points located between the control points used within the least squares solution:

$$\varepsilon_m^{\text{flux}}(x_i) = \frac{\left|\frac{\partial\phi^-}{\partial\eta}(x_i) - \frac{\partial\phi^+}{\partial\eta}(x_i)\right|}{\max(f(x)) - \min(f(x))} \text{ for } m = 1,\ldots, M+1 \quad (4\text{-}25a)$$

$$\varepsilon_m^{\text{head}}(x_i) = \frac{\left|\varphi_{(x_i)}^- - \varphi_{(x_i)}^+\right|}{\max(\varphi) - \min(\varphi)} \text{ for } m = 2,\ldots, M \quad (4\text{-}27b)$$

Note that for the topographic surface ($m = 1$), $\varepsilon_1^{\text{flux}}(x_i)$ is

$$\varepsilon_1^{\text{flux}}(x_i) = \frac{\left|f(x_i) - \frac{\partial\phi^+}{\partial\eta}(x_i)\right|}{\max(f(x)) - \min(f(x))} \quad (4\text{-}27c)$$

and for the bottom bedrock ($m = M + 1$):

$$\varepsilon_{M+1}^{\text{flux}}(x_i) = \frac{\left|\frac{\partial\phi^-}{\partial\eta}(x_i)\right|}{\max(f(x)) - \min(f(x))} \quad (4\text{-}27d)$$

$\min(f(x))$ and $\max(f(x))$ [LT^{-1}] refer to minimum and maximum flux applied across the topographic surface, $\max(\varphi)$ and $\min(\varphi)$[L] are the maximum and minimum value of the pressure head in the entire domain. In addition, with a manner similar to [*Tristscher et al.*, 2001] total root

mean square normalized flux error ($\text{rmse}^{\text{flux}}$) and total root mean square normalized head error ($\text{rmse}^{\text{head}}$) are obtain as follows;

$$\text{rmse}^{\text{flux}} = \frac{1}{\sqrt{NC}}\text{sqrt}[\sum_{i=1}^{NC}(\varepsilon_1^{\text{flux}}(x_i))^2 + \sum_{i=1}^{NC}(\varepsilon_{M+1}^{\text{flux}}(x_i))^2 + \sum_{i=1}^{NC}(\varepsilon_m^{\text{flux}}(x_i))^2] \quad (4\text{-}26a)$$

$$\text{rmse}^{\text{head}} = \frac{1}{\sqrt{NC}}\text{sqrt}[\sum_{i=1}^{NC}(\varepsilon_m^{\text{head}}(x_i))^2] \text{ for } m = 2,\ldots, M \quad (4\text{-}28b)$$

The rate of convergence of the solutions with a free boundary condition will also be assessed in the below cases.

4.5.1 Example 1: Homogenous system

The configuration for a hypothetical homogenous unconfined aquifer system adjacent to a 20 m wide river is shown in Figure 4-2. Figure 4-2a shows the infiltration and evapotranspiration function ($f(x)$) applied across the topographic surface. The hydrological and hydrogeological parameters used in example 1 are: $K^s = 1$ m d^{-1}, $\alpha_1 = 0.5$ m^{-1}, $\varphi^e = -0.5$ m, river head (H_r) = 5.5 m, river width = 20m.

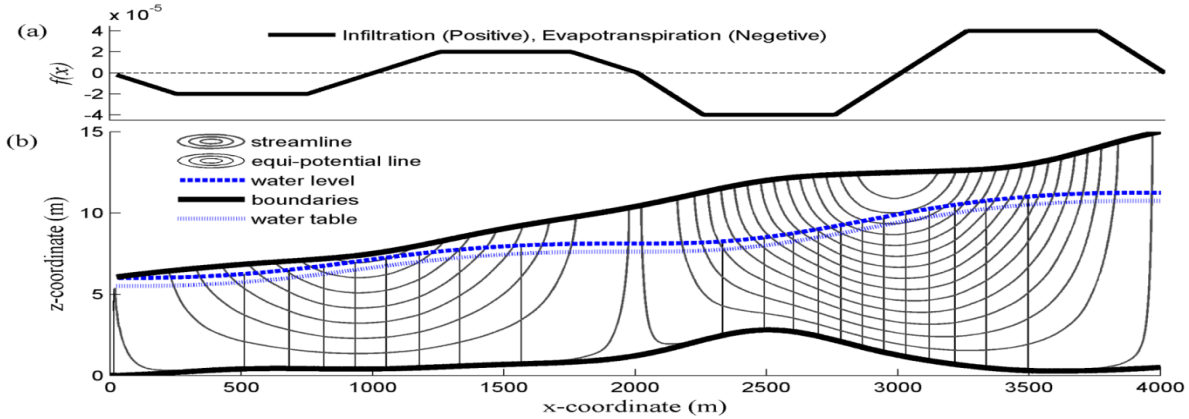

Figure 4-2. a) Infiltration and evapotranspiration function $f(x)$ [md^{-1}] used in example 1, b) Layout of the flow streamlines (grey), equi-potential contours (black), water level and water table in a homogenous unconfined aquifer adjacent to a constant head river at left corner after 10 iterations. Image from *Ameli et al.* [2013].

The flow net for this problem, along with the calculated top of capillary fringe and water table locations are shown in Figure 4-2b. This solution was identified after 10 iterations. Hydraulic head contours in the saturated zone show that conditions are nearly hydrostatic beneath the top of capillary fringe interface. Above the capillary fringe the flow condition is not hydrostatic (not shown here). The solution was obtained using $(M_u + M_s)(2N+1)$ =282 coefficients and 1400 control points along each evaluation curve (i.e., the topographic surface, bedrock and top of capillary fringe). The topographic surface boundary condition (Eq. (4-11b)), no-flow bedrock boundary condition (Eq. (4-16)) and continuity of flux (Equation (4-17)) and head (Equation (4-18)) across top of capillary fringe, have been satisfied by expanding the general series solution (Equations (4-19), (4-21), (4-22) and (4-23)) at control points along each interface and minimizing error using weighted least square method (Equations (4-24) and (4-25)). Note that since the units and magnitude of the flux and head errors are different, weighting coefficients for each control point (w_i) were considered as 4 and 1 for flux and head conditions respectively. A relaxation factor τ = 0.5 used to control the convergence behaviour of the top of the capillary fringe (Equation 4-26).

Figure 4-3 demonstrates the quality and the convergence behavior of the series solutions used in example 1. Figure 4-3a shows the convergence of the solution as the pressure head at 1400 control points along the free boundary top of capillary fringe converges to air entry pressure ($\varphi^e = -0.5\ m$). As can be seen from the figure, control points along the intersection of the top of capillary fringe and topographic surface have the largest absolute error at initial iterations. Figure 4-3b shows the normalized flux errors across the topographic surface ($\varepsilon_1^{\text{flux}}$) and the bottom bedrock ($\varepsilon_{M+1}^{\text{flux}}$) at 1400 points between the control points used for least squares minimization.

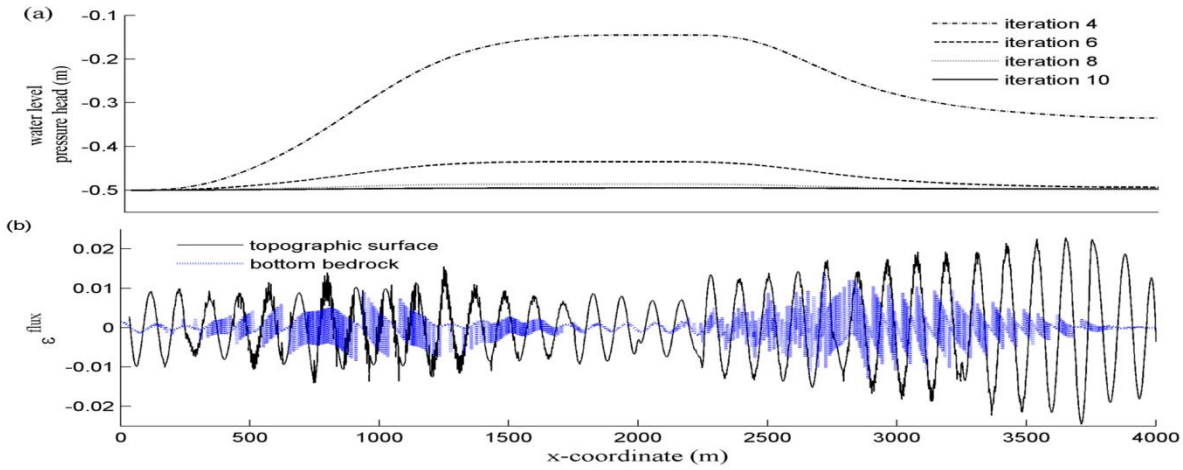

Figure 4-3. Convergence of the water level moving boundary between saturated and unsaturated zones to air entry pressure ($\varphi^e = -0.5$ m) with relaxation factor (τ) = 0.5, b) Normalized flux error across boundary interfaces (topography surface and the bottom bedrock). Image from *Ameli et al.* [2013].

Although there is a flux error across the impermeable bedrock, the net normalized flux error is on the order 10^{-17} , which guarantees mass conservation inside the domain. The largest normalized flux error over both interfaces (2%) occurs along the intersection of the top of capillary fringe and the topographic surface, and on the right side of the topographic surface with higher $f(x_i)$ (Figure 4-3b). The error along the topographic surface can result from abrupt changes of surface function (evapotranspiration to infiltration and vice versa) that cause Gibbs phenomenon. Although a linear transition was used between infiltration and evapotranspiration (Figure 4-2a), some degree of function smoothing could have reduced this error. Normalized head errors along the river boundary condition are also on the order 10^{-8} (not shown here). In addition, total root mean square normalized flux error ($\mathrm{rmse}^{\mathrm{flux}}$) along the topographic surface and bottom bedrock are on the order of 10^{-3}. Note that, since the governing equation is elliptic and satisfied exactly using series solutions method, the largest errors in the domain occur along the system boundaries. The series solution is seen to be valid and successful (with acceptable ranges of error along boundaries) in naturally complex homogenous regional unconfined aquifer as long as Gibbs phenomenon is avoided and the Fourier series converges.

4.5.2 Example 2: Heterogeneous system

In a second example, a hypothetical regional aquifer system with 4 layers is considered. The 5m wide river with constant head equal to 10 m is located at the left of the domain. Two different surface flux distributions ($f(x)$) are considered in example 2 to assess the impact of the surface water boundary upon the efficiency of the approach (Figure 4-4). The hydrological and hydro-geological parameters used are : $K_1^S = 10\ \mathrm{m\ d^{-1}}$, $K_2^S = 8\ \mathrm{m\ d^{-1}}, K_3^S = 0.8\ \mathrm{m\ d^{-1}}, K_4^S = 0.08\ \mathrm{m\ d^{-1}}, \alpha = 0.5\ \mathrm{m^{-1}}$ (identical for 4 layers), $\varphi^e = -0.5$ m (identical for 4 layers), river head, h_r = 5 m, river width = 10m.The sorptive number (α) and air entry pressure (φ^e) are assumed to be identical for all layers. This assumption guarantees that the continuity of head condition across the layer interfaces in the unsaturated zone (Equation (4-13)) can be expressed as a linear equation with respect to the unknown solution coefficients.

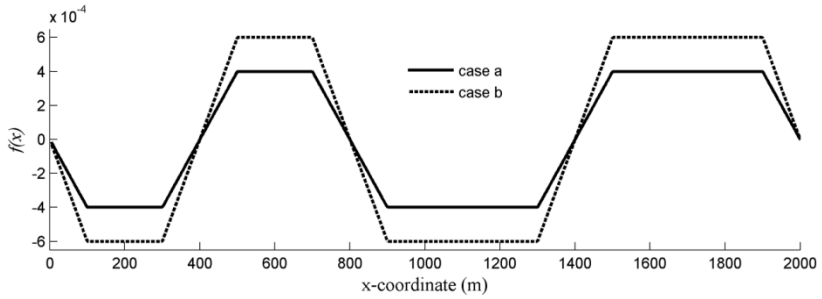

Figure 4-4. Infiltration and evapotranspiration function ($f(x)$) [md^{-1}] used in example 2, for cases a and b. Image from *Ameli et al.* [2013].

Figure 4-5 shows the layout of flow net for the two cases. As can be seen, while *M* is equal to 4 in both cases, M_u and M_s are 2 in case a and for case b due to the intersection of the top of capillary fringe with the first layer interface M_u is 2 and M_s is 3. Figure 4-5b, in addition, demonstrates as infiltration rate increases at *x*=1400 m, the top of capillary fringe elevation increases and intersects the layer interface.

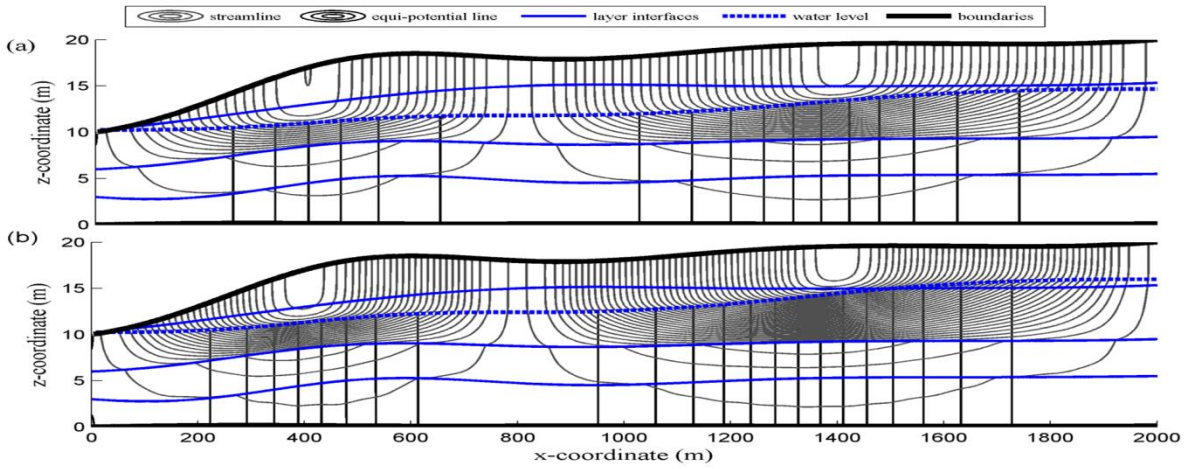

Figure 4-5. Layout of flow net in the 4-Layer aquifer after 14 iterations, a) case (a), b) case (b). Image from *Ameli et al.* [2013].

Note that M^* (the uppermost layer in which the top of capillary fringe is located) is the second and first layer for case a and b, respectively. The solutions were obtained using $(2N+1) = 101$ coefficients in each layer ($(M_u + M_s)$ $(2N+1)$ coefficients in total, 404 for case (a) and 505 for case (b), and 1200 control points along each evaluation curve.

Similar to example 1, for test case a each control point weighting coefficients (w_i) has been considered as 4 and 1 for flux and head boundaries respectively and the relaxation factor (τ) equal to 0.5 used for the top of capillary fringe pressure head convergence (Equation (4-26)). For case b, on the other hand, a smaller relaxation factor (τ) = 0.375 was required to handle complications due to the intersection of the top of capillary fringe and the layer interface. Figure 4-6 shows the rapid convergence of the solution for cases a and b while the pressure head at 1200 control points along the top of capillary fringe free boundary converges to the air entry pressure ($\varphi^e = -0.5\ m$).

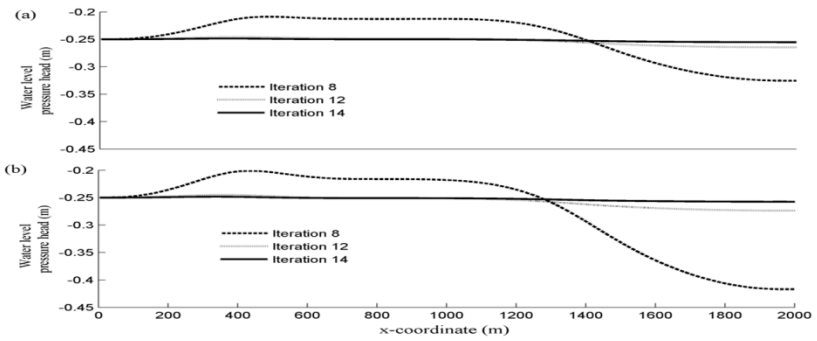

Figure 4-6. Convergence of the water level moving boundary between saturated and unsaturated zones in example 2; a) case (a) with relaxation factor (τ) = 0.5 , b) case (b) with relaxation factor (τ) = 0.375. Image from *Ameli et al.* [2013].

The steepness of the capillary fringe surface around the intersection combined with the change in material properties along this free boundary interface may cause Gibbs phenomenon in case b); this describes the slower convergence rate of the control points around the intersection Figure 4-7 shows the normalized flux errors across the top $\varepsilon_1^{\text{flux}}$ and the bottom $\varepsilon_{M+1}^{\text{flux}}$ boundary conditions, and along the layer interfaces $\varepsilon_m^{\text{flux}}$ at 1200 points for both cases. The maximum normalized flux errors across all the interfaces are on the order of 10^{-2} (m d^{-1}). For both cases, the maximum normalized flux error along the topographic surface (2%) occurs at sharp changes in surface function $f(x)$ (Figure 4-4). A high contrast in hydraulic conductivity ($K_s^2/K_s^3 = 10$) across 2nd interface z_3 (the interface between the second layer and the third one), could cause normalized flux error as high as 2% for both cases. Intersection of the top of capillary fringe with the first layer interface (z_2) caused an abrupt change in the governing equation from the unsaturated into the saturated along this interface. Consequently, normalized continuity flux errors across the first layer interface (z_2) in case b are higher than in case a around the intersection with a maximum error of 3% at x=1500 m (the intersection point circle in Figure 4-7b). Normalized flux error trend across this interface for case b are almost identical to case a for points far away from the intersection. In addition, for both cases a and b total root mean square normalized flux error ($\text{rmse}^{\text{flux}}$) are on the order of 10^{-3} , with the largest contribution to this error found along the topographic surface.

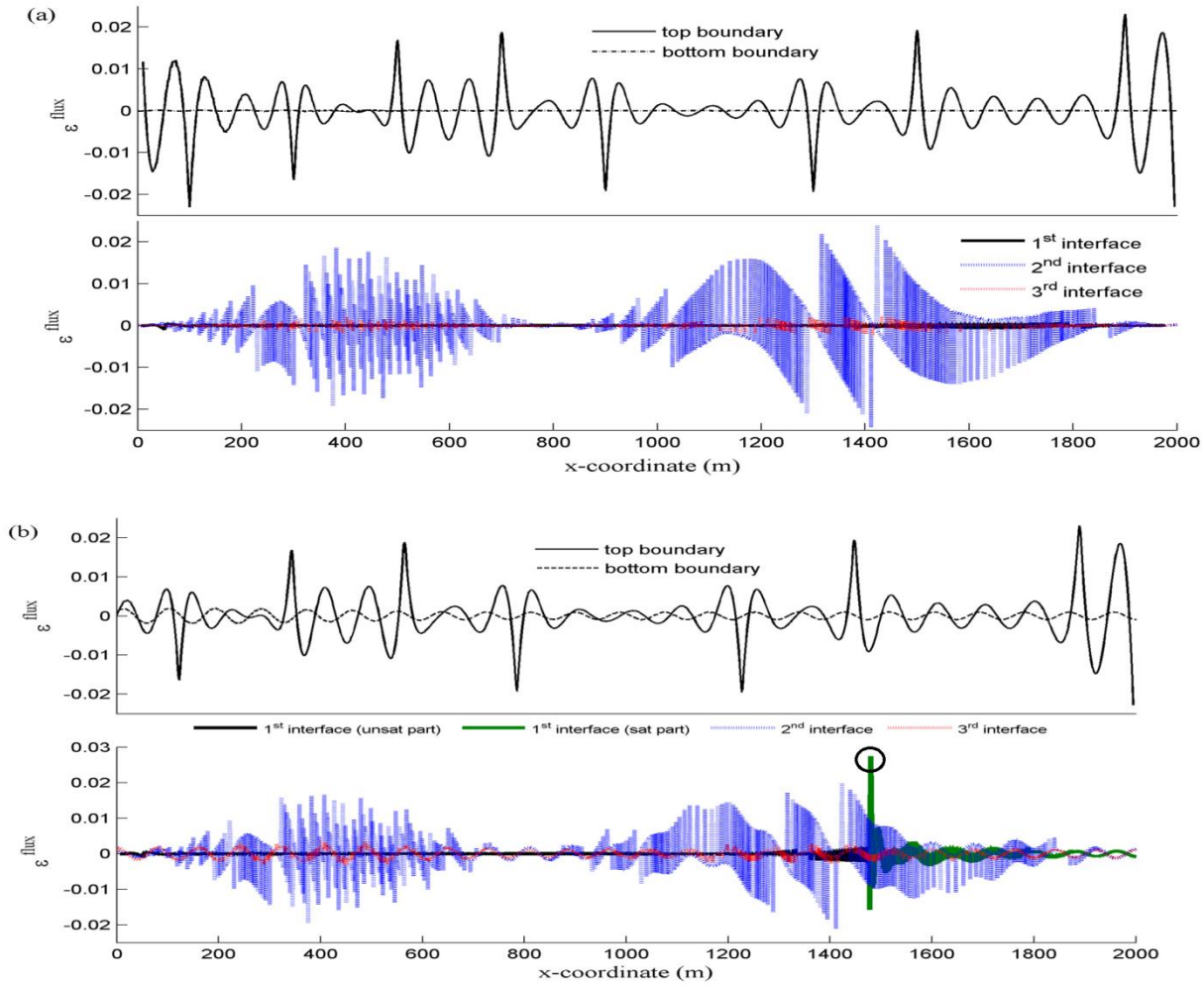

Figure 4-7. Normalized flux boundary and continuity error across internal interfaces (1200 points) after 14 iterations in the example 2; a) case (a), b) case (b) the unsaturated and saturated part of the first layer interface (z_2) have shown in separate colours (black and green respectively) and black circle shows the maximum error along (z_2). Image from *Ameli et al.* [2013].

The errors in flux are within acceptable range, although the previous series solutions of [*Tristscher et al.*, 2001; *Wong and Craig*, 2010] reported lower flux errors. This may be attributed to the discontinuities in the gradient of the infiltration distribution function, the complexity of the stratified domain geometry, or the complexity of the free boundary problem, any of which can exacerbate Gibbs phenomenon. However, the net normalized flux error across layer interfaces and bottom bedrock are on the order of 10^{-18} to 10^{-14} for both cases except for the first layer interface in case b with errors on the order of 10^{-7} (due to intersection of the top of capillary fringe with the first layer

interface). Figure 4-8 illustrates the normalized head errors $\varepsilon_m^{\text{head}}$ across the layer interfaces at 1200 points for both cases. Similar to the flux errors across the layer interfaces, for case (b) the maximum normalized head errors across the first layer interface occur at the intersection of the top of capillary fringe and this interface that is in a magnitude of 10^{-5} (m). For both cases, a high contrast in hydraulic conductivity ($8/0.8$) across 2nd interface (z_3) could cause the highest normalized head errors over the entire domain. In addition, for both cases a and b total root mean square normalized head error ($\text{rmse}^{\text{head}}$) are on the order of 10^{-7}.

In spite of the efficiency of the developed models in this chapter, the sorptive numbers were not consistent with the highly permeable soils used here. For a larger (more realistic) sorptive value the model did not converge; this may be attributed to the instability of continuity of head equation (Equation 4-13) across the layer interfaces.

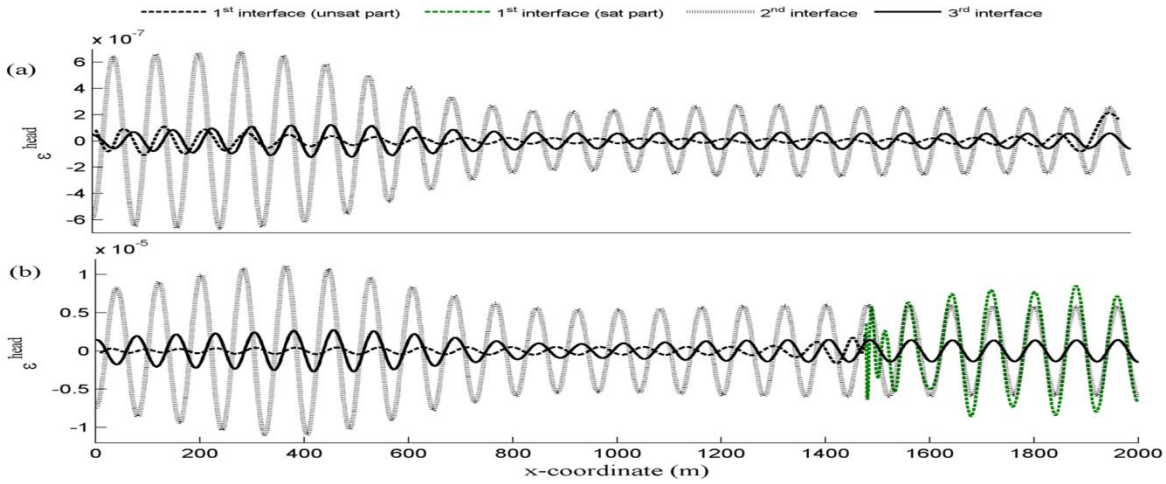

Figure 4-8. Normalized head continuity error across internal interfaces in the example 2, a) case a, b) case b the unsaturated and saturated part of the first layer interface (z_2) have shown in separate colours (black and green respectively). Image from *Ameli et al.* [2013].

4.6 Conclusion

In this chapter, robust general solutions for free boundary steady saturated-unsaturated flow in naturally complex heterogeneous geological settings have been developed and assessed. The capillary fringe zone has been considered as a distinctive zone with a free boundary at the top and bottom.

Semi-analytical series solutions have been showed to simulate coupled saturated and unsaturated flow accurately as long as Gibbs phenomenon issue has been addressed and the Fourier series converges. This is contingent upon

- The continuity conditions being linear (e.g., identical sorptive number and air entry pressure head for all unsaturated layers)
- interfaces being continuous in value and gradient
- the surface function ($f(x)$) being continuous in value and ideally gradient

The solutions converged with acceptable rates of convergence and errors in top of capillary fringe and water table locations. Without discretization artifacts, introduced by numerical schemes, boundary errors, pressure head, flux and stream function distributions are immediately available as continuous function of the space. The number of degrees of freedom required to simulate these complex systems is small.

Chapter 5
Semi-analytical series solutions for three dimensional groundwater-surface water interaction

This chapter is based on the following published article. For the coherence of this thesis, changes have been made in the introduction, background, method and conclusion sections of this publication. References are presented at the end of the thesis.

Ameli, A. A., J. R. Craig, Semi-analytical series solutions for three dimensional groundwater-surface water interaction *Water Resour. Res., 50,* Doi:10.1002/2014WR0.

5.1 Introduction

This chapter addresses the extension of the semi-analytical series solutions approach to free boundary 3-D steady subsurface flow controlled by water exchange across the ground surface (e.g., evapotranspiration, infiltration, seepage faces) and the presence of surface water bodies in a stratified aquifer. A priori unknown water table surface including seepage faces and recharge zones, is determined semi-analytically using a robust iterative scheme. The solutions are derived and demonstrated on a number of test cases and the errors are assessed and discussed. This accurate and grid-free 3-D model can be a helpful tool for providing insight into lake-aquifer and stream-aquifer interactions. Here, it is used to assess the impact of lake sediment geometry and properties on lake-aquifer interactions. Various combinations of lake sediment are considered and the appropriateness of the Dupuit-Forchheimer approximation for simulating lake bottom flux distribution is investigated. In addition, the method is applied to a test problem of surface seepage flows from a complex topographic surface.

5.2 Background

Semi-analytical series solutions have been used to address 2-D saturated topography-driven flow [e.g., *Craig*, 2008; *Wong and Craig*, 2010] and saturated-unsaturated free boundary flow [*Ameli et al.*, 2013; *Tristscher et al.*, 2001] in naturally complex homogenous and stratified unconfined aquifers. This method is able to provide helpful insights into effective controls on groundwater-surface water interaction including the effect of sediment geometry and material property on seepage distributions at the lake-aquifer interface, all without the use of grid or mesh.

The relative significance of lake size, confined aquifer size, homogenous confined aquifer material property and precipitation amount in lake-aquifer flow regime have been assessed numerically [*Genereux and Bandopadhyay*, 2001; *Townley and Trefry*, 2000] and analytically [*Kacimov*, 2000; 2007]. However, the effect of lake sediment material properties and geometry on lake-aquifer interaction has not been fully investigated. It is known that lake sediment may play a significant role in altering the lake bed shape [*Miller et al.*, 2013] and will impact the distribution of seepage flux at the lake bed [*Genereux and Bandopadhyay*, 2001]. However, the impact of sediment layer geometry and properties on seepage flux at the lake bed have not been assessed.

In 2-D Dupuit-Forchheimer models [*Kirkham*, 1967], where the resistance to vertical flow is ignored, it is common to treat the lake bed as uniform, which leads to a characteristic seepage distribution where lake's fluxes are highest at the shore and decrease with distance from the shoreline. With Dupuit-Forchheimer assumption, the extent of this seepage zone as measured from the lake shore is proportional to a leakage factor, calculated from the sediment and aquifer conductivity and thickness [e.g., *Bakker*, 2002; *Bakker*, 2004; *Strack*, 1984]. Multiple research studies have shown that the Dupuit-Forchheimer model may be a reasonable approximation of a fully 3-D system when the lake is very large compared to the aquifer thickness [e.g., *Hunt et al.*, 2003b; *Kacimov*, 2000]. Some 3-D and 2-D cross sectional models have been used to estimate sediment layer impacts using this leakage factor approach instead of explicitly modeling the lake sediment layer [*Kacimov*, 2000; *Nield et al.*, 1994]. However, the leakage factor approach neglects horizontal flow through the lake sediment and may therefore miss lateral flow effects, and it can be accurate only for the case of a very thin and low permeable lake sediment with uniform thickness [*Kacimov*, 2000]. To realistically investigate the effect of lake sediment on lake-aquifer interaction, a robust 3-D multi-layer model with the ability to explicitly consider the sediment layer is desirable. In one of the few research studies that independently considered the lake sediment layer, Genereux and Bandopadhyay [2001] have treated the sediment as porous medium cells (of lower hydraulic conductivity) in direct contact with the lake bed. Their study did not consider the geometry of the lake sediment layer (a uniform sediment layer with a specified thickness equal to the discretized mesh thickness was used) and suffered from numerical discretization errors [*Bakker and Anderson*, 2002].

5.3 Problem statement

The layout of a stratified 3-D aquifer system with a free water table surface and surface water bodies is shown in Figure 5-1. The domain has a length of L_x and L_y in *x* and *y* direction, and is subdivided into *M* layers with arbitrary interface geometry, each with hydraulic conductivity of K_m. Layers, indexed downward from *m* =1 to *m* =*M*, are bounded by the surface $z_m(x,y)$ above and $z_{m+1}(x,y)$ below, and may pinch out to a thickness of zero. The bottom bedrock $z_{M+1}(x,y)$ and sides of the aquifer are impermeable. The free boundary (a priori unknown) water table surface, $z_{wt}(x,y)$, is defined as the surface with zero pressure head. The land surface is defined by $z_1(x,y)$. The modeled domain is bounded above by $z_t(x,y)$, which is the surface defined as the water table surface $(z_{wt}(x,y))$ where the water table is lower than the land surface, and the land surface $(z_1(x,y))$ at seepage faces or areas in direct contact with surface water. All layer interfaces, the topographic surface, and the bedrock surface are specified prior to solution.

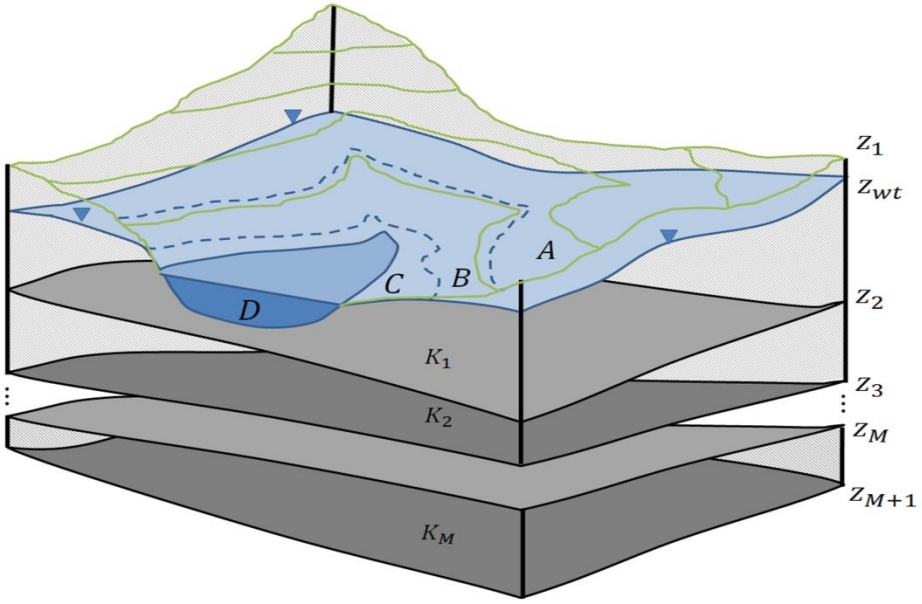

Figure 5-1. Layout of the general 3-D problem. *M* layers are separated by the interfaces $z_m(x,y)$, with $z_{M+1}(x,y)$ corresponding to the bottom bedrock and $z_1(x,y)$ corresponding to the land surface. $z_{wt}(x,y)$ corresponding to the water table location. A, B, C, D refers to the zones where different types of surface conditions are applied: (A) uncorrected infiltration, (B) transition between recharge and discharge zones, (C) seepage face and (D) surface water. Image from *Ameli and Craig* [2014].

As described in chapter 3, the problem may be posed in terms of a discharge potential, ϕ_m [L^2T^{-1}], defined as

$$\phi_m(x,y,z) = K_m\, h_m(x,y,z) \tag{5-1}$$

where $h_m(x,y,z)$ [L] is the total hydraulic head in the m^{th} layer. Using continuity of mass and Darcy's law, each layer's discharge potential function must satisfy the Laplace equation:

$$\frac{\partial^2 \phi_m}{\partial x^2} + \frac{\partial^2 \phi_m}{\partial y^2} + \frac{\partial^2 \phi_m}{\partial z^2} = 0 \quad \text{for } m = 1, \dots, M \tag{5-2}$$

Flow rates are calculated as the spatial derivative of the discharge potential. In a manner similar to *Wong and Craig* [2010] for the 2-D discharge magnitude normal to an interface, the 3-D discharge across an interface can be decomposed into vertical and horizontal components when the cosine of the slope angle (in both *x* and *y* directions) describing each evaluation surface may be approximated as unity. The resulting equation is as follows:

$$\frac{\partial \phi_m}{\partial \eta} = \frac{\partial \phi_m}{\partial z} - \frac{d\hat{z}}{dx}\frac{\partial \phi_m}{\partial x} - \frac{d\hat{z}}{dy}\frac{\partial \phi_m}{\partial y} \tag{5-3}$$

where η is the coordinate normal to interface surfaces represented by the function $\hat{z}(x,y)$, which is either a layer interface ($z_m(x,y)$), bottom bedrock surface ($z_{M+1}(x,y)$) or top interface ($z_t(x,y)$).

Across the sides of the domain, no-flow conditions in *x* and *y* directions are imposed.

$$\frac{\partial \phi_m}{\partial x}(0,y,z\ \ ) = \frac{\partial \phi_m}{\partial x}(L_x,y,z\ \ ) = 0 \text{ for } m = 1, \dots, M \tag{5-4a}$$

$$\frac{\partial \phi_m}{\partial y}(x,0,z\ \ ) = \frac{\partial \phi_m}{\partial y}\big(x,L_y,z\ \ \big) = 0 \text{ for } m = 1, \dots, M \tag{5-4b}$$

The top surface boundary of the modeled domain, $z_t(x,y)$, is subject to a specified vertical flux distribution (recharge), and/or Dirichlet boundary conditions along surface water bodies and seepage faces. Here, in order to insure convergence of the iterative approach, both Dirichlet and Neumann conditions along the a priori unknown top surface are treated as being dependent upon the depth of the water table. Here we extend the approach of *Forsyth* [1988], where Dirichlet seepage faces and specified head boundary conditions are implemented as equivalent source/sink terms, to handle the

spatially variable boundary condition along the water table surface. In regions where the water table is below the surface, the specified recharge rate is applied directly. A specified depth (δ) with a reduced recharge rate (transition zone), is considered between recharge and discharge zones that may be justified by the increased evapotranspiration in the vicinity of the land surface. Rather than treating this flux-water table elevation relationship as piecewise linear (as might be done in e.g., MODFLOW), a smooth continuous relationship, displayed in Figure 5-2, is used. This ensures smooth transitions between regimes and better numerical convergence of the water table while still respecting the physics of the problem. The function is defined as

$$F(z_{wt}) = \begin{cases} R & z_{wt} < (z_1 + d_{sw}) - \delta \\ R(1 - e^{\alpha[z_{wt} - (z_1 + d_{sw})]}) & z_{wt} > (z_1 + d_{sw}) - \delta \end{cases} \quad (5\text{-}5)$$

Where R [LT^{-1}] is the specified surface infiltration rate, $d_{sw}(x, y)$ is the surface water body depth [L], defined from the bottom of the surface water body, which is zero along $z_t(x, y)$ except at the area in direct contact with surface water body (e.g., lake and stream). The exponential function parameter, α [L^{-1}], controls the numerical convergence of the scheme. A small value of α ensures a smooth transition between regimes and guarantees the stability of the solution with a potentially slow convergence rate in emulating the Dirichlet condition. On the other hand, a large value of α increases rate of convergence; however, by attenuating the transition zone this may cause instabilities attributed to Gibbs phenomenon. Gibbs phenomenon is a common issue with series-based solution, and occurs whenever an orthogonal series (e.g., a Fourier series) is used to approximate a discontinuous function [for further details see *Nahin*, 2011]. In the remainder of this paper a value of transition zone depth (δ=10 cm) was selected to avoid sharp transition between recharge and discharge zones. In addition, the selected α value for each case should be sufficiently high to mimic a Dirichlet condition but not so high to cause numerical instability.

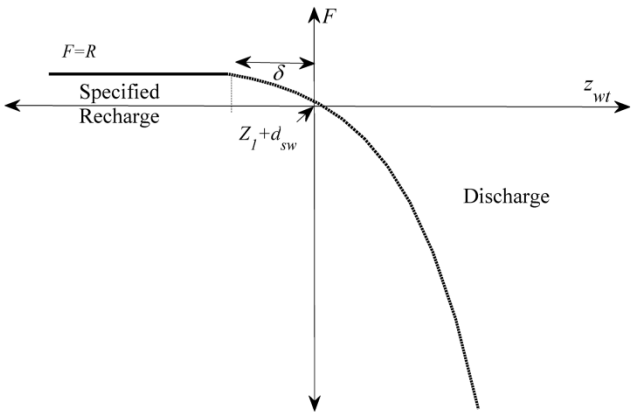

Figure 5-2. The method to obtain flux $\boldsymbol{F(z_{wt})}$ along the top surface boundary. Image from *Ameli and Craig* [2014].

As outlined in *Forsyth* [1988] such an approach efficiently discharges a sufficient amount of water to force the Dirichlet condition in areas where the estimated water table elevation is above the land surface. This treatment of the top boundary with a continuous transition from recharge to discharge (Dirichlet) conditions ensures that: 1- The locations of seepage faces, do not have to be known a priori, 2- sharp transitions between regimes do not produce corresponding transitions in conditions (potentially leading to Gibbs phenomenon) and 3- the algorithm for determining the water table location is not predisposed to keep portions of the water table in a fixed state. Such an algorithm may be useful for numerical integrated models (e.g., HydroGeoSphere), as well.

The calculated flux from Equation (5-5) is applied along the top surface of the modeled domain, $z_t(x,y)$,

$$\frac{\partial \phi}{\partial \eta}\big(x,y,z_t(x,y)\big) = F(x,y) \tag{5-6}$$

The continuity of flux and pressure head along each layer interface ($m = 2,\dots,M$) can be represented as:

$$\frac{\partial \phi_m}{\partial \eta}\big(x,y,z_m(x,y)\big) = \frac{\partial \phi_{m-1}}{\partial \eta}\big(x,y,z_m(x,y)\big) \tag{5-7}$$

$$\frac{\phi_m\left(x,y,z_m(x,y)\right)}{K_m} = \frac{\phi_{m-1}\left(x,y,z_m(x,y)\right)}{K_{m-1}} \tag{5-8}$$

Lastly, no-flow conditions are imposed along the bottom of the domain (bedrock)

$$\frac{\partial \phi_M}{\partial \eta}\left(x,y,z_{M+1}(x,y)\right) = 0 \tag{5-9}$$

In each layer ($m = 1 \ldots M$), a discharge potential function of the following form is assumed:

$$\phi_m(x,y,z) = \sum_{j=0}^{J-1}\sum_{n=0}^{N-1} cos\,\omega_j x\, cos\,\omega_n y\,[A_{jn}^m cosh(\gamma_{jn} z) + B_{jn}^m sinh(\gamma_{jn} z)] \tag{5-10}$$

Note that the form of this solution is obtained using the method of separation of variables and satisfies the governing equation (Equation (5-2)) as described in section 3.2. In the preceding equation, j and n represent the coefficient index while J and N are the order of approximation in the x and y direction respectively (in total, N x J series terms are used). The series coefficients associated with the m^{th} layer are A_{jn}^m, B_{jn}^m. Through judicious selection of ω_j, ω_n and γ_{jn}, the sides no-flow conditions (Equation (5-4) are satisfied:

$$\omega_j = \frac{j\pi}{L_x};\ \omega_n = \frac{n\pi}{L_y};\quad \gamma_{jn} = \pi\sqrt{\frac{j^2}{{L_x}^2} + \frac{n^2}{{L_y}^2}} \quad \text{for} \quad j = 0 \ldots . J-1 \ \ \&\ n = 0 \ldots . N-1 \tag{5-11}$$

The unknown coefficients A_{jn}^m, B_{jn}^m will be calculated to satisfy the continuity and boundary conditions (Equations (5-6) to (5-9)).

5.4 Solution

To fully define 3-D series solutions, unknown coefficients are calculated using a constrained least squares numerical algorithm. A priori unknown water table elevation is obtained through a robust iterative scheme. Initially it is guessed to be equal to a specified elevation $z_{wt}^r(x,y)$ where r refers to iteration number; r =1 for the initial iteration. The relative location of the water table to (z_1+d_{sw}) at a regular grid of NC control points along $z_t^r(x,y)$, determines the flux distribution $F^r(x,y)$ from Equation (5-5). A set of NC control points, in addition, are located along each layer interface and bedrock surface to apply the continuity of flux (Equation (5-7)) and head (Equation (5-8)), and no-

flow boundary condition along the bedrock (Equation (5-9)). Note that here *NC* is the product of NC_x and NC_y which are the number of uniformly spaced control points in *x* and *y* direction respectively. For each guess of the water table surface, the unknown coefficients are calculated by minimizing the total sum of squared boundary and continuity condition errors (at control points along the mentioned interfaces) that is constrained such that zero net flux is maintained along the top boundary ($z_t^r(x,y)$). The total sum of squared errors (TSSE) is here subdivided into the errors along mentioned evaluation curves, i.e.,

$$TSSE \quad = SSE_{\mathrm{t}} + \sum_{m=2}^{M} SSE_{\mathrm{m}} + SSE_{\mathrm{b}} \tag{5-12a}$$

where

$$SSE_{\mathrm{t}} = \sum_{i=1}^{NC_x} \sum_{k=1}^{NC_y} [\frac{\partial \phi}{\partial \eta}\left(x_i, y_k, z_t^r(x_i, y_k)\right) - F^r(x_i, y_k)]^2 \tag{5-12b}$$

$$SSE_{\mathrm{m}} =$$

$$\sum_{i=1}^{NC_x} \sum_{k=1}^{NC_y} [\frac{\partial \phi_m}{\partial \eta}\left(x_i, y_k, z_m(x_i, y_k)\right) - \frac{\partial \phi_{m-1}}{\partial \eta}\left(x_i, y_k, z_m(x_i, y_k)\right)]^2 +$$

$$\sum_{i=1}^{NC_x} \sum_{k=1}^{NC_y} \left[\frac{\phi_m(x_i, y_k, z_m(x_i, y_k))}{K_m} - \frac{\phi_{m-1}(x_i, y_k, z_m(x_i, y_k))}{K_{m-1}}\right]^2 \text{ for } m=2, \ldots, M \tag{5-12c}$$

$$SSE_{\mathrm{b}} = \sum_{i=1}^{NC_x} \sum_{k=1}^{NC_y} [\frac{\partial \phi_M}{\partial \eta}\left(x_i, y_k, z_{M+1}(x_i, y_k)\right)]^2 \tag{5-12d}$$

with zero net flux constraint along $z_t^r(x,y)$ as follows;

$$\sum_{i=1}^{NC_x} \sum_{k=1}^{NC_y} [F^r(x_i, y_k)] \; = 0 \tag{5-13a}$$

The subscripts refer to the errors along the top surface (t), layer interfaces (m) and bottom bedrock (b). Note that Equation (5-13a) is implemented while $F^r(x,y)$ is obtained from equation 5. However, to apply the zero net flux constraint along with least squares system of equations, a zero pressure head condition along the water table is used ($z_{wt}^r \rightarrow h_m^r$) for the control points where $z_{wt} > \delta$ and $F^r(x_i, y_k)$ is obtained as follows:

$$F^r(x_i,y_k)=\begin{cases} R\,(x_i,y_k) & z_{wt} < (z_1+d_{sw})-\delta \\ -W(z^r_{wt}(x_i,y_k))\,[h^r_m(x_i,y_k)-(z_1(x_i,y_k)+d_{sw}(x_i,y_k))] & z_{wt} > (z_1+d_{sw})-\delta \end{cases} \quad \text{(5-13b)}$$

Where $W(z^r_{wt}) = \left|-R\alpha e^{\alpha[z^r_{wt}-(z_1+d_{sw})]}\right|$

Equation (5-13b) is a Taylor series of equation 5 about z^r_{wt}. The unknown coefficients (A^r_{jn},B^r_{jn}) at each iteration are obtained and the 3-D series expansions for discharge potential (Eq. 5-10) are then fully defined; however the top boundary condition is still not met exactly due to the initially incorrect location of z_t.The series solution provides a hydraulic head distribution ($h^r_m(x_i,y_k,z^r_{wt}(x_i,y_k))$) at each control point along the initial top surface boundary. Due to the zero pressure head condition along the water table, in each iteration, following equation may be used to modify water table location:

$$z^{r+1}_{wt}(x_i,y_k) = z^r_{wt}(x_i,y_k)+\tau(h^r_m(x_i,y_k)-z^r_{wt}(x_i,y_k)) \quad \text{(5-14)}$$

Where τ is a relaxation factor. The solution of the constrained minimization of the resultant over determined system of equations (Equations (5-12a) and (5-13a)) was here handled using an active set algorithm [*Byrd and Waltz*, 2011]. Note that the condition used in equation 5-13b ($z^r_{wt} \rightarrow h^r_m$) is satisfied as the solution converges.

5.5 Analysis

The following section describes a set of tests used to first investigate the impact of sediment layer geometry and properties on lake-aquifer interaction, and secondly assess the quality and numerical behavior of the series solution. In the first test case, different combinations of lake sediment geometry and material properties are considered. The efficiency of the semi-analytical series solution method is assessed in the second test case.

Normalized continuity (Equations (5-15a), (5-15a)) and boundary condition (Equations (5-15a), (5-15a)) errors are evaluated along each interface (*m*) at points located halfway between the control points used within the constrained least squares solution as follows:

$$\varepsilon^{\text{flux}}_m \quad (x,y) \quad = \frac{\frac{\partial\phi^-}{\partial\eta}(x,y)-\frac{\partial\phi^+}{\partial\eta}(x,y)}{\max(F(x,y))-\min(F(x,y))} \text{ for } m=2,\ldots, M \quad \text{(5-15a)}$$

$$\varepsilon^{\text{head}}_m \quad (x,y) = \frac{\varphi^-_{(x,y)}-\varphi^+_{(x,y)}}{\max(\varphi)-\min(\varphi)} \qquad \text{for } m=2,\ldots, M \quad \text{(5-15b)}$$

Along the modeled domain top surface interface, $z_t(x,y)$, the normalized flux boundary condition error is

$$\varepsilon_1^{\text{flux}}(x,y) = \frac{F(x,y) - \frac{\partial \phi^+}{\partial \eta}(x,y)}{\max(F(x,y)) - \min(F(x,y))} \quad (5\text{-}15c)$$

and along the bottom bedrock, the no-flow condition error is defined as:

$$\varepsilon_{M+1}^{\text{flux}}(x,y) = \frac{\frac{\partial \phi^-}{\partial \eta}(x,y)}{\max(F(x,y)) - \min(F(x,y))} \quad (5\text{-}15d)$$

Here, $\max(F(x,y))$ and $\min(F(x,y))$ [LT^{-1}] refer to the minimum and maximum flux applied across the top surface which is also the maximum flux in the domain, and $\max(\varphi)$ and $\min(\varphi)$ [L] are the maximum and minimum value of the pressure head in the entire domain. The (-) and (+) signs refer to the top and bottom of each interface respectively.

5.5.1 Example 1: Effect of lake sediment on lake-Aquifer interaction

The method derived herein is able to accurately simulate 3-D flow in lake-aquifer systems where the sediment layer (with an arbitrary geometry) is considered independently rather than using a conductance condition, as is common. We intend to use this method to evaluate the effect of sediment geometry and material properties on the flow distribution through the lake bed. The same lake geometry is used for all examples in this section, $(z = 3 - 0.6\exp(-0.0025r^2))$, where r is the radius from the center of the domain. Two different lake sediment geometries are considered: a) a sediment layer of uniform thickness, and b) a sediment layer with non-uniform thickness which is more reflective of real lake sediment geometry (Figure 5-3a). To assess the effect of lake sediment thickness, two different sediment thicknesses are considered for each geometry: a) a thin layer with a maximum thickness of 23 cm, and b) a thicker layer with a maximum thickness of 46 cm. To investigate the effect of sediment material properties, three ratios of porous media to sediment hydraulic conductivity (P =1, 20 and 200) are considered (Figure 5-3b). The uniform hydraulic head at the lake is set equal to the water elevation of $H_r = 2.65$ m for all the examples in this section (Figure 5-3a). The parameter chosen are specific to this problem, but the results are expected to generalize to other system geometries.

All examples are subject to a uniform specified infiltration rate of $R = 10^{-4}$ md^{-1}. Surface water depth, d_{sw}, (Equation (5-5)) is zero for all control points along the top surface boundary of the modeled

domain, except those in direct contact with surface water body. A value of α =20 m^{-1} is selected for all 12 examples considered in this section. A 100 m x 100 m computational domain with no-flow conditions along the sides and bottom is used, where the lake and seepage surfaces are the outlet for recharge. The initial guess used for the water table location is uniformly equal to the lake uniform hydraulic head, iteratively determined thereafter. The solutions are obtained for two-layer systems (aquifer and sediment layer) using $J = N = 28$, and $NC_x=NC_y$ =30 (900 control points) along each evaluation surface (i.e., the modeled domain top boundary, the layer interface between the sediment layer and aquifer, and the bedrock).

Figure 5-3b illustrates the normalized seepage flux distribution (normalized with respect to the specified infiltration rate (R)) through a cross section along lake bed for the 12 examples considered in this section, while Figure 5-3c demonstrates the variation of minimum, average and the maximum of normalized seepage flux at the lake bed as P increases for 4 sediment layer geometries. Because of the symmetry of the domain, only the flux distribution along the plane of symmetry through the middle of the lake is reported. These solutions were identified after 60 iterations with a relaxation factor of τ = 0.10 used to control the convergence behavior of the unknown water table. Note that this strong relaxation is required to insure convergence of the solution where a large value of α=20 generates a sharp transition between recharge and discharge regimes. The solution with a smaller α value can converge using a larger relaxation factor at the expense of relaxing the top boundary conditions in the transition zone. For the uniform sediment layer, it is seen that as the ratio of aquifer to sediment conductivity (P) increases, the flux distribution becomes more spatially uniform, though only slightly (Figure 5-3b). Figure 5-3c depicts the small increase in the minimum and the average seepage flux at the lake bed, and decrease in its maximum as P increases. This confirms the result of *Genereux and Bandopadhyay* [2001], though in their numerical simulation the thickness of uniform sediment layer depended upon the mesh size. Unlike with the uniform sediment, changes in thickness and conductivity in the non-uniform sediment layer have considerable impact, in a totally different manner, on lake bed flux distribution. As the aquifer to sediment conductivity ratio (P) and/or the thickness of the sediment layer increase, the flux distribution adjusts to increase the shoreline fluxes and decrease the off-shore seepage (Figure 5-3b). This effect may increase the risk of seepage-induced erosion at the shoreline due to the large concentrated flux through the lake bed, and in the extreme, is consistent with results from 2-D Dupuit- Forchheimer models of lake seepage [*Bakker*, 2002; 2004; *Strack*, 1984]. Figure 5-3c shows that for the non-uniform layer problem, as P increases

the minimum and the average seepage flux at the lake bed decrease considerably, while the maximum flux increases. Effect of *P* on seepage flux distribution becomes more significant as the thickness of non-uniform sediment layer increases. Because the flow resistance of the thickest part of the sediment becomes significant, in all cases the impact of non-uniform sediment layer on lake bed seepage flux distribution may be attributed to the large resistance of the sediment layer off-shore compared to along the shoreline.

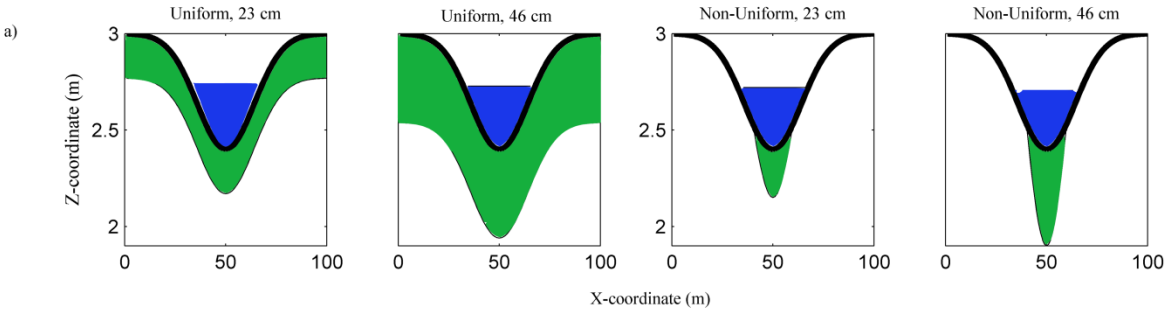

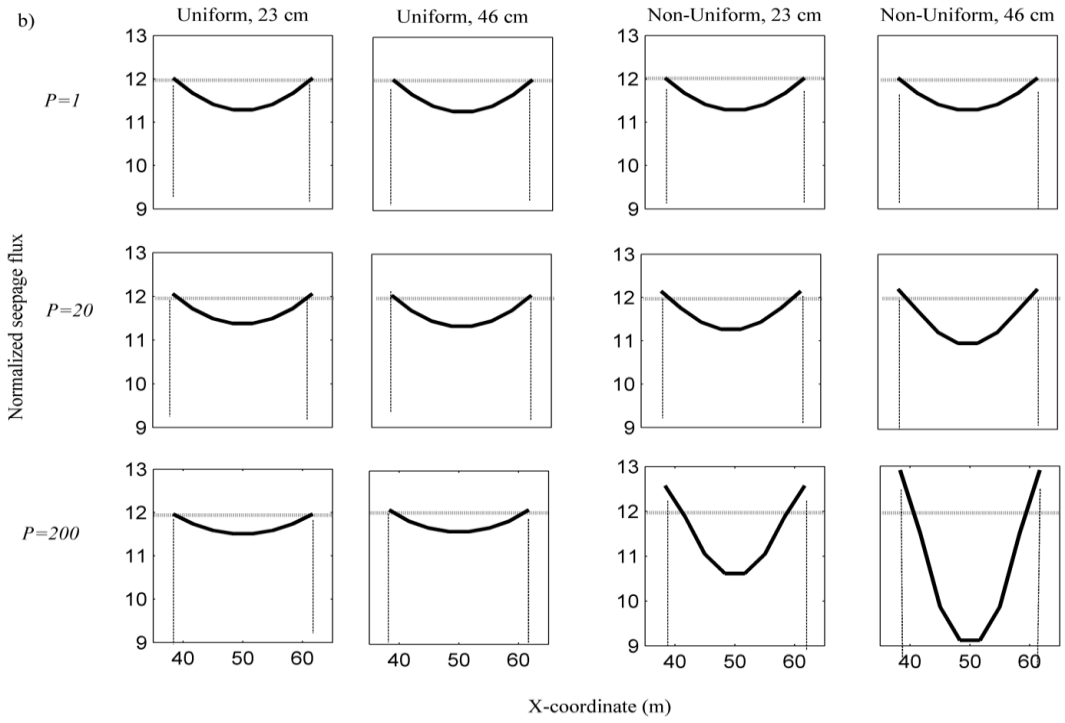

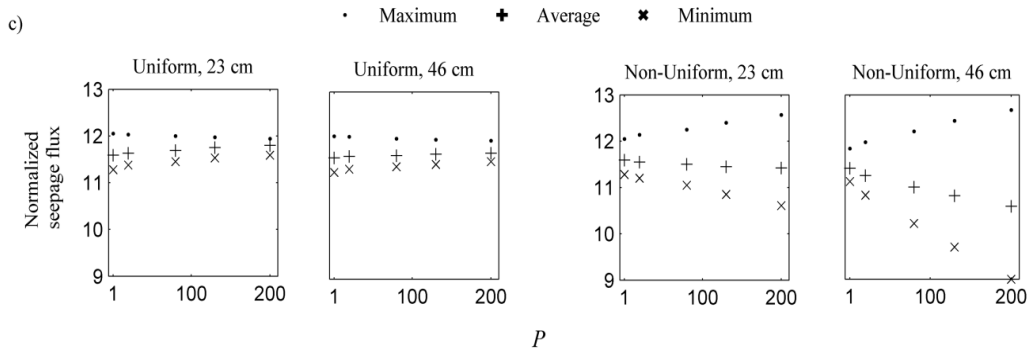

Figure 5-3. Layout of the normalized seepage flux distribution at the lake bed in lake-aquifer system. a) layout of four sediment layer geometries (green) with the same lake geometry, water level of 2.65 m (blue) is shown for four cases. b) normalized seepage flux distribution at the lake bed for four sediment layer geometries combined with three ratios of aquifer to lake sediment hydraulic conductivity (P=1, 20, 200), results shown along the plane of symmetry through the middle of the lake, a reference grey line depicts a value of normalized seepage flux=12. c) minimum, average and the maximum normalized seepage flux at the lake bed with respect to P for P=1, 20, 80, 130 and 200. Image from *Ameli and Craig* [2014].

Note that for all these simulations, the maximum normalized flux error along the modeled domain top surface, $\varepsilon_1^{\text{flux}}$, was on the order of 10^{-4}, while this measure along the remaining interfaces ($\varepsilon_2^{\text{flux}}$, $\varepsilon_3^{\text{flux}}$) are on the order of 10^{-5}. This test case explored the various impacts of sediment geometry and properties on flux distribution at the lake bed, and not surprisingly it has an effect on flow behavior in the aquifer.

We found that increased thickness of lake sediment can slightly uniformize the flux at the lake bed for an uniform sediment layer, but can considerably impact the lake bed flux at the shoreline and off-shore, respectively, if the sediment thickness is non-uniform. Contrary to 2-D models which use the Dupuit-Forchheimer approximation for the flow in the aquifer coupled with purely vertical flow through an uniform lake sediment [e.g.,*Bakker*, 2002; *Bakker*, 2004], the ratio of shoreline to off-shore fluxes is still quite mild; it is clear that the Dupuit-Forchheimer assumption, in cases such as these, overestimate the concentration of lake bed flux. However, the effects of (more realistic) non-uniform sediment thickness likely compensate for the artifacts of this assumption. This is consistent with studies [e.g., *Kacimov*, 2000], which have indicated that flow behaviour near the lake is often fully 3-D and Dupuit-Forchheimer approximation should be used with caution in problems of lake-aquifer interaction.

5.5.2 Example 2: Surface seepage flow from an unconfined aquifer

In a second example, the numerical behavior of the series solution method is assessed for the simulation of subsurface flow induced by evapotranspiration, infiltration and seepage faces in a hypothetical 3-layer unconfined aquifer (Figure 5-4a). The purpose of this test case is to both demonstrate the efficacy of the method and to examine its numerical convergence and error characteristics. The land surface topography used in this simulation was taken from a small river branch in the upstream area of the Nith river basin in southwestern Ontario, and two layer interfaces were generated by scaling and shifting the land surface elevations (Figure 5-4a). Note that, in this simulation, there is no surface water body explicitly specified. Here, compared to the previous test cases a larger value of α = 50 m^{-1} is selected to properly address the sharp transition between recharge zones and seepage faces. This sharp transition is caused from the geometrically complex topographic surface of this test case. The hydrological and hydrogeological parameters used are: $K_1 = 10\ \mathrm{m/d}$, $K_2 = 8\ \mathrm{m/d}$, $K_3 = 5\ \mathrm{m/d}$ and R=10^{-3} m/d. No-flow boundary conditions are considered along the domain sides and the bottom bedrock. In this example d_{sw} (Equation (5-5)) is equal to zero for all control points along the top surface boundary. A uniform initial guess for the water table location is placed a few centimeters higher than the lowest elevation of the land surface. Surface water was not allowed to pool; it is assumed that all discharge from the land surface runs off and the overland flow depth is zero. The solutions are obtained using NC_x = NC_y=32 (in total 1024 control points per interface) and a small number of degrees of freedom J = N =30, for a total of 5400 degrees of freedom (roughly equivalent to e.g., a 18x18x18 finite difference model). A relaxation factor τ = 0.06 is applied to control the convergence (Equation (5-14)). Again, here a larger relaxation factor could be used if a smaller value of α has been imposed to generate the exponential function in Equation (5-5). Figure 5-4a also shows the converged water table after 60 iterations. The contour of water table along with land surface topography are depicted in Figure 5-4b where highlighted (blue) discharge faces (represent zone C in Figure 5-1), are separated from recharge faces (the remaining part of the domain). Figure 5-4c shows the layout of flow path lines that clearly demonstrates flow concentration toward the seepage faces.

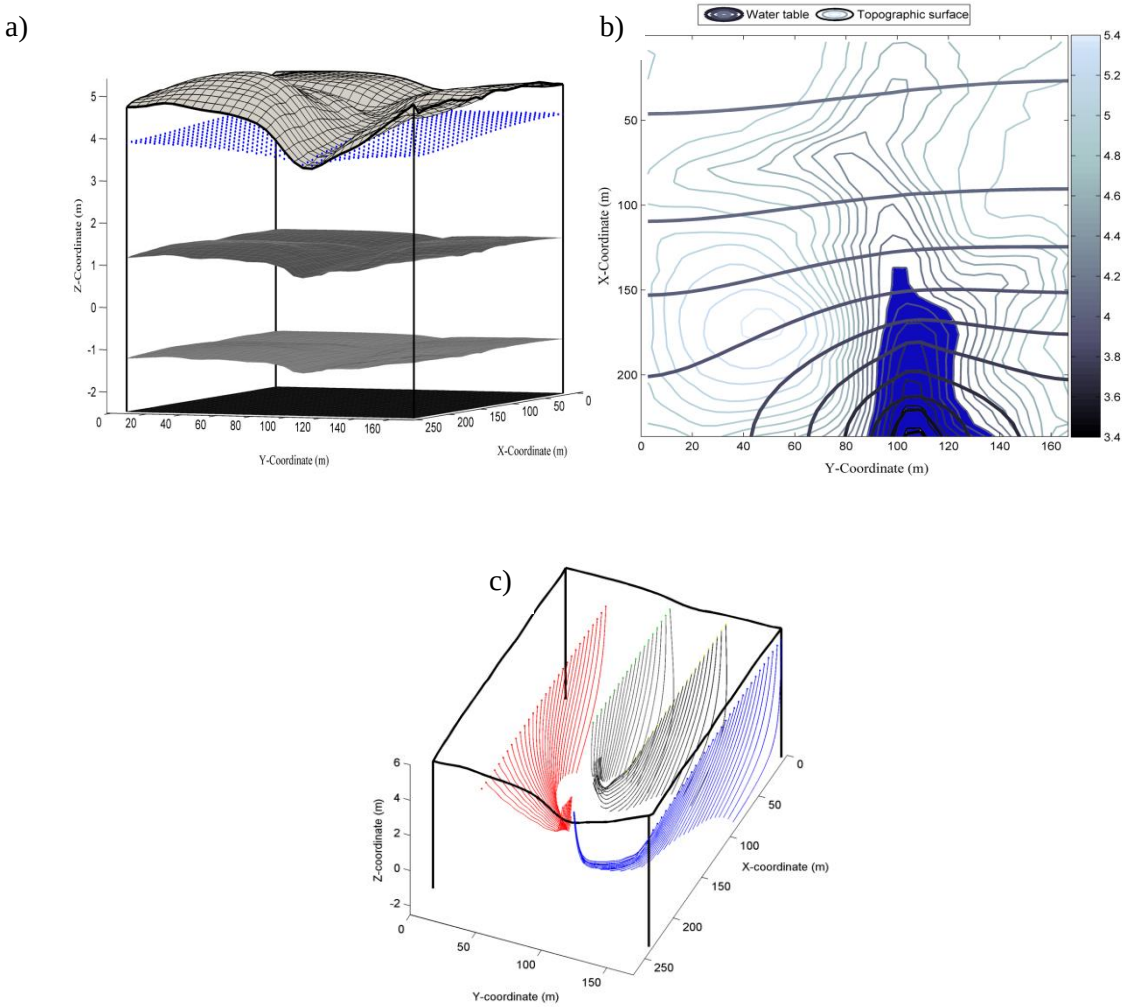

Figure 5-4. Solution in 3-Layer unconfined aquifer after 60 iterations, a) The layout of the stratified unconfined aquifer along with the converged water table (blue surface), b) contour of water table along with land surface topography with highlighted discharge faces, c) The layout of the flow path lines. Image from *Ameli and Craig* [2014].

Note that using Equation (5-5) to estimate the seepage face with zero pressure head, while significantly improving convergence skill of the algorithm, can still lead to relatively abrupt changes in surface fluxes over short distances. This manifests as Gibbs phenomenon. To mitigate this issue, the land surface has been slightly smoothened using LOWESS function of MATLAB (Figure 5-4a). This is an inherent challenge for the series solution method: while smooth system geometry leads to well-behaved solutions, irregular geometry can be problematic.

Figure 5-5 shows the contour of normalized flux error ($\varepsilon_1^{\text{flux}}$) at the 1024 error evaluation points across the top boundary condition (z_t). The largest errors are along the seepage face (with the maximum of 2%) where there is an abrupt increase in F (x,y) due to the change from Neumann to Dirichlet condition. A smaller α value could have led to smoother F (x,y), but would increase the error in emulating the Dirichlet boundary condition along the seepage faces. Increased surface smoothing can also decrease the error, but potentially at the cost of deviating from the actual problem statement in ways which may impact conclusions made from model results.

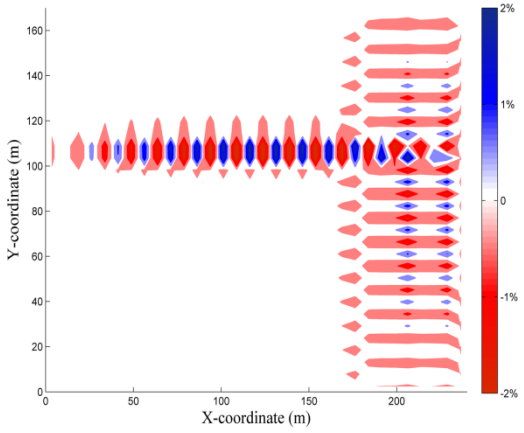

Figure 5-5. Contour of normalized flux error across the modeled domain top surface boundary ($\boldsymbol{\varepsilon_1^{\text{flux}}}$). Image from *Ameli and Craig* [2014].

Normalized flux error at 1024 error evaluation points across the first ($\varepsilon_2^{\text{flux}}$) and second ($\varepsilon_3^{\text{flux}}$) layer interfaces, and bottom bedrock ($\varepsilon_4^{\text{flux}}$) are lower than the top surface with the maximum of 10^{-4}, 10^{-4} and 10^{-5} for $\varepsilon_2^{\text{flux}}$, $\varepsilon_3^{\text{flux}}$ and $\varepsilon_4^{\text{flux}}$, respectively. In addition, the maximum normalized head errors, $\varepsilon_2^{\text{head}}$ and $\varepsilon_3^{\text{head}}$ across two layer interfaces are 10^{-4} and 10^{-5}, respectively. Except along the interfaces, continuity of mass, head and flux are exactly satisfied in the entire domain. The solution has converged well after a reasonable number of iterations. Figure 5-6 depicts the convergence behaviour of the solution; the average absolute pressure head error at 1024 error evaluation points along the water table exponentially converges to zero.

Despite the presence of a free boundary, and the presence of natural geometry and stratification, the series solution approach appears to be an efficient alternative to numerical schemes for the simulation

of 3-D steady flow in a naturally complex unconfined aquifer system as long as Gibbs phenomenon is controlled. One way to accomplish this is to feed the model only well behaved problem descriptions. Future research is needed to properly account for physically necessary discontinuities in flux.

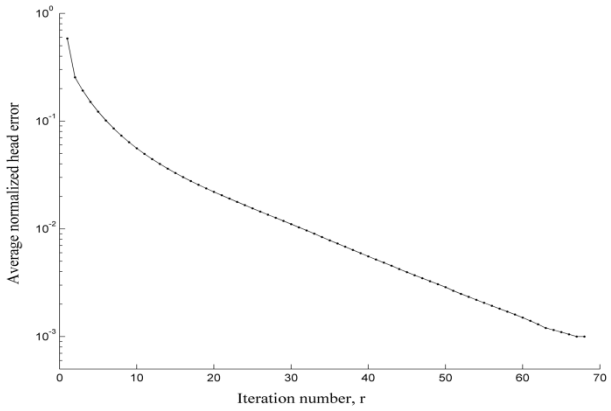

Figure 5-6. Convergence behaviour of the water table with $\boldsymbol{\tau}$ = 0.06. Image from *Ameli and Craig* [2014].

5.6 Conclusion

A general semi-analytical solution approach for free boundary steady groundwater-surface water interaction in a 3-D stratified unconfined aquifer has been developed and assessed in this chapter. The free boundary water table surface may be located through a robust iterative scheme and using a novel approach to estimate the flux along the modeled domain top surface boundary, and handle both Neumann and Dirichlet surface conditions without compromising convergence properties. The semi-analytical series solutions accurately simulated 3-D flow with acceptable rates of convergence and errors in the water table location. Because the method does not rely upon volume discretization, boundary errors, internal flow and pressure head values, and flux distribution at the ground surface are immediately available as continuous functions of space. The method was used to provide some insights into the impact of lake sediment geometry and properties on lake-unconfined aquifer interactions. Results demonstrated that lake sediment geometry and properties have a variable effect on the seepage distribution through the lake bed. While flux distribution in non-uniform sediment layers are significantly impacted by contrasts in conductivity, uniform sediment layers are likely to have relatively uniform flux distributions, with less sensitivity to lake bed material properties. The application of the developed model to a problem driven by a real topography pulled from a DEM

indicated that the number of degrees of freedom required to obtain an accurate solution for a realistic problem with a high rate of convergence is small.

Chapter 6
Semi-analytical solutions for assessing pumping impacts on groundwater-surface water interaction

6.1 Introduction

Horizontal wells and radial collector wells are sometimes considered as suitable alternatives to vertical wells for water withdrawal or remediation of contaminated groundwater systems. Radial collector wells are able to withdraw a large quantity of groundwater and surface water with a small drawdown. The appropriateness of radial collector wells for river bank filtration (RBF) and pump and treat applications has been reported by many researchers [e.g., *Moore et al.*, 2012; *Patel et al.*, 2010]. Understanding the interaction between radial collector wells, regional groundwater flow and surface water features requires a robust model with the ability to provide three dimensional details in the vicinity of both the well and surface water body. In addition, to realistically incorporate the effect of long radial arms (commonly longer than 80 m), the variation of inflow along these arms must be taken into account and it is desirable to effectively simulate the head distribution at the resolution of the well caisson (i.e., at the centimeter scale). Simulation of multi scale problems such as these is challenging using discrete numerical models. When applying grid-based methods to address arbitrary orientations of small diameter radials, high grid resolution is required which leads to computational inefficiency. For example, to accurately obtain the drawdown-discharge relationship of a single horizontal well in a homogenous aquifer with a regular geometry (a box domain of 150m*480m*24m), *Haitjema et al.* [2010] used a MODFLOW model of 1,846,314 cells. The requirements of models used for the design of RBF and pump and treat systems will be even stricter; in the design process, the assessment of different scenarios including various layouts and length of radial arms is required.

These conditions are well suited for the application of the analytical element method (AEM) where no horizontal or vertical grid discretization is required. More importantly, distributed singularities along the well axis are able to mimic the behavior of each arbitrarily-oriented arm regardless of its length and diameter. Researchers have recently extended AEM for the simulation of 2-D and 3-D flow toward a partially penetrating vertical well [*Bakker*, 2001; *Luther and Haitjema*, 1999], a single horizontal well [*Bakker and Strack*, 2003; *Luther*, 1998; *Steward and Jin*, 2001; 2003] and radial

collector well [*Bakker et al.*, 2005; *Luther and Haitjema*, 2000]. However, the discharge-drawdown relationship in the previously cited literature was obtained for isolated pumping well(s). More recently *Haitjema et al.* [2010] and *Moore et al.* [2012] have extended these AEM models to incorporate the interaction between horizontal well(s) and other regional features including rivers and regional flow. Rivers in these models have been treated using a group of constant head line sinks; this is accompanied by a simple 1-D Cauchy boundary (head dependent) condition to incorporate the effect of vertical resistance in the vicinity of the river. This treatment compromises the proper incorporation of river geometry and material properties.

3-D AEM models have been typically developed for flow toward wells located in homogenous confined aquifers where the no-flow top and bottom boundary conditions can be properly addressed by the method of images. Emulating free boundary conditions (i.e., the water table) at the top of modeled domain may be challenging, and in the past has been handed using distributed singularities. In the few research studies in which a free boundary condition at the water table has been considered, many auxiliary geometric features (e.g., doublet sinks or panel sinks) were applied external to the domain to aid in satisfying the phreatic surface boundary conditions [*Luther and Haitjema*, 1999; *Luther and Haitjema*, 2000]. Aquifer stratification with a regular layer interface has also been included in AEM models where 1) an additional analytic elements are externally applied to assist in satisfying the continuity conditions across layers [*Luther*, 1998] or 2) the domain is discretized vertically into many aquifers each with constant conductivity (the multi-aquifer model of [*Bakker et al.*, 2005]). In spite of the ability of AEM to emulate pumping well behavior, the treatment of phreatic surface or layer stratification using auxiliary singularities is challenging particularly in that there are no unique guidelines about the location, type and number of required singularities.

The series solution model developed in chapter 5 has been shown to properly address the phreatic surface, complex stratification, and non-regular surface water geometry. As stated in chapter 3, both series solution methods and AEM satisfy the linear groundwater governing equation exactly. Here, based on superposition, the series solution model for 3-D groundwater-surface water interaction developed in chapter 5 is augmented with a set of analytic elements (line sinks) which are used to represent pumping wells. The coupled series-AEM method was first used by *Bakker* [2010] to simulate 2-D interaction between river, homogenous confined aquifer and a vertical pumping well where series method was employed to emulate the flow boundary conditions at the sides of the domain. The series-AEM model is here intended to investigate 3-D groundwater-surface water

interaction induced by surface water bodies, infiltration, and a radial collector well in a naturally complex stratified unconfined aquifer. This series-AEM model is able to 1) discern the origin of well water and 2) estimate the percentage of well water captured from surface sources. It may be an efficient tool for designing RBF systems. This semi-analytical grid-free model is here used to assess the impact of pumping rate on the hydrological connectivity between river and radial collector well which plays a significant role in the performance of RBF systems.

6.2 Background

During the past decade, radial collector wells have been designed and installed in aquifers in the vicinity of stream or lake to withdraw naturally filtered surface water for supplying municipal drinking water (e.g., as done in the Saylorville well-field in the Des Moines River Valley, Iowa [*Moore et al.*, 2012]). The efficiency of each design is assessed by the ability of the well to induce recharge from surface water [*Moore et al.*, 2012]. In addition to pumping capacity, the quality of the water obtained using RBF systems is very important. Generally the water captured by RBF is the mixture of regional groundwater and surface water, each with different qualities. For example, the installed RBF systems in the vicinity of the Des Moines River Valley captures river waters which are being naturally treated for undesirable surface water constituents (such as pathogens) by passing through coarse grained river bed sediment [*Gollnitz et al*., 2005]. At the same time, groundwater in this area is higher in hardness, alkalinity, dissolved iron, manganese and solids [*Moore et al.*, 2012]. The identification of the mixture quality prior to construction requires detailed understanding of the expected interaction between regional groundwater, the radial collector well and adjacent rivers.

Modeling of the interaction between groundwater, surface water and well can provide useful insights into the physics of this challenging interaction; provided the appropriate boundary conditions are used. There are typically three assumptions used in the application of boundary conditions along radial arms in groundwater modeling literature; uniform flux, uniform head and constrained non-uniform head along the radial well screen. The latter is most in agreement with the actual behavior of long horizontal arms which exhibit considerable head losses inside the screened pipes where both flux and head are non-uniform; the friction loss equation (e.g., Darcy-Weisbatch) may be used to define the relationship between head along the well screen. In the case of laminar flow with negligible head losses inside the pipes, the second assumption is valid. The uniformity of flux assumption may only be valid for a very short radial screen, and is not a suitable option for application to the radial

collector well problem. Mesh-based numerical models have been widely used to address the interaction between groundwater, surface waters and wells using the finite element [*Ophori and Farvolden*, 1985] and finite difference method [*Chen et al.*, 2003; *Haitjema et al.*, 2010; *Patel et al.*, 1998; *Rushton and Brassington*, 2013a; b]. However, a mesh-based model may not be an efficient tool for the purpose of designing radial collector wells for river bank filtration. In addition to the high grid resolution required to properly address the small well diameter and arbitrary orientations of radial arms, the implementation of the boundary condition along the well screen is also challenging in standard numerical models. Typically, flow toward radial arms is approximated using head dependent boundary cells [*Patel et al.*, 1998] or the drain package [*Kelson*, 2012] accompanied by an entry resistance (conductance factor) in MODFLOW.

Semi-analytical approaches have been applied to simulate flow toward horizontal well(s) in confined and unconfined aquifers. A boundary integral equation model has been developed by *Bischoff* [1981] to simulate 3-D flow toward a 3-arm radial collector well in a confined aquifer. *Haitjema* [1982] used third order horizontal line sinks and line doublets to incorporate the 3-D effects of a horizontal well in a homogenous confined aquifer. These geometric features have been replaced by a set of line sinks at the centerline of the well each with linearly-varied strength to properly emulate the constant head condition (or non-uniform flux) along horizontal well(s) in homogenous confined aquifers by *Steward and Jin* [2001]; 2003]. *Bakker et al.* [2005] have discretized a confined aquifer into several (fictitious) horizontal homogenous aquifers where horizontal flow inside each aquifer is computed analytically based on Dupuit-Forchheimer approximation; vertical flow is approximated with a vertical resistance of a leaky layer between aquifers using a finite difference method. This quasi 3-D multi-aquifer analytic element model accounts for the head losses inside the screen pipe and skin effects (non-uniform head along the screen). A separate horizontal aquifer is assigned to the collector well which is represented by a multilayer line sinks. The skin effect is approximated by applying the entry resistance parameter to inflow of the well screen. Using vertical discretization, this model can incorporate the effect of stratification with parallel layer interfaces. AEM models have also been developed to simulate 3-D flow toward horizontal well(s) in homogenous unconfined aquifers [*Luther and Haitjema*, 2000]. In these models, the phreatic surface position was located through an iterative scheme in a manner similar to series solution approach discussed in chapter 4. Using AEM, auxiliary elements (e.g., point sinks and sink rings) were required outside the flow domain to aid in satisfying a zero-recharge boundary condition along phreatic surface.

Surface water features can also be incorporated in AEM models using a set of line sinks. This enables AEM to consider the interaction between regional groundwater, surface water and radial collector wells for the application to RBF system design. For the interaction between a single horizontal well and river in a 2-D homogenous confined aquifer, *Haitjema et al.* [2010] estimated entry resistances for the simulation of converging flow to well and stream in a 2-D Dupuit-Forchheimer AEM code (GFLOW) generated by *Haitjema* [1995]. These developed resistances obtained for an infinitely long single horizontal well in a confined aquifer and can roughly approximate the effect of vertical flow toward river and horizontal well. These resistances were later used in a 2-D MODFLOW model as well [*Kelson*, 2012]. The AEM model developed by *Haitjema et al.* [2010] was one of the first studies which semi-analytically approximated the interaction between a river and well; this model has provided similar well yields to that generated by a high resolution MODFLOW model for a given well drawdown. Although the model was accurate enough for the purpose of discerning well yield, the authors suggested that it cannot provide accurate 3-D details in the vicinity of a well and stream and therefore should not be used for the purpose of designing the radial collector well in RBF systems. *Moore et al.* [2012] have linked this 2-D regional model with the quasi 3-D local-scale multi-aquifer model developed by *Bakker et al.* [2005] (in a manner similar to the telescoping mesh refinement used in MODFLOW) to develop a general AEM model for the design of radial collector well in a RBF system. First, the regional 2-D AEM model is calibrated based on observed steady-state drawdown and measured water level. At the proper distance from radial collector well where vertical flow is negligible (three or four times the representative leakage length), the fluxes are applied as perimeter boundary conditions for the 3-D local-scale model. The local interaction between the radial collector well and river is then assessed using the quasi-3D Multi-aquifer AEM model.

The study of *Moore et al.* [2012] has also suggested important guidelines for choosing the optimum length, number, elevation and location of a radial collector well in the design phase. They showed that the elevation of lateral arms has a minor impact on well drawdown and yield, and can be determined based on operational, construction and maintenance considerations. They mentioned that the laterals should be placed well below the caisson water level while the water level in the caisson should be located above the pump inlet to meet suction-head requirements and desirable water yield. At the same time, the relative elevation of radial collector well with respect to the bedrock should be high enough to avoid hydraulic interference. They have also found that with the same cumulative lateral screen length, a longer lateral works better than more laterals with shorter length; this is because of

less hydraulic interactions between laterals. They concluded that the relative distance between radial collector well and river is the most important control on the efficiency of RBF systems.

6.3 Problem Statement

Figure 6-1 shows the general layout of a 3-D stratified unconfined aquifer in the presence of a radial collector well, surface infiltration and a surface water body. The aquifer has a length of L_x and L_y in the x and y directions and is subdivided into M layers, each with uniform conductivity, K_m. Each layer is bounded by the surface $z_m(x,y)$ above and $z_{m+1}(x,y)$ below, and $z_1(x,y)$ refers to the topographic surface. The bottom boundary with surface $z_{M+1}(x,y)$ and sides of the aquifer are impermeable. Similar to chapter 5, the a priori unknown water table surface, $z_{wt}(x,y)$, is defined as the surface with zero pressure head. The radial collector well consists of multiple horizontal arms of the same length of l_{wl} and located at an elevation of z_{wl}. Radial arms are allowed to intersect the layer interfaces.

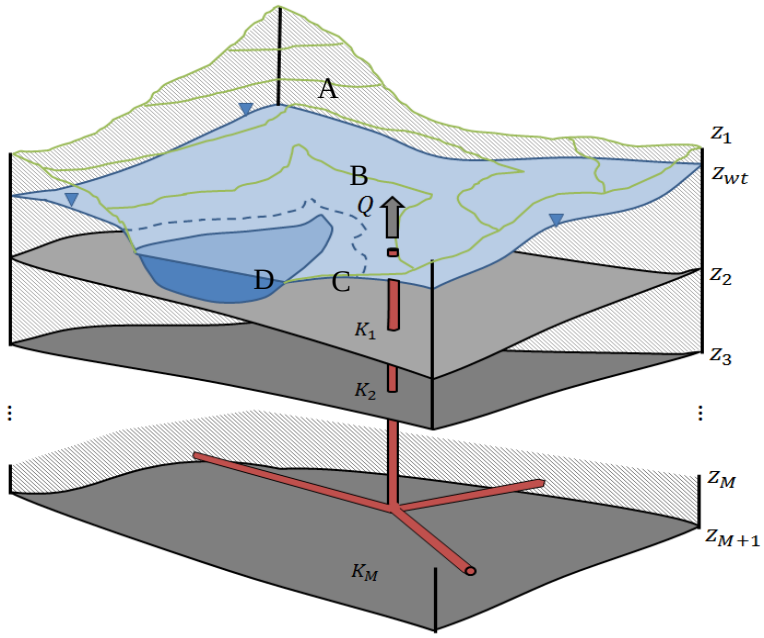

Figure 6-1. Layout of the general 3-D problem. M layers are bounded by $z_{M+1}(x,y)$ corresponding to the bottom bedrock and $z_1(x,y)$ corresponding to the land surface. Layers are separated by the interfaces $z_m(x,y)$. Radial arms of the same length of l_{wl} are located at the elevation of z_{wl}. A, B, C, D refers to the zones where different types of surface conditions are applied: (A) uncorrected infiltration, (B) transition between recharge and discharge zones, (C) seepage face and (D) surface water.

In a manner similar to chapter 5, the 3-D Laplace equation in terms of a discharge potential, ϕ_m [L^2T^{-1}], governs groundwater flow in each layer of the aquifer

$$\frac{\partial^2 \phi_m}{\partial x^2} + \frac{\partial^2 \phi_m}{\partial y^2} + \frac{\partial^2 \phi_m}{\partial z^2} = 0 \quad \text{for } m = 1, \dots, M \tag{6-1}$$

Similarly, the 3-D discharge across an interface can be decomposed into vertical and horizontal components (equation 5-3). Across the sides of the domain, no-flow conditions in *x* and *y* directions are imposed.

$$\frac{\partial \phi_m}{\partial x}(0, y, z\ ) = \frac{\partial \phi_m}{\partial x}(L_x, y, z\ ) = 0 \text{ for } m = 1, \dots, M \tag{6-2}$$

$$\frac{\partial \phi_m}{\partial y}(x, 0, z\ ) = \frac{\partial \phi_m}{\partial y}\left(x, L_y, z\ \right) = 0 \text{ for } m = 1, \dots, M \tag{6-3}$$

The modeled domain is bounded above by $z_t(x, y)$, which is the surface defined as the water table surface ($z_{wt}(x, y)$) where the water table is lower than the land surface, and the land surface ($z_1(x, y)$) at areas in direct contact with surface water body. Unlike in chapter 5, here the surface water body boundary condition (surface D in figure 6-1) is fixed, rather than generated as a by-product of the solution. A constant head Dirichlet condition equal to the surface water stage, H_r [L], is applied across the areas in direct contact with surface water body. For the implementation of the remaining surface conditions (recharge, transition and seepage faces), the scheme presented in section 5.3 is used where $F(x, y)$ is obtained using equation 5-5.

$$\frac{\partial \phi}{\partial \eta}\left(x, y, z_{wt}(x, y)\right) = F(x, y) \tag{6-4}$$

$$\frac{\phi\ \ \left(x, y, z_1(x, y)\right)}{K_1} = H_r \tag{6-5}$$

Continuity of flux and pressure head along each layer interface ($m = 2, \dots, M$) can be represented as:

$$\frac{\partial \phi_m}{\partial \eta}\left(x, y, z_m(x,y)\right) = \frac{\partial \phi_{m-1}}{\partial \eta}\left(x, y, z_m(x,y)\right) \tag{6-6}$$

$$\frac{\phi_m\left(x, y, z_m(x,y)\right)}{K_m} = \frac{\phi_{m-1}\left(x, y, z_m(x,y)\right)}{K_{m-1}} \tag{6-7}$$

No-flow conditions are also imposed along the bedrock which is a flat interface with a planar geometry in this chapter.

$$\frac{\partial \phi_M}{\partial \eta}\left(x, y, z_{M+1}(x,y)\right) = 0 \tag{6-8}$$

At the radial collector well, the a priori unknown head is obtained based on a given pumping rate, although the method is able to properly address the reverse case. In a manner similar to *Steward and Jin* [2003], two boundary conditions must be satisfied along the entire well screen length. First, the head along the cylindrical face of the well must be uniform, which implies zero head loss along the well screens. This is applied by setting the head at a set of NC_w control points (located along screens surface) equal to the head at a specified but arbitrary position p along this boundary.

$$\frac{\phi\ \ \left(x_p, y_p, z_p\right)}{K_p} = \frac{\phi_{\ddot{m}}(x_w, y_w, z_w)}{K_{\ddot{m}}}\ for\ w = 1 \ldots NC_w \tag{6-9}$$

Here $\ddot{m}$ is conditional upon the layer where each control point or the specified point, p, are located. This ensures the ability of the model to address the cases where radial arms intersect the layer. For the second boundary condition at the collector well, the summation of unknown strengths along a pumping well is set equal to the pumping rate Q

$$\sum_{i=1}^{N_s} {\sigma_0}^i l^i = Q \tag{6-10}$$

where N_s, ${\sigma_0}^i$ and l^i are the number of segments, constant strength of each segment, and segment length, respectively, as discussed in section 3.3. In applying this condition, the unknown head in the radial collector well, H_w, may be obtained.

Both the series solution and AEM solution satisfy the linear 3-D Laplace equation. Therefore superposition theory suggests that in each layer ($m = 1 \dots M$) of a stratified unconfined aquifer, a discharge potential function of the following form can be applied:

$$\phi_m(x,y,z)=\phi_m^{Series}(x,y,z) + \phi^{AEM}(x,y,z) \tag{6-11}$$

The series solution to groundwater flow in each layer of a stratified unconfined aquifer developed in chapter 5 is (equation 5-10):

$$\phi_m^{Series}(x,y,z) = \sum_{j=0}^{J-1}\sum_{n=0}^{N-1} cos\,\omega_j x\, cos\,\omega_n y\,[A_{jn}^m cosh(\gamma_{jn}z) + B_{jn}^m sinh(\gamma_{jn}z)] \tag{6-12}$$

The AEM solution representing the radial collector well is:

$$\phi^{AEM}(x,y,z) = \sum_{i=1}^{N_s} \phi_w^i(x,y,z) \tag{6-13}$$

where the discharge potential effect of the i^{th} segment, ϕ_w^i, in global coordinate system is obtained based on the closed form expression developed by *Steward and Jin* [2003] in local coordinate system of each segment (equation (3-8)). The resulting equation is:

$$\phi_w^i(x,y,z) = -\frac{{\sigma_0}^i}{4\pi} ln \frac{\left[\left(x-x_0^i+L\right)^2 + \left(y-y_0^i\right)^2 + \left(z-z_0^i\right)^2\right]^{\frac{1}{2}} + \left(x-x_0^i+L\right)}{\left[\left(x-x_0^i-L\right)^2 + \left(y-y_0^i\right)^2 + \left(z-z_0^i\right)^2\right]^{\frac{1}{2}} + \left(x-x_0^i-L\right)} \tag{6-14}$$

where x_0^i, y_0^i and z_0^i refer to the center of each segment in the global coordinate system of the ground water model. The total discharge potential function (equation (6-11)) must satisfy the no-flow condition at the sides and bottom of the domain (equations (6-2) & (6-3) & (6-8)). Again based on superposition both series and AEM solution must satisfy these boundary conditions. As explained in chapter 5, the series portion of solution already satisfies no-flow condition at the sides by judicious selection of ω_j, ω_n and γ_{jn} as (repeated form equation 5-11):

$$\omega_j = \frac{j\pi}{L_x};\ \omega_n = \frac{n\pi}{L_y};\quad \gamma_{jn} = \pi\sqrt{\frac{j^2}{{L_x}^2} + \frac{n^2}{{L_y}^2}} \quad \text{for} \quad j = 0 \ldots . J-1 \ \&\ n = 0 \ldots . N-1 \tag{6-15}$$

In addition, to satisfy no-flow condition along the bottom bedrock by the series portion of the solution, B_{jn}^m (Equation (6-12)) must be equal to zero (similar to [*Read et al.*, 2005]). The method of images is here used to enable AEM to satisfy no-flow conditions at the sides and bottom of the domain. Therefore equation (6-11) is modified as

$$\phi_m(x,y,z) = \phi_m^{Series}(x,y,z) + \sum_{i=1}^{N_s} \phi_w^i(x,y,z) + \sum_{j=1}^{N_I}\sum_{i=1}^{N_s} \phi_I^i(x,y,z) \tag{6-16}$$

Where ϕ_I^i refers to discharge potential correspond to the image of i^{th} segment and N_I is the number of image wells. As discussed in section 3.3 the strength associated with each image segment is identical to its real counterpart and only their locations (x_0^i, y_0^i and z_0^i) are different. Note that, the no-flow boundary condition at the sides and bottom of the domain only met exactly when N_I approaches infinity. The uniformity of head condition, in addition, met exactly when N_s approaches infinity.

6.4 Solution

The 3-D semi-analytical series-AEM solution for the interaction between groundwater, surface water bodies and a radial collector well (Equation (6-16)) in each layer of a stratified unconfined aquifer is obtained by identifying unknown coefficients of the series solution (A_{jn}^m in equation (6-12)) and AEM terms ($\sigma_0{}^i$ in equation (6-14)). These coefficients are calculated using a constrained least squares numerical algorithm. Similar to chapter 5, the priori unknown water table elevation, $z_{wt}^r(x,y)$, (where r is the iteration number) is obtained through a robust iterative scheme. A set of NC control points, are located along the top of the modeled domain surface, $z_t^r(x,y)$, bedrock surface ($z_{M+1}(x,y)$) and each layer interface ($z_m(x,y)$) to characterize the error in the top boundary condition, and the continuity of flux and head conditions (equations (6-4) to (6-8)). Note that here *NC* is the product of NC_x and NC_y which are the number of uniformly spaced control points in *x* and *y* direction respectively. Initially, the top of modeled domain surface, $z_t^1(x,y)$, is assumed to be equal to the river water stage, H_r at all control points. The uniformity of head boundary condition along the radial screens is satisfied by applying equation (6-9) at a set of NC_w control points located along the screens surface. The unknown coefficients for each guess of the water table surface, are calculated by

minimizing the total sum of squared boundary and continuity condition errors (at control points along the mentioned interfaces and well screen surfaces) that is constrained with equation (6-10) such that the total inflow be equal to pumping rate Q at the radial collector well. The total sum of squared errors (TSSE) is here subdivided into the errors along mentioned evaluation curves:

$$\mathrm{TSSE} \quad = \mathrm{SSE_t} + \sum_{\mathrm{m}=2}^{M} \mathrm{SSE_m} + \mathrm{SSE_w} \tag{6-17}$$

The subscripts refer to the errors along the top surface (t), layer interfaces (m) and radial collector well screens (w).

where

$$\mathrm{SSE_t} = \sum_{\substack{i=1 \\ i\notin C}}^{NC} \left[\frac{\partial \phi_{\ddot{m}}}{\partial \eta}\left(x_i, y_i, z_{wt}^{r}(x_i, y_i)\right) - F(x_i, y_i)\right]^2 + \sum_{\substack{i=1 \\ i\in C}}^{NC} [\frac{\phi_{\ddot{m}}\left(x_i, y_i, z_1\ (x_i, y_i)\right)}{K_{\ddot{m}}} - H_r]^2 \tag{6-17a}$$

Where C is the set of coordinate indices for control points in direct contact with the surface water body (Dirichlet zone). $\ddot{m}$ is the layer where the control point along the top surface is located.

$$\mathrm{SSE_m} =$$

$$\sum_{i=1}^{NC} \left[\frac{\partial \phi_m}{\partial \eta}\left(x_i, y_i, z_m(x_i, y_i)\right) - \frac{\partial \phi_{m-1}}{\partial \eta}\left(x_i, y_i, z_m(x_i, y_i)\right)\right]^2 +$$

$$\sum_{i=1}^{NC} \left[\frac{\phi_m(x_i, y_i, z_m(x_i, y_i))}{K_m} - \frac{\phi_{m-1}(x_i, y_i, z_m(x_i, y_i))}{K_{m-1}}\right]^2 \quad \text{for } m=2, \ldots, M \tag{6-17b}$$

$$\mathrm{SSE_w} = \sum_{w=1}^{NC_w} \left[\frac{\phi_{\ddot{m}}(x_w, y_w, z_w)}{K_{\ddot{m}}} - \frac{\phi\ (x_p, y_p, z_p)}{K_p}\right]^2 \tag{6-17c}$$

here $\ddot{m}$ is defined as the layer where the control points or the point (p) with a fixed position are located along the screens.

For each layer (m =1, ..., M), the unknown series solution (A_{jn}^{mr}) and AEM ($\sigma_0{}^{ir}$) coefficients at the r^{th} iteration, are calculated and the 3-D series-AEM expansion for discharge potential (equation (6-16)) is then fully obtained; however the top boundary condition along the water table surface (z_{wt}) is still

not met exactly due to the initially incorrect location of water table. Equation (6-16) provides a hydraulic head distribution ($h_m^r(x_i, y_k, z_{wt}^r(x_i, y_k))$) at each control point along the initial top surface boundary. Due to the zero pressure head condition along the water table, in each iteration, following equation may be used to modify water table location:

$$z_{wt}^{r+1}(x_i, y_i) = z_{wt}^r(x_i, y_i) + \tau(h_m^r(x_i, y_i) - z_{wt}^r(x_i, y_i)) \quad (6\text{-}18)$$

where τ is a relaxation factor. An active set algorithm proposed by *Byrd and Waltz* [2011], is used to solve the constrained least squares solution of the resultant over-determined system of equations (equations (6-10) & (6-17)) where a Lagrange multiplier is used to implement the constraint equation.

6.5 Analysis

This section describes a set of tests used to first demonstrate the quality and numerical behavior of the series-AEM method for the simulation of a river bank filtration process and secondly assess the impact of pumping rate on the hydrological connection between river and radial collector well. In the first test case, the efficiency of the solution is assessed for the simulation of the interaction between groundwater, river and radial collector well in the presence of infiltration and a free boundary phreatic surface in a hypothetical naturally complex stratified unconfined aquifer. Different values of the pumping rate are considered in the second test case to investigate the impact of pumping rate on the percentage of surface water body withdrawal by the collector well. This demonstrates that how the hydrological connection between river and radial collector well varies by pumping rate.

Equations (5-15) are used to evaluate the normalized uniformity, continuity and boundary condition errors along each interface (m) and radial screens at points located halfway between the control points used within the constrained least squares solution. Note that the water stage of the river (H_r) is used for normalizing head errors.

6.5.1 Example 1: River Bank Filtration process in a naturally complex unconfined aquifer

The numerical behavior of the series-AEM solution developed in this chapter is assessed for the simulation of the interaction between river, groundwater and radial collector well in a 2-layer unconfined aquifer (shown in figure 6-2). The land surface topography used in this example is the modified form of a small river branch in the upstream area of the Nith river basin in southwestern

Ontario. The hypothetical layer interfaces are generated by scaling and shifting the land surface elevations (Fig. 6-2). The hydrological and hydrogeological parameters used are: $K_1 = 100\ \mathrm{m/d}$, $K_2 = 80\ \mathrm{m/d}$ and R=10^{-4} m/d with a given pumping rate of 60000 m^3/d at the radial collector well. The radial collector well located at z_{wl}=7 m on the outside corner of the river (100 m distance between the center of the collector caisson and river in each direction). It is comprised of 2 arms of the same length of l_{wl} =100 m and radius of 0.50 m. Material properties of the aquifer, length, relative distance to river and pumping rate of the radial collector well used in this example are consistent with commonly seen properties for river bank filtration analysis (as shown by experimental-numerical analysis in Saylorville wellfield [*Moore et al.*, 2012]). No-flow boundary conditions are considered along the domain sides and the bottom bedrock. In this example, d_{sw} (figure 5-2) is equal to zero for all control points along the top surface boundary, since the surface water body is directly implemented using constant head condition (equation (6-5)). A uniform head of $H_r = 44.60$ m is considered along the river. The solutions are obtained using NC=2304 control points per interface (top of modeled domain, and layer interface), and NC_w= 600 control points along each radial arm. Evenly-spaced control points along the length of each arm are placed at 6 positions along the perimeter of arm section (left, right, top-left, top-right, bottom-left, bottom-right). This layout of control points ensures the proper representation of radial collector well and accurate estimation of the contribution of each well water source. The number of series terms of J= N = 40 and line segments of N_s=30 (along each arm) are required to ensure accurate representation of river, free boundary, precipitation and radial collector well. This small number of degrees of freedom for a total of 3932 degrees (roughly equivalent to e.g., a 16x16x16 finite difference model) shows the computational efficiency of the grid-free solution developed here for this challenging problem. Twelve image wells (6 images and 6 images of images) are also considered for each arm to guarantee the accurate implementation of the no-flow condition at the sides of the domain. To satisfy the no-flow condition along the bottom bedrock by AEM portion of the solution an additional 13 image wells are considered (including 12 images of image wells used to emulate no-flow condition at sides and one image well below the radial collector well). A relaxation factor τ = 0.05 (equation (6-18)), exponential function parameter α =50 and transition zone depth δ=50 cm (equation 5-5) are applied to control the convergence. Similar to chapter 5, here a larger relaxation factor could be used if a smaller value of α has been imposed to generate the exponential function in equation 5-5. Figure 6-2 shows the converged water table and path lines move toward radial collector well after 45 iterations.

Figure 6-2 only depicts the layout of flow path lines toward the radial collector well to illustrate the capacity of the developed model to simulate river bank filtration process. These path lines were generated using back tracking from 180 particle releasing points located along the radial collector well (this figure only depicts 60 path lines terminated at the particle releasing points located at the left and right sides of arms section). Blue path lines originate from the river and move toward two radial arms aligned with the *x* and *y* axes. Red lines depict the path lines which do not originate from the river. The percentage of well waters captured from the river can be estimated by assigning a weight to each path line. This weight is equal to the obtained strength of the line sink segment $(\sigma_0{}^i)$ which the path line is terminated in the collector well. Therefore in releasing 180 particles from the well, the flow-weighted path lines suggest that approximately 57% of radial collector well inflow originate from the river. This percentage increases as the radial collector well location approaches the river. Note that to obtain this percentage all 180 particle releasing points (located at 6 sides of arms section) have been used in the back tracking procedure to generate the path lines. This relative contribution of each source to radial collector well water seems to be only mildly sensitive to the solution parameters including the number of control points NC and NC_w, number of particle releasing points, number of series terms *N* and *J*, and number of line sink segments N_s. For example by doubling the number of control points along each arm or the number of line sink segments, mentioned percentage changes less than 1%. In addition, this percentage changes less than 2% when only control points located at the left and right sides of each arm are used in the solution instead of control points located at all 6 sides.

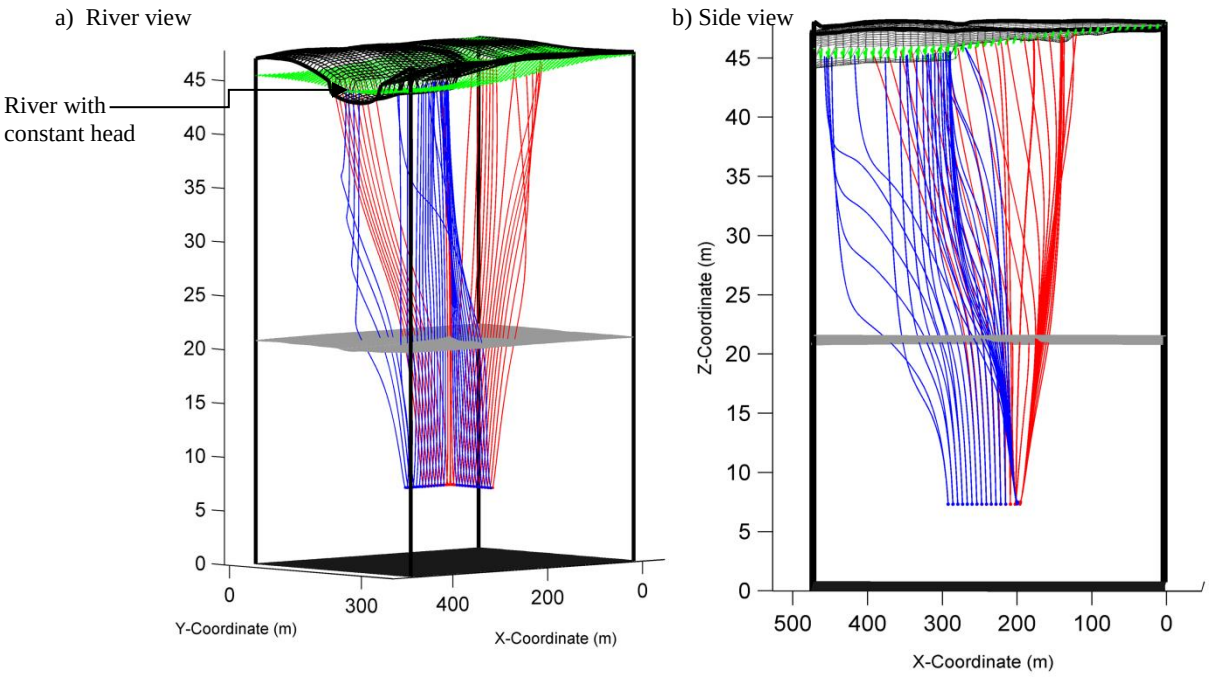

Figure 6-2. Series-AEM solution in 2-Layer unconfined aquifer after 45 iterations, a) river view, b) side view. Green surface depicts the converged water table. Flow path lines move toward collector well are shown in blue (originated from river) and red (not originated from river) lines. Note that there is varying scale in *x*, *y* and *z* directions.

Figure 6-3 depicts the convergence behavior of the water table and the variation of the unknown head at the collector well with iteration number. Figure 6-3a shows the average normalized pressure head error $(h_m^r(x_i, y_i) - z_{wt}^r(x_i, y_i)$ at 2304 error evaluation points along the water table converges almost exponentially to zero. The unknown head at the collector well also approaches to 43.50 m as shown in figure 6-3b.

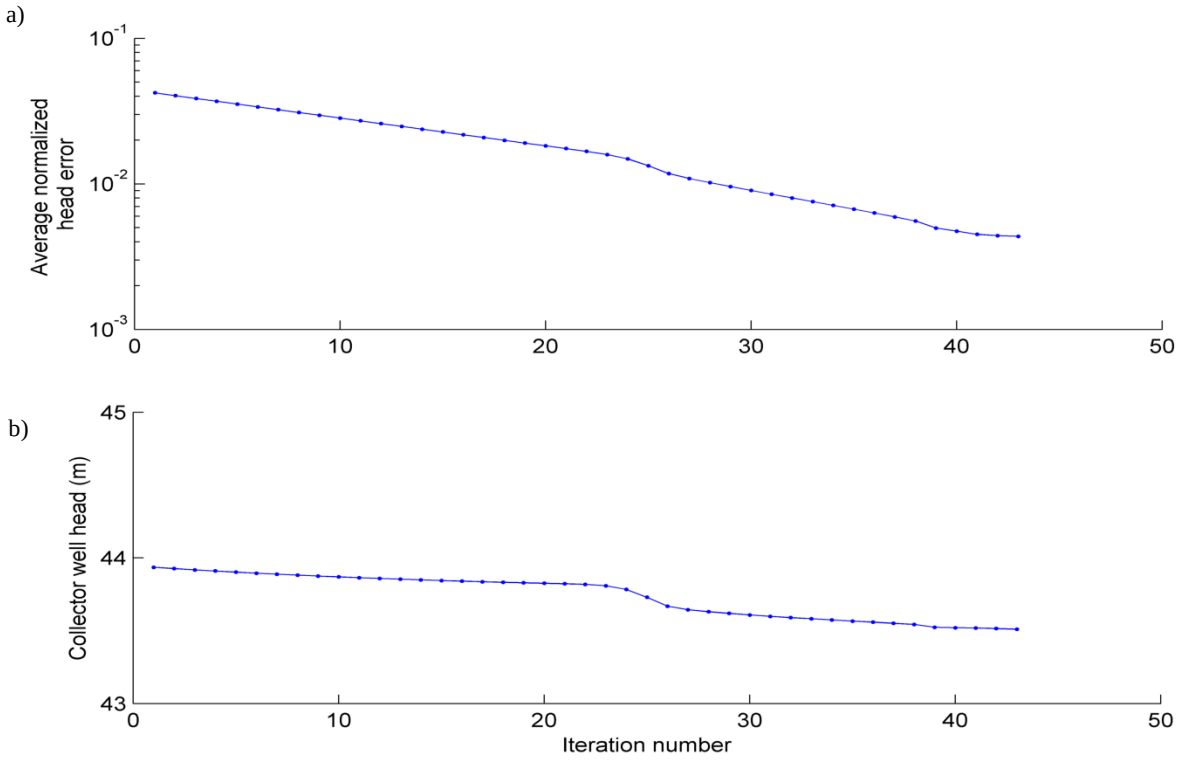

Figure 6-3. Convergence behavior of the solution. a) Variation of average normalized head error along the water table and b) collector well head with respect to iteration number.

As stated earlier, the series-AEM solution developed here satisfies the governing equation exactly. Using 12 Image wells for each arm, no-flow conditions at the sides of the domain were satisfied with a normalized error on the order of 10^{-8}. In addition, no-flow conditions along the bottom bedrock were satisfied with a normalized error on the order of 10^{-14} using 13 image wells as discussed earlier. The constraint on total inflow into the radial collector well (equation (6-10)) is met exactly. Using least squares (equation (6-17)), however, there are numerical errors along 2304 error evaluation points in the implementation of boundary and continuity conditions along the top, layer interface and radial screens as shown in figure 6-4. Figure 6-4a shows the contours of normalized flux error ($\varepsilon_1^{\text{flux}}$) at the 2132 error evaluation points (points in direct contact with surface water body are not included) across the top boundary interface where the specified flux ($F\ (x, y)$from equation 5-5) was applied. The largest errors are at the projection of radial arms on the top surface with the maximum of 9%. The mean absolute normalized flux error along this interface is 1.3%. At the remaining 172 control points along the top interface which are in direct contact with the river, the normalized head error is on the order of 10^{-4} (not shown here). Figures 6-4b show that the normalized flux errors at

2304 error evaluation points across the first ($\varepsilon_2^{\text{flux}}$) layer interface are lower than the top surface with the maximum of 0.4% for $\varepsilon_2^{\text{flux}}$, which again occur at the projection of radial arms along this interface. In addition, the contour of normalized head error, $\varepsilon_2^{\text{head}}$ across 2304 evaluation points at the layer interface are shown in figure 6-4c with the maximum of 0.4%. The head uniformity at 1200 control points located along two radial arms is also assessed in figure 6-4d. As stated earlier, along each arm 600 control points are located at 6 sides of the arm section. The top and bottom portions of figure 6-4d depicts the normalized head error at 6 sides of the arm aligned with the *x* and *y* axes, respectively. The maximum normalized uniformity of head error is 0.6% and 2% along the arm in *x* and *y* directions, respectively, which occurs at the ends of each arm. Note that by increasing the number of line segments (N_s) the maximum error decrease and the uniformity of head along the arms is met more accurately, but the computational cost considerably increases. For example by doubling the number of line segments, the maximum normalized uniformity of head error at the ends of each arm decreases almost 30% (not shown here).

a)

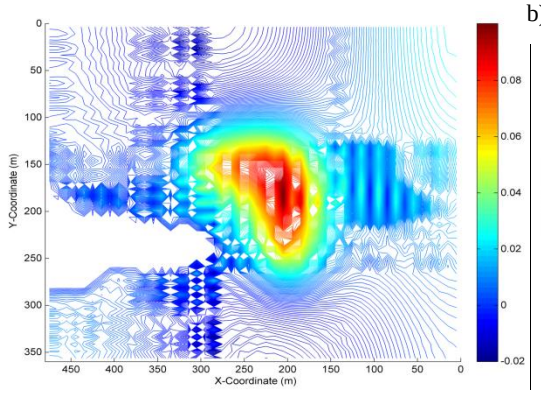

b)

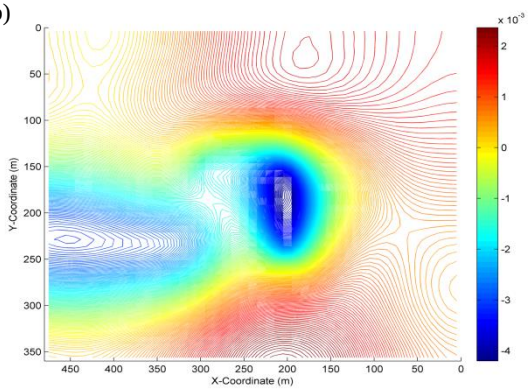

c)

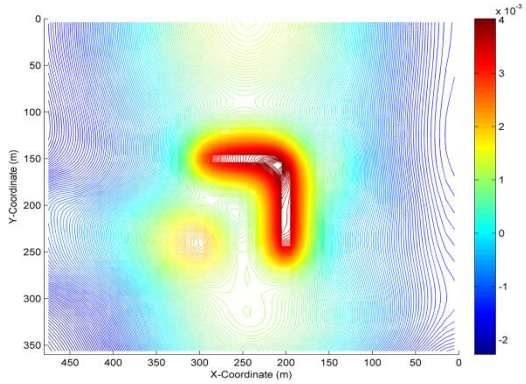

d)

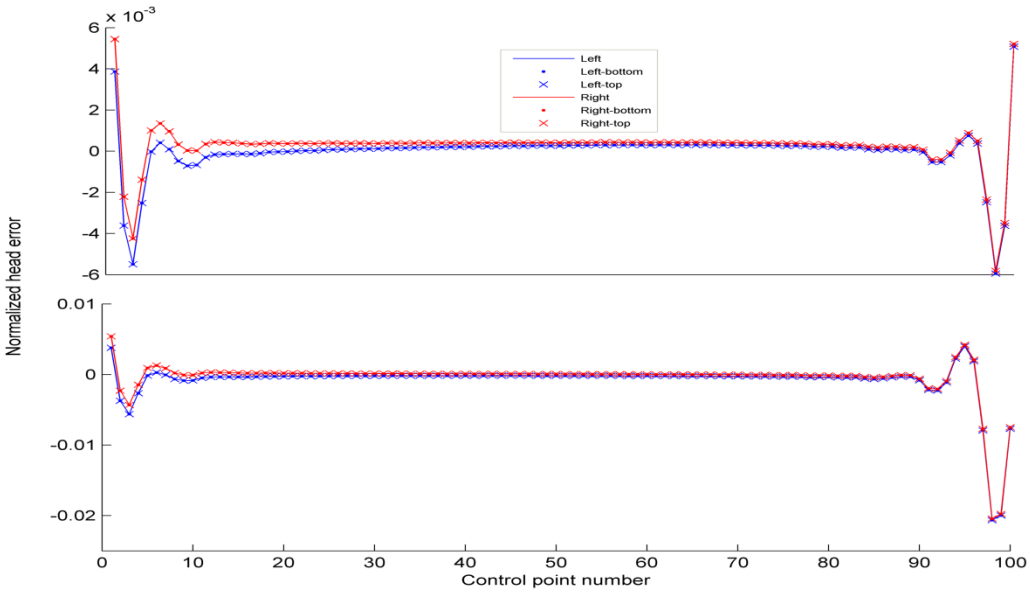

Figure 6-4. Normalized error of boundary and continuity conditions along evaluation interfaces. a) contours of normalized flux error along the water table surface, b) contours of normalized continuity of flux error along the first layer interface, c) contours of normalized continuity of head error along the first layer interface, d) uniformity of head normalized error along the control pints located at 6 sides of the arm in *x* (top) and *y* (bottom) directions.

Results suggest that the series-AEM model developed here is able to properly address fully 3-D interaction between radial collector well, regional groundwater and surface water body despite the presence of a free boundary, precipitation, natural geometry and stratification. The sources of collector well waters can be accurately discerned and the percentage of surface water and groundwater captured by the well is approximately obtained while this percentage is almost insensitive to solution parameters. The model can be easily used for various layouts and length of radial arms while there is no limitation on the relative distance between collector well and river. Therefore it is may be an effective tool for the purpose of RBF system design. The model can easily be extended for the simulation of the interaction between lake, groundwater and collector well.

6.5.2 Example 2: Pumping rate impact on hydrological connection between river and well

In a second example, the impact of pumping rate on the percentage of well waters captured from the river is assessed. A homogenous aquifer ($k = 100$ m/d) with a simple geometry is considered (figure 6-5). A uniform head of $H_r = 35.80$ m is assumed along the river as shown in figure 6-5. The solution

parameters and properties of the radial collector well shown in the figure (red and blue lines show the arm in *x* and *y* direction, respectively) are the same as example 1 except the location of the collector well caisson (in plan view) which is exactly below the center of the river. This minimizes the effect of the relative distance between collector well and river on the percentage of well waters captured from the river which has been suggested [*Moore et al.*, 2012] as the major control in RBF system design.

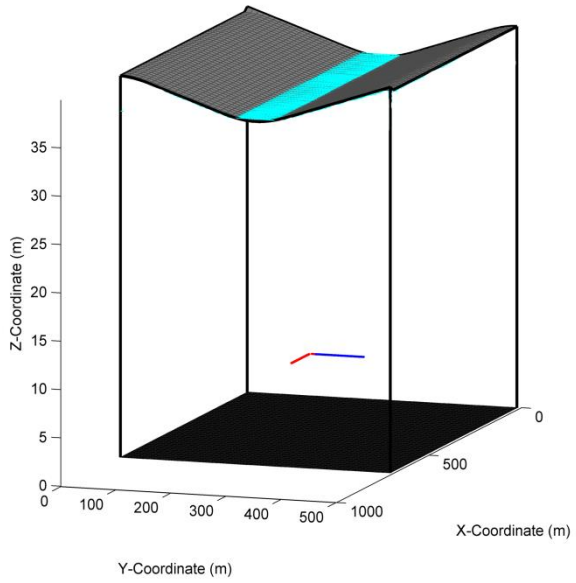

Figure 6-5. Layout of a radial collector well located in a homogenous unconfined aquifer with a simple geometry. Red and blue lines show the arm in *x* and *y* direction, respectively. River with a simple geometry is shown in a light blue.

To assess the effect of pumping rate on the hydrological connection between river and collector well, three different pumping rates are considered. Figure 6-6 depicts the converged water table and path lines move toward the radial collector well after 45 iterations where Q at the radial collector well is equal to a) 30000 m^3/d, b) 60000 m^3/d and c) 120000 m^3/d. These figures only depict path lines terminated at the control points located at the left and right side of each arm section instead of all 6 sides control points used in the solution. Red lines depict the path lines which do not originate from the river and blue lines are the path lines move toward radial collector well from the river. Figure 6-6 shows for the same number of path lines for all three cases, the last case (Q = 120000 m^3/d) has the most number of path lines which do not originate from the river. For the case with Q =30000 m^3/d, 84% of radial collector well waters originate from the river, while for the case with Q =60000 m^3/d and Q =120000 m^3/d this percentages decrease to 76% and 65%, respectively.

a) $Q = 30000\ m^3/\mathrm{d}$ b) $Q = 60000\ m^3/\mathrm{d}$

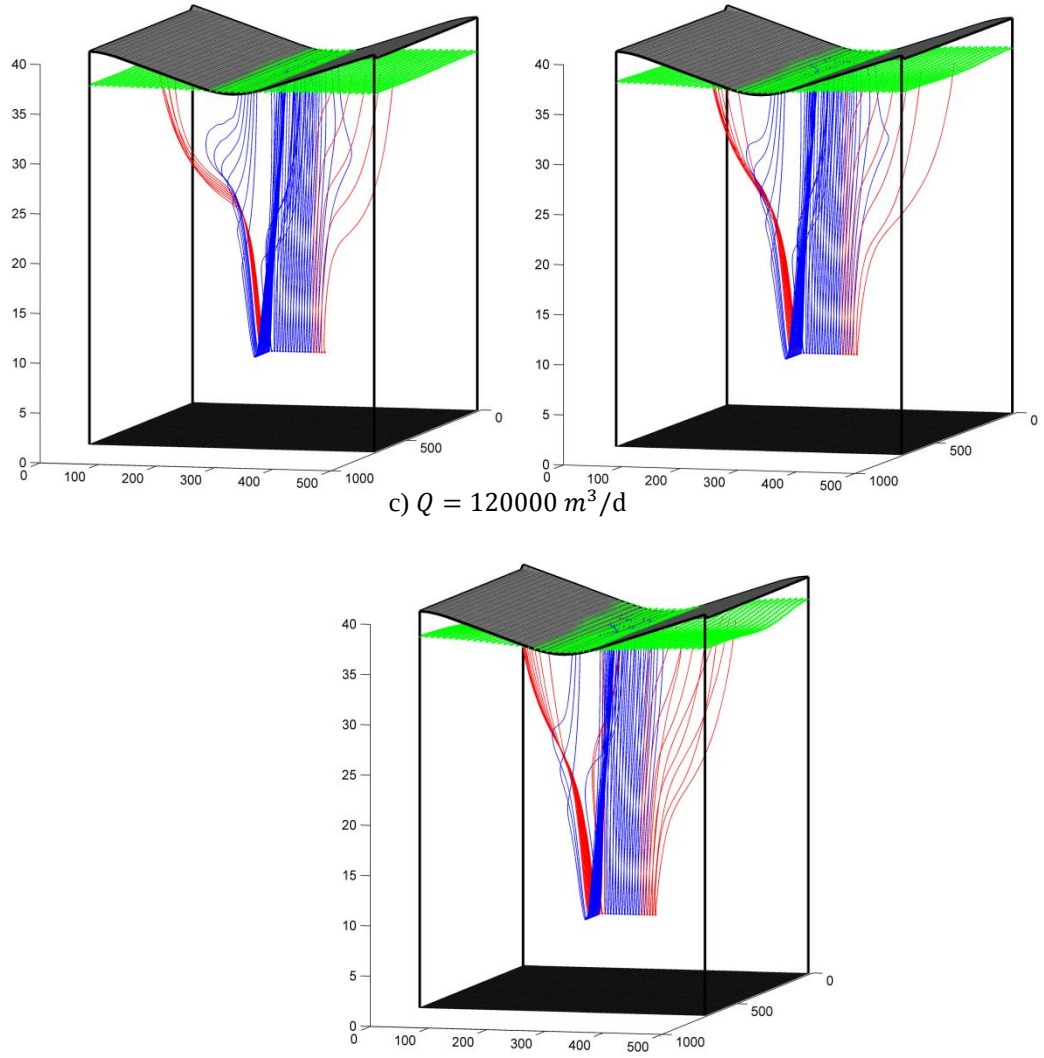

c) $Q = 120000\ m^3/\mathrm{d}$

Figure 6-6. Series-AEM solution in a homogenous unconfined aquifer after 45 iterations, for a) Q = 30000 m^3/d, b) Q = 60000 m^3/d and c) Q = 120000 m^3/d. Green surfaces depict the converged water table. Flow path lines are shown in blue and red lines where red path lines do not originate from the river.

This decrease in the percentage of the captured water from river as pumping rate increases may be attributed to the cone of depression generated in the vicinity of the collector well. Due to construction considerations, the placement of the collector well right below the river is challenging and a minimum relative distance between river and collector well is required [*Moore et al.*, 2012]. No

doubt, the effect of pumping well on attenuating the well waters captured from the river is increased as the relative distance between the collector well and river increases.

6.6 Conclusion

A general semi-analytical series-AEM solution for the simulation of fully 3-D interaction between collector well, free boundary groundwater and surface water body in a naturally complex stratified unconfined aquifer has been developed and assessed in this chapter. This model accurately simulated 3-D flow with acceptable errors in a priori known water table location. Infiltration, naturally complex geometry and layer stratification, river geometry and material property, and radial collector well have been considered. Each arm of the radial collector well in this model is allowed to have an arbitrary orientation and intersect the layer interface(s). This grid-free model also indicated that for a realistic problem a small degrees of freedom required to ensure an accurate solution which is converged after a reasonable number of iterations. Internal flow and pressure head values, radial collector well inflows, flux distribution at the ground surface and boundary errors are immediately available as continuous functions of space. This robust model was able to discern well waters origin and approximate the percentage of well waters captured from different sources (e.g., river, groundwater). Therefore, it may be used for the purpose of designing RBF systems. In spite of all the advantages of the model, the mandatory no-flow side boundaries in some specific cases may limit the application of the model for the simulation of the regional interaction between groundwater, surface water and radial collector well. It is clear that, for this case at least, there were non-physical boundary artifacts, which would be alleviated by using larger domain extents.

The method was also used to provide some insights into the impact of pumping rate of the collector well on hydrological connection between river and collector well. Despite that the radial collector well was placed below the river, results suggested that as the pumping rate increases the percentage of well waters originating from the river decreases. This effect can compromise the appropriateness of RBF systems.

Chapter 7
Conclusions and future directions

7.1 Conclusions

This thesis improved the capacity of existing semi-analytical series solution and AEM approaches for solving groundwater-surface water interaction problems which are challenging to solve using mesh-based methods. Geometrically complex topography and layer stratification, surface water bodies, collector well geometry, a priori unknown phreatic surface (free boundary condition) and infiltration have been properly incorporated into a general model framework which can be successfully applied to complex systems with small number of degrees of freedom. The free boundary water table surface was identified using a robust iterative scheme. These solutions exactly satisfied mass balance and governing equation in the entire domain, as well as no-flow conditions at the sides of the domain. Boundary and continuity conditions across the layer interfaces are met with acceptable rates of error. Because the methods developed here do not rely upon volume discretization, internal flow, error and pressure head values are immediately available as continuous functions of space. These accurate, fast, continuous and grid-free models were able to assess factors controlling groundwater-surface water interaction problems with or without pumping well(s). In the following, the main contributions attained in each chapter are outlined.

- In chapter 4, the series solution approach was extended to address 2-D saturated-unsaturated flow close to a constant head river in geometrically complex stratified unconfined aquifers. The capillary fringe zone was considered as a distinctive zone with free boundary at the top and bottom. The continuous saturated-unsaturated series solution model provided a description of the water distribution and flow direction in both saturated and unsaturated zones. This model was used to assess the impact of saturated and unsaturated material properties on the behavior of unsaturated and capillary fringe flow, and the a priori unknown water table elevation.

- In chapter 5, the series solution method was extended to simulate 3-D groundwater-surface water interaction in a geometrically complex stratified unconfined aquifer, where flow was controlled by water exchanges across the land surface including evapotranspiration, infiltration, seepage faces and exchange with surface water bodies. Without having to

assume the location of seepage faces, the location of phreatic surface was obtained. This model was demonstrated to be an efficient tool to simulate flow toward seepage faces in a realistic stratified unconfined aquifer with a small number of degrees of freedom. In addition, the grid-free series solution model explicitly represented the lake sediment geometry and properties. This model was used to show that, for a uniform sediment layer, increased thickness of lake sediment can slightly uniformize the flux at the lake bed. For non-uniform sediment layer, increasing the maximum thickness of lake sediment can considerably increase and decrease the lake bed fluxes at the shoreline and off-shore, respectively. In spite of this effect, results suggested that the commonly used scheme to incorporate lake sediment layer effects (the Dupuit-Forchheimer approximation coupled with the assumption of purely vertical flow through a uniform lake sediment) overestimates the concentration of lake bed flux.

- The 3-D series solution model was augmented with 3-D AEM based approach in chapter 6 to assess steady-state groundwater-surface water interaction between a radial collector well and river in naturally complex stratified unconfined aquifers. Limitations of AEM for the accurate representation of constrained free boundary phreatic surface, naturally complex stratification and surface water body were mitigated by coupling with a series solution model. The resultant model may be an efficient tool for the purpose of RBF system design. Radial collector well water sources and the percentage of well waters captured from each source (e.g., groundwater and river) can be accurately discerned. This continuous and grid-free model suggested that as pumping rate increases the appropriateness of RBF systems may be compromised by decreasing the percentage of river water captured by well.

The developed grid-free semi-analytical models in this thesis appear to be efficient alternatives to numerical methods for the simulation of 3-D steady-state groundwater-surface water interaction in cases where the mesh-related issues of numerical models can be problematic. However, these models are only efficient if Gibbs phenomenon is properly addressed. Gibbs phenomenon causes instability at sharp changes in geometry of the layers or boundary conditions across an interface. The former can be mitigated by a degree of surface smoothing and the latter may be somewhat addressed by using weighted least squares as done in chapters 5 and 4, respectively. However, these mentioned treatments are stopgap schemes and are not able to address the core problem. For example, in the models developed in this thesis, increasing the number of series term does not always lead to more

accuracy. In the examples presented in chapter 5, as N and J increase the accuracy of the top of the modeled domain free boundary condition increases until $N = J = 30$ and decreases thereafter. This is connected to the Gibbs phenomena issue. Indeed, by increasing the number of series terms, the sharp changes in geometry/boundary condition are mimicked more accurately, but the appropriateness of the series solution method in the remaining areas is compromised. This issue was simply shown in figure 3-1 for the curve fitting of a 1-D problem. Increasing the number of control points within the areas with higher potential for Gibbs phenomenon may not also lead to higher accuracy in the entire domain. As the number of control points along the areas including sharp changes increases, the contribution (weight) of these areas to the total series solution increases and the efficiency of the series solution method in the remaining areas is compromised. Gibbs phenomenon may also limit the applicability of the methods presented in chapter 6; for example, there must be enough distance between radial collector well elevation and topographic surface to ensure accurate representation of free boundary condition along the phreatic surface.

In addition to Gibbs phenomenon, there are other important issues to be recognized. The mandatory no-flow side boundaries assumed in all developed models may limit their application for the simulation of regional groundwater-surface water interaction particularly in the presence of pumping wells with a large discharge rate. Ideally the method may be somehow augmented to handle alternate boundary conditions. For unsaturated modeling, the unsaturated parameters (sorptive number and air entry pressure) were here constrained to be identical for different layers to ensure the linearity of the mathematical model. Using a non-linear least squares algorithm may circumvent this issue. Lastly, the model for saturated-unsaturated flow was developed based on the Gardner model to ensure separability and linearity of the governing equation. Series solutions model will not be able to incorporate other non-linear soil-water characteristic relationships (e.g., Van Genuchten), as the one unconquerable requirement of series solution methods is that the governing equation must be linear.

Although the developed series solutions and series-AEM models in this thesis circumvent the mesh-related issues of numerical models in some specific cases, these methods must be improved considerably to compete with numerical models in more general settings. In the following section, some recommendations for the improvement of these models in accompany with the applications of the developed models in the other fields are listed.

7.2 Future directions

As stated above the most challenging issue of the developed models in this thesis is Gibbs phenomenon. This issue may in the future be rectified by supplementing standard basis functions with special 'supplemental solutions', which handle local departures from generally smooth solutions, perhaps using the existing library of 2-D and 3-D AEM solutions. This approach properly worked for 1-D curve fitting of a complex function using a discrete Fourier series in chapter 3 but is much more challenging to implement as part of 2-D and 3-D series solution approach. Developing supplemental solutions with the ability to address 2-D and 3-D abrupt changes in surface geometry and boundary conditions may address the Gibbs phenomenon issues reported in this thesis.

Extending the developed models in this thesis for the simulation of transient groundwater-surface water interaction with or without pumping well(s) can also be a useful progress in the application of semi-analytical approaches. This may be done using Laplace transform method for topography-driven flow. For free boundary problems, the Laplace transform method may also be coupled with the developed models in this thesis to address some simplified transient cases (e.g., with the assumption of zero specific storage).

The models and techniques presented in this thesis can be used and extended to other fields of science. For example, the linearized separable equations which govern heat transfer may be addressed in a manner similar to the developed models in this thesis. Other application areas may include soil mechanics, laminar fluid flow, and electromagnetic systems.

References

Ameli, A. A., and J. R. Craig (2014), Semianalytical series solutions for three-dimensional groundwater-surface water interaction, *Water Resources Research*, *50*(5).
Ameli, A. A., J. R. Craig, and S. Wong (2013), Series solutions for saturated–unsaturated flow in multi-layer unconfined aquifers, *Advances in Water Resources*, *60*, 24-33.
An, H., Y. Ichikawa, Y. Tachikawa, and M. Shiiba (2010), Three-dimensional finite difference saturated-unsaturated flow modeling with nonorthogonal grids using a coordinate transformation method, *Water Resources Research*, *46*(11).
Anderson, E. I. (2003), An analytical solution representing groundwater-surface water interaction, *Water Resources Research*, *39*(3).
Bakker, M. (2001), An analytic, approximate method for modeling steady, three-dimensional flow to partially penetrating wells, *Water Resources Research*, *37*(5), 1301-1308.
Bakker, M. (2002), Two exact solutions for a cylindrical inhomogeneity in a multi-aquifer system, *Advances in Water Resources*, *25*(1), 9-18.
Bakker, M. (2004), Modeling groundwater flow to elliptical lakes and through multi-aquifer elliptical inhomogeneities, *Advances in Water Resources*, *27*(5), 497-506.
Bakker, M. (2010), Hydraulic modeling of riverbank filtration systems with curved boundaries using analytic elements and series solutions, *Advances in Water Resources*, *33*(8), 813-819.
Bakker, M., and E. I. Anderson (2002), Comment on "Numerical investigation of lake bed seepage patterns: effects of porous medium and lake properties" by Genereux, D., and Bandopadhyay, I., 2001. Journal of Hydrology 241, 286–303, *Journal of Hydrology*, *258*(1), 260-264.
Bakker, M., and O. D. Strack (2003), Analytic elements for multiaquifer flow, *Journal of Hydrology*, *271*(1), 119-129.
Bakker, M., and J. L. Nieber (2004), Two-dimensional steady unsaturated flow through embedded elliptical layers, *Water Resources Research*, *40*(12).
Bakker, M., V. A. Kelson, and K. H. Luther (2005), Multilayer Analytic Element Modeling of Radial Collector Wells, *Ground Water*, *43*(6), 050901015612001.
Barnes, R., and I. Janković (1999), Two-dimensional flow through large numbers of circular inhomogeneities, *Journal of Hydrology*, *226*(3), 204-210.
Basha, H. (1999), Multidimensional linearized nonsteady infiltration with prescribed boundary conditions at the soil surface, *Water resources research*, *35*(1), 75-83.
Basha, H. (2000), Multidimensional linearized nonsteady infiltration toward a shallow water table, *Water Resources Research*, *36*(9), 2567-2573.
Berkowitz, B., S. E. Silliman, and A. M. Dunn (2004), Impact of the capillary fringe on local flow, chemical migration, and microbiology, *Vadose Zone Journal*, *3*(2), 534-548.
Bischoff, H. (1981), An integral equation method to solve three dimensional confined flow to drainage systems, *Applied Mathematical Modelling*, *5*(6), 399-404.
Boano, F., C. Camporeale, and R. Revelli (2010), A linear model for the coupled surface-subsurface flow in a meandering stream, *Water Resources Research*, *46*(7).
Boussinesq, J. (1872), Théorie des ondes et des remous qui se propagent le long d'un canal rectangulaire horizontal, en communiquant au liquide contenu dans ce canal des vitesses sensiblement pareilles de la surface au fond, *Journal de Mathématiques Pures et Appliquées*, 55-108.
Buckingham, E. (1907), Studies on the movement of soil moisture.
Butler Jr, J. J. (1997), *The design, performance, and analysis of slug tests*, CRC Press.

Byrd, R. H., and R. A. Waltz (2011), An active-set algorithm for nonlinear programming using parametric linear programming, *Optimization Methods & Software*, *26*(1), 47-66.
Cardenas, M. B., and X.-W. Jiang (2010), Groundwater flow, transport, and residence times through topography-driven basins with exponentially decreasing permeability and porosity, *Water Resources Research*, *46*(11).
Carter, V. (1990), great dismal swamp: an illustrated case study, *Ecosystems of the world.*
Charbeneau, R. J. (2006), *Groundwater hydraulics and pollutant transport*, Waveland Press.
Chen, C., J. Wan, and H. Zhan (2003), Theoretical and experimental studies of coupled seepage-pipe flow to a horizontal well, *Journal of hydrology*, *281*(1), 159-171.
Correll, D. L., T. E. Jordan, and D. E. Weller (1992), Nutrient flux in a landscape: effects of coastal land use and terrestrial community mosaic on nutrient transport to coastal waters, *Estuaries*, *15*(4), 431-442.
Craig, J., and W. Read, Wayne, (2010), The future of analytical solution methods for groundwater flow and transport simulation.
Craig, J. R. (2008), Analytical solutions for 2D topography-driven flow in stratified and syncline aquifers, *Advances in Water Resources*, *31*(8), 1066-1073.
Dripps, W., R. Hunt, and M. Anderson (2006), Estimating recharge rates with analytic element models and parameter estimation, *Ground Water*, *44*(1), 47-55.
Dunne, T., and R. D. Black (1970), An experimental investigation of runoff production in permeable soils, *Water Resources Research*, *6*(2), 478-490.
Forsyth, P. A. (1988), Comparison of the single-phase and two-phase numerical model formulation for saturated-unsaturated groundwater flow, *Computer Methods in Applied Mechanics and Engineering*, *69*(2), 243-259.
Freeze, R. A., and P. Witherspoon (1967), Theoretical analysis of regional groundwater flow: 2. Effect of water-table configuration and subsurface permeability variation, *Water Resources Research*, *3*(2), 623-634.
Gardner, W. (1958), Some steady-state solutions of the unsaturated moisture flow equation with application to evaporation from a water table, *Soil science*, *85*(4), 228-232.
Genereux, D., and I. Bandopadhyay (2001), Numerical investigation of lake bed seepage patterns: effects of porous medium and lake properties, *Journal of Hydrology*, *241*(3), 286-303.
Haitjema, H. (1982), Modeling three-dimensional flow in confined aquifers using distributed singularities, University of Minnesota.
Haitjema, H. (1995), *Analytic element modeling of groundwater flow*, Academic Press.
Haitjema, H., S. Kuzin, V. Kelson, and D. Abrams (2010), Modeling Flow into Horizontal Wells in a Dupuit-Forchheimer Model, *Ground Water*, *48*(6), 878-883.
Haitjema, H. M., and S. Mitchell-Bruker (2005), Are Water Tables a Subdued Replica of the Topography?, *Ground Water*, 43 (6), 050824075421008.
Halford, K. J., and G. C. Mayer (2000), Problems Associated with Estimating Ground Water Discharge and Recharge from Stream-Discharge Records, *Groundwater*, *38*(3), 331-342.
Hantush, M. M. (2005), Modeling stream–aquifer interactions with linear response functions, *Journal of Hydrology*, *311*(1-4), 59-79.
Harte, P. T., and T. C. Winter (1993), Factors affecting recharge to crystalline rock in the Mirror Lake area, Grafton County, New Hampshire, paper presented at USGS Toxic Substances Hydrology Program—Proceedings of the Technical Meeting, Colorado Springs, Colorado, September 20–24.
Harvey, F. E., D. L. Rudolph, and S. K. Frape (1997), Measurement of hydraulic properties in deep lake sediments using a tethered pore pressure probe: Applications in the Hamilton Harbour, western Lake Ontario, *Water Resources Research*, *33*(8), 1917-1928.

Hiscock, K. M., and T. Grischek (2002), Attenuation of groundwater pollution by bank filtration, *Journal of Hydrology*, *266*(3), 139-144.
Hoffman, A. H. (1998), Pump-and-treat rescue, *Civil Engineering—ASCE*, *68*(3), 56-57.
Hunt, B. (2003), Unsteady stream depletion when pumping from semiconfined aquifer, *Journal of Hydrologic Engineering*, *8*(1), 12-19.
Hunt, B. (2009), Stream depletion in a two-layer leaky aquifer system, *Journal of Hydrologic Engineering*, *14*(9), 895-903.
Hunt, B., J. Weir, and B. Clausen (2001), A stream depletion field experiment, *Groundwater*, *39*(2), 283-289.
Hunt, R. J. (2006), Ground Water Modeling Applications Using the Analytic Element Method, *Ground Water*, *44*(1 Ground Water), 5-15.
Hunt, R. J., D. A. Saad, and D. M. Chapel (2003a), *Numerical simulation of ground-water flow in La Crosse County, Wisconsin, and into nearby pools of the Mississippi River*, US Department of the Interior, US Geological Survey.
Hunt, R. J., H. M. Haitjema, J. T. Krohelski, and D. T. Feinstein (2003b), Simulating Ground Water-Lake Interactions: Approaches and Insights, *Ground Water*, *41*(2), 227-237.
Janković, I., A. Fiori, and G. Dagan (2003), Flow and transport in highly heterogeneous formations: 3. Numerical simulations and comparison with theoretical results, *Water Resources Research*, *39*(9).
Joshi, S. D. (2003), Cost/benefits of horizontal wells, paper presented at SPE Western Regional/AAPG Pacific Section Joint Meeting, Society of Petroleum Engineers.
Kacimov, A. (2000), Three-dimensional groundwater flow to a lake: an explicit analytical solution, *Journal of Hydrology*, *240*(1), 80-89.
Kacimov, A. (2007), Three-dimensional groundwater flow to a shallow pond: An explicit solution, *Journal of Hydrology*, *337*(1), 200-206.
Kelson, V. (2012), Predicting Collector Well Yields with MODFLOW, *Ground Water*, *50*(6), 918-926.
Kirkham, D. (1967), Explanation of paradoxes in Dupuit Forchheimer Seepage Theory, *Water Resources Research*, *3*(2), 609-622.
Knupp, P. (1996), A moving mesh algorithm for 3-D regional groundwater flow with water table and seepage face, *Advances in Water Resources*, *19*(2), 83-95.
Larabi, A., and F. De Smedt (1997), Numerical solution of 3-D groundwater flow involving free boundaries by a fixed finite element method, *Journal of Hydrology*, *201*(1), 161-182.
Luther, K., and H. M. Haitjema (1999), An analytic element solution to unconfined flow near partially penetrating wells, *Journal of Hydrology*, *226*(3), 197-203.
Luther, K., and H. Haitjema (2000), Approximate analytic solutions to 3D unconfined groundwater flow within regional 2D models, *Journal of Hydrology*, *229*(3), 101-117.
Luther, K. H. (1998), Analytic solutions to three-dimensional unconfined groundwater flow near wells, Indiana University.
Marklund, L., and A. Wörman (2011), The use of spectral analysis-based exact solutions to characterize topography-controlled groundwater flow, *Hydrogeology Journal*, *19*(8), 1531-1543.
Matott, L. S., A. J. Rabideau, and J. R. Craig (2006), Pump-and-treat optimization using analytic element method flow models, *Advances in Water Resources*, *29*(5), 760-775.
McCallum, A. M., M. S. Andersen, G. C. Rau, and R. I. Acworth (2012), A 1-D analytical method for estimating surface water-groundwater interactions and effective thermal diffusivity using temperature time series, *Water Resources Research*, *48*(11).
Mehl, S., and M. C. Hill (2010), Grid-size dependence of Cauchy boundary conditions used to simulate stream–aquifer interactions, *Advances in Water Resources*, *33*(4), 430-442.

Miller, H., J. M. Bull, C. J. Cotterill, J. K. Dix, I. J. Winfield, A. E. Kemp, and R. B. Pearce (2013), Lake bed geomorphology and sedimentary processes in glacial lake Windermere, UK, *Journal of Maps*, *9*(2), 299-312.
Mishra, P. K., and S. P. Neuman (2010), Improved forward and inverse analyses of saturated-unsaturated flow toward a well in a compressible unconfined aquifer, *Water Resources Research*, *46*(7).
Mishra, P. K., V. Vessilinov, and H. Gupta (2013), On simulation and analysis of variable-rate pumping tests, *Ground Water*, *51*(3), 469-473.
Moore, R., V. Kelson, J. Wittman, and V. Rash (2012), A Modeling Framework for the Design of Collector Wells, *Ground Water*, *50*(3), 355-366.
Nahin, P. J. (2011), *Dr. Euler's fabulous formula: cures many mathematical ills*, Princeton University Press.
Nield, S. P., L. R. Townley, and A. D. Barr (1994), A framework for quantitative analysis of surface water-groundwater interaction: Flow geometry in a vertical section, *Water Resources Research*, *30*(8), 2461-2475.
Okkonen, J., and B. Kløve (2011), A sequential modelling approach to assess groundwater–surface water resources in a snow dominated region of Finland, *Journal of Hydrology*, *411*(1), 91-107.
Ophori, D. U., and R. N. Farvolden (1985), A hydraulic trap for preventing collector well contamination: a case study, *Groundwater*, *23*(5), 600-610.
Oz, I., E. Shalev, H. Gvirtzman, Y. Yechieli, and I. Gavrieli (2011), Groundwater flow patterns adjacent to a long-term stratified (meromictic) lake, *Water Resources Research*, *47*(8), n/a-n/a.
Patel, H., C. Shah, and D. Shah (1998), Modeling of radial collector well for sustained yield: a case study, paper presented at Proc int conf MODFLOW.
Patel, H., T. Eldho, and A. Rastogi (2010), Simulation of radial collector well in shallow alluvial riverbed aquifer using analytic element method, *Journal of irrigation and drainage engineering*, *136*(2), 107-119.
Philip, J. (1998), Seepage shedding by parabolic capillary barriers and cavities, *Water resources research*, *34*(11), 2827-2835.
Powers, W., D. Kirkham, and G. Snowden (1967), Orthonormal function tables and the seepage of steady rain through soil bedding, *Journal of Geophysical Research*, *72*(24), 6225-6237.
Ray, C., T. Grischek, J. Schubert, J. Z. Wang, and T. F. Speth (2002), A Perspective of Riverbank Filtration (PDF), *Journal-American Water Works Association*, *94*(4), 149-160.
Read, W., and R. Volker (1993), Series solutions for steady seepage through hillsides with arbitrary flow boundaries, *Water Resources Research*, *29*(8), 2871-2880.
Read, W., and P. Broadbridge (1996), Series solutions for steady unsaturated flow in irregular porous domains, *Transport in porous media*, *22*(2), 195-214.
Read, W., S. Belward, P. Higgins, and G. Sneddon (2005), Series solutions for seepage in three dimensional aquifers, *ANZIAM Journal*, *46*, C1126--C1140.
Richards, L. A. (1931), Capillary conduction of liquids through porous mediums, *Journal of Applied Physics*, *1*(5), 318-333.
Romanoa, C. G., E. O. Frind, and D. L. Rudolph (1999), Significance of Unsaturated Flow and Seepage Faces in the Simulation of Steady-State Subsurface Flow, *Groundwater*, *37*(4), 625-632.
Rushton, K. (2007), Representation in regional models of saturated river–aquifer interaction for gaining/losing rivers, *Journal of Hydrology*, *334*(1-2), 262-281.
Rushton, K. R., and F. C. Brassington (2013a), Hydraulic behaviour and regional impact of a horizontal well in a shallow aquifer: example from the Sefton Coast, northwest England (UK), *Hydrogeology Journal*, *21*(5), 1117-1128.

Rushton, K. R., and F. C. Brassington (2013b), Significance of hydraulic head gradients within horizontal wells in unconfined aquifers of limited saturated thickness, *Journal of Hydrology*, *492*, 281-289.
Samani, N., M. Kompani-Zare, H. Seyyedian, and D. Barry (2006), Flow to horizontal drains in isotropic unconfined aquifers, *Journal of Hydrology*, *324*(1), 178-194.
Selim, H. (1975), Water flow through a multilayer stratified hillside, *Water Resources Research*, *11*(6), 949-957.
Serrano, S. E., and S. Workman (1998), Modeling transient stream/aquifer interaction with the non-linear Boussinesq equation and its analytical solution, *Journal of Hydrology*, *206*(3), 245-255.
Simpkins, W. W. (2006), A multiscale investigation of ground water flow at Clear Lake, Iowa, *Ground Water*, *44*(1), 35-46.
Smerdon, B., K. Devito, and C. Mendoza (2005), Interaction of groundwater and shallow lakes on outwash sediments in the sub-humid Boreal Plains of Canada, *Journal of Hydrology*, *314*(1), 246-262.
Smerdon, B., C. Mendoza, and K. Devito (2007), Simulations of fully coupled lake-groundwater exchange in a subhumid climate with an integrated hydrologic model, *Water Resources Research*, *43*(1).
Sophocleous, M. (2002), Interactions between groundwater and surface water: the state of the science, *Hydrogeology Journal*, *10*(1), 52-67.
Sophocleous, M., M. Townsend, L. Vogler, T. McClain, E. Marks, and G. Coble (1988), Experimental studies in stream-aquifer interaction along the Arkansas River in central Kansas—Field testing and analysis, *Journal of Hydrology*, *98*(3), 249-273.
Stark, J., D. Armstrong, and D. Zwilling (1994), *Stream-aquifer interactions in the Straight River area, Becker and Hubbard Counties, Minnesota*, US Geological Survey.
Steward, D. R. (1999), Three-dimensional analysis of the capture of contaminated leachate by fully penetrating, partially penetrating, and horizontal wells, *Water Resources Research*, *35*(2), 461-468.
Steward, D. R., and W. Jin (2001), Gaining and losing sections of horizontal wells, *Water Resources Research*, *37*(11), 2677-2685.
Steward, D. R., and W. Jin (2003), Drawdown and capture zone topology for nonvertical wells, *Water Resources Research*, *39*(8).
Strack, O. D. (1984), Three Dimensional Streamlines in Dupuit-Forchheimer Models, *Water Resources Research*, *20*(7), 812-822.
Strack, O. D. (Ed.) (1989), *Groundwater mechanics*, Prentice-Hall, Englewood Cliffs, NJ.
Strack, O. D., and H. M. Haitjema (1981), Modeling double aquifer flow using a comprehensive potential and distributed singularities: 1. Solution for homogeneous permeability, *Water Resources Research*, *17*(5), 1535-1549.
Tartakovsky, G. D., and S. P. Neuman (2007), Three-dimensional saturated-unsaturated flow with axial symmetry to a partially penetrating well in a compressible unconfined aquifer, *Water Resources Research*, *43*(1).
Teloglou, I. S., and R. K. Bansal (2012), Transient solution for stream–unconfined aquifer interaction due to time varying stream head and in the presence of leakage, *Journal of Hydrology*, *428-429*, 68-79.
Therrien, R., R. McLaren, E. Sudicky, and S. Panday (2008), HydroGeoSphere: A three-dimensional numerical model describing fully-integrated subsurface and surface flow and solute transport, *Groundwater Simul. Group, Waterloo, Ont., Canada*.
Townley, L. R., and M. G. Trefry (2000), Surface water-groundwater interaction near shallow circular lakes: Flow geometry in three dimensions, *Water Resources Research*, *36*(4), 935-948.

Tristscher, P., W. Read, P. Broadbridge, and J. Knight (2001), Steady saturated-unsaturated flow in irregular porous domains, *Mathematical and computer modelling*, *34*(1), 177-194.
Tsou, P. R., Z. Y. Feng, H. D. Yeh, and C. S. Huang (2010), Stream depletion rate with horizontal or slanted wells in confined aquifers near a stream, *Hydrology and Earth System Sciences*, *14*(8), 1477-1485.
Wang, X. S., S. P. Neuman, O. D. Strack, A. Verruijt, M. Jamali, B. Seymour, J. Bear, A. H. D. Cheng, C. Chen, and X. Kuang (2011), Methods to derive the differential equation of the free surface boundary, *Groundwater*, *49*(2), 133-143.
Ward, N. D., and H. Lough (2011), Stream depletion from pumping a semiconfined aquifer in a two-layer leaky aquifer system, *Journal of Hydrologic Engineering*, *16*(11), 955-959.
Werner, A. D., M. R. Gallagher, and S. W. Weeks (2006), Regional-scale, fully coupled modelling of stream–aquifer interaction in a tropical catchment, *Journal of Hydrology*, *328*(3-4), 497-510.
Winter, T., and H. Pfannkuch (1984), Effect of anisotropy and groundwater system geometry on seepage through lakebeds: 2. Numerical simulation analysis, *Journal of Hydrology*, *75*(1), 239-253.
Winter, T. C., and D. O. Rosenberry (1995), The interaction of ground water with prairie pothole wetlands in the Cottonwood Lake area, east-central North Dakota, 1979–1990, *Wetlands*, *15*(3), 193-211.
Wong, S., and J. R. Craig (2010), Series solutions for flow in stratified aquifers with natural geometry, *Advances in Water Resources*, *33*(1), 48-54.
Workman, S., S. Serrano, and K. Liberty (1997), Development and application of an analytical model of stream/aquifer interaction, *Journal of Hydrology*, *200*(1), 149-163.
Wörman, A., A. I. Packman, L. Marklund, J. W. Harvey, and S. H. Stone (2006), Exact three-dimensional spectral solution to surface-groundwater interactions with arbitrary surface topography, *Geophysical Research Letters*, *33*(7).
Yeh, H.-D., and Y.-C. Chang (2013), Recent advances in modeling of well hydraulics, *Advances in Water Resources*, *51*, 27-51.
Zhan, H., and V. A. Zlotnik (2002), Groundwater flow to a horizontal or slanted well in an unconfined aquifer, *Water Resources Research*, *38*(7), 13-11-13-11.
Zhan, H., L. V. Wang, and E. Park (2001), On the horizontal-well pumping tests in anisotropic confined aquifers, *Journal of Hydrology*, *252*(1), 37-50.